

Engineering Micro-Vortex Streaming via Acoustofluidics

by

Shuaiguo Zhao

Department of Mechanical Engineering and Materials Science
Duke University

Date: _____

Approved:

Tony Jun Huang, Supervisor

Pei Zhong

Xiaoyue Ni

Mark Walters

Dissertation submitted in partial fulfillment of
the requirements for the degree of Doctor
of Philosophy in the Department of
Mechanical Engineering and Materials Science in the Graduate School
of Duke University

2022

ABSTRACT

Engineering Micro-Vortex Streaming via Acoustofluidics

by

Shuaiguo Zhao

Department of Mechanical Engineering and Materials Science
Duke University

Date: _____

Approved:

Tony Jun Huang, Supervisor

Pei Zhong

Xiaoyue Ni

Mark Walters

An abstract of a dissertation submitted in partial
fulfillment of the requirements for the degree
of Doctor of Philosophy in the Department of
Mechanical Engineering and Materials Science in the Graduate School of
Duke University

2022

Copyright by
Shuaiguo Zhao
2022

Abstract

Acoustofluidic technologies, the integration of acoustics into microfluidics, offer rich possibilities for particle manipulation in life sciences. One promising aspect of these technologies is acoustic micro-vortex streaming, resulting from the energy dissipation of acoustics into fluids. There are two opposing directions for the development of micro-vortex streaming: the first one is increasing rotational flow to enhance microscale fluid motion for laminar fluid mixing and capture of biological particles; the other is suppressing rotational flow to create stable acoustic pressure fields for particle patterning, deflection and separation. Although these developments have demonstrated success in microfluidic mixing and cell separation, their ability to realize nanoparticle separation and precisely control fluid mixing, particularly for viscous samples, multi-fluids, and sequential fluids, remains limited. In this dissertation, we target at expanding micro-vortex streaming based acoustofluidic technologies by addressing the existed technological hurdles and introducing new physical concept of topological insulator.

To this end, we first developed a sharp edge based acoustofluidic micromixer that enables robust and strong mixing. Robust, efficient, and strong mixing in microfluidics is essential to viscous biological sample preparation. Inspired by the concept that the energy band of phononic crystals depends strongly on their structure height and substrate thickness, we maximized micro-vortex streaming via

rational design of the microchamber and glass substrate thickness. The device is able to not only mix fluids across a wide range of flow rates up to $150 \mu\text{L min}^{-1}$, but also process fluids with viscosities to $95.9 \text{ mPa}\cdot\text{s}$. Using this strong micro-vortex streaming, we were able to realize on-chip liquefaction for human stool samples. This device provides a promising platform to be integrated with portable stool diagnostics.

Next, we developed a sharp edge based acoustofluidic micromixer capable of achieving rapid, multi-fluid (≥ 2) and multi-step (≥ 2) mixing, which is difficult to realize in hydrodynamic fluid focusing method. Rapid, multi-step and multi-fluid mixing is critical to nanomaterial synthesis for drug delivery. These novel capabilities are realized simply by varying the strength and sites of micro-vortex streaming. With this platform, we synthesized homogeneous poly(lactide-co-glycolide)-block-poly(ethylene glycol) (PLGA-PEG) nanoparticles by rapid mixing, high-molecular PLGA-PEG nanoparticles by strong mixing, PLGA-lipid core-shell nanoparticles by two-step mixing and chitosan nanoparticles by three-fluid mixing. When combined with varying flow rates and reagent concentrations, the acoustofluidic platform allows for nanoparticle synthesis with unprecedented control of nanoparticle size and structure.

We have also developed a surface acoustic wave (SAW)-based, disposable acoustofluidic platform for bacteria separation by suppressing micro-vortex streaming

and enhancing acoustic pressure field. SAW induced micro-vortex streaming is generated by the viscous attenuation of SAW propagation. In SAW-based devices, the acoustic streaming competes with acoustic radiation force. To overcome SAW induced streaming, we generated standing SAW to form time-averaged momentum flux in opposite direction and then cancelling it out. To increase acoustic radiation force, we designed unidirectional transducers that enable SAW to propagate primarily in one direction, thus tremendously increasing acoustic energy intensity. Using this device, we were able to pattern 400 nm polystyrene particles within the disposable microchannel, as well as separate 600 nm silicon dioxide and 200 nm silver nanoparticles from 1 μm polystyrene particles. Additionally, our disposable device achieved high-purity separation of bacteria from human red blood cells (RBCs). This method of unidirectional transducer design provides a way of enhancing acoustic radiation force to suppress acoustic streaming.

Finally, we developed a valley hall based topological acoustofluidic device with the characteristic of chiral micro-vortex streaming by introducing the concept of topological insulator. Topological insulators, which originate from condensed matter physics, have recently been exploited for unconventional wave propagation. One of the prominent features of valley-hall based topological insulators is chiral vortex feature of energy flux. By electroplating copper micropillars on a lithium niobate substrate, we established hexagonal latticed copper pillars with valley hall effect in microfluidics, where SAW was utilized as excitation source. We numerically and experimentally demonstrated

clockwise and anticlockwise of vortex streaming by tracing 200 nm fluorescent polystyrene particles. To our knowledge, this is the first visualization of chiral vortex feature in topological insulators. Within the microfluidic community, this allows for novel functionalities including unidirectional particle rotation and back-movement immune particle transport. In the topological physics space, the liquid domain within microfluidic devices enables a new technology for characterizing topological spin textures, which is difficult to be realized in solid or air domain. Furthermore, multiphysics nature of the system enriches the physics of topological insulators. Therefore, the topological acoustofluidics developed here expands not only the field of microfluidics but also the field of topological insulators.

In summary, this dissertation serves to further the knowledge of micro-vortex streaming along three planes: enhancing micro-vortex streaming, suppressing micro-vortex streaming, and introducing topological physics to generate chiral micro-vortex streaming. Finally, I will provide my perspective for the next-generation development of micro-vortex streaming based technologies and possible emerging applications. I hope that eventually the microfluidic and physical communities can benefit from each other.

Dedication

This dissertation is dedicated to my mother, Ping, who has encouraged me all the time during my Ph.D. studies.

Contents

Abstract	iv
List of Tables	xiii
List of Figures	xiv
Acknowledgements	xvii
1. Introduction	1
1.1 Microfluidics	1
1.1 Acoustofluidics	3
1.2 Different Mechanisms for Micro-Vortex Streaming	7
1.3.1. Sharp Edge Oscillation Induced Vibration Streaming	8
1.3.2. SAW Energy Dissipation Induced Streaming	10
1.3.3. Topological Symmetry Broken Induced Chiral Vortex Feature	11
1.4. Applications of Micro-Vortex Streaming	13
1.4.1. Fluid Manipulation Using Vibration Streaming	14
1.4.2. Particle Manipulation Using Micro-Vortex Streaming	16
1.4.3. Particle Manipulation by Suppressing Micro-Vortex Streaming	18
1.5. Dissertation Outline	19
2. On-Chip Stool Liquefaction via Acoustofluidics	21
2.1. Motivation	21
2.2. Materials and Methods	24
2.2.1. Stool Sample	24

2.2.2.	Fabrication and Operation of Acoustofluidic Devices.....	24
2.2.3.	Standard Stool Liquefaction Procedure	28
2.2.4.	Morphology Characterization	28
2.2.5.	Bacterial Cell Culture.....	29
2.2.6.	Bacterial Viability via Fluorescence Microscope and Flow Cytometry	29
2.3.	Results and Discussion	30
2.3.1.	Rational Acoustofluidic Design to Improve Mixing Performance.....	30
2.3.2.	Visual Comparison.....	36
2.3.3.	Morphology Characterization	37
2.3.4.	Bacterial Cell Culture.....	38
2.3.5.	Fluorescence Microscope	40
2.3.6.	Flow Cytometry.....	41
2.4.	Conclusions	43
3.	Size- and Structure-Controlled Synthesis of Polymeric Nanoparticles via Acoustofluidics.....	44
3.1.	Motivation	44
3.2.	Materials and Methods	47
3.2.1.	Chemicals	47
3.2.2.	Device Fabrication.....	48
3.2.3.	Nanoparticle Synthesis from Low-Molecular-Weight Polymers	49
3.2.4.	Nanoparticle Synthesis from High-Molecular-Weight Polymers	49
3.2.5.	PLGA-PEG/Lipid Core-Shell Nanoparticle Synthesis	50

3.2.6.	Synthesis of Chitosan Nanoparticles	51
3.2.7.	Sample Characterization	52
3.3.	Results and Discussion	52
3.3.1.	Principle of the Acoustofluidic Synthesis Platform.....	52
3.3.2.	Controllable Synthesis of Low-Molecular-Weight Nanoparticles	56
3.3.3.	Controllable Synthesis of High-Molecular-Weight Nanoparticles	63
3.3.4.	Multiple Reagent Mixing for Chitosan Nanoparticle Synthesis.....	70
3.3.5.	Sequential Nanoprecipitation for Core-Shell Nanoparticle Synthesis	73
3.4.	Conclusions	76
4.	A Disposable Acoustofluidic Chip for Nano/Micro Particle Separation using Unidirectional Acoustic Transducers.....	78
4.1.	Motivation	79
4.2.	Materials and Methods	82
4.2.1.	Device Fabrication.....	82
4.2.2.	Experimental Setup.....	85
4.2.3.	Sample Characterization	87
4.3.	Results and Discussion	87
4.3.1.	Characterization of Disposable Acoustofluidic Chips with Hybrid Hard/Soft Material Design.....	87
4.3.2.	Disposable Acoustofluidic Chips for Particle Deflection	95
4.3.3.	Disposable Acoustofluidic Chips for Nano/Micro Particle Separation	98
4.3.4.	Disposable Acoustofluidic Chips for Bacteria Separation.....	102
4.4.	Conclusions	104

5. Topological Acoustofluidics	106
5.1. Motivation	106
5.2. Methods	110
5.2.1. Sample Fabrication.....	110
5.2.2. Experimental Measurement.....	110
5.2.3. Numerical Simulation.....	111
5.3. Results and Discussion	112
5.3.1. Design of On-Chip Topological Acoustofluidic Device	112
5.3.2. Experimental Visualization of Chiral Vortex Streaming at Valley Projected Edge State	114
5.3.3. Topological Pressure Wells at Edge-State Pathways for Reversible Particle Manipulation.....	117
5.3.4. Topological Acoustofluidic Mapping of the Anisotropic Edge States on Lithium Niobate	120
5.4. Conclusions	122
6. Conclusion.....	123
6.1. Summary.....	123
6.2. Potential Future Work.....	126
References	128
Biography.....	147

List of Tables

Table 1: The number of live/dead bacteria in the stool sample on different days..... 41

Table 2: Acoustic performance comparison between “hard PDMS” and “soft PDMS” ... 84

List of Figures

Figure 1.1: Micro-vortex streaming in sharp edge based acoustofluidic device.....	8
Figure 1.2: Micro-vortex streaming in surface acoustic wave devices	10
Figure 1.3: Chiral vortex of energy flux in topological phononic insulator.....	12
Figure 1.4: Fluid mixing in sharp edge based acoustofluidic devices.....	15
Figure 1.5: SAW induced micro-vortex streaming for selectively particle capture.....	16
Figure 1.6: The suppression of micro-vortex streaming for particle manipulation.....	17
Figure 2.1: Device operation principle of micro-vortex streaming.....	25
Figure 2.2: Detailed design of the acoustofluidic-based stool liquefaction device.....	26
Figure 2.3: Dependence of mixing performance on driving frequency.	32
Figure 2.4: Rational design of device parameters by the characterization of mixing performance of the acoustofluidic devices.....	33
Figure 2.5: Numerical simulation and experimental results for mixing investigation of viscous PEGDA700 polymer solution.....	34
Figure 2.6: Photo of visual observation of human stool samples.....	36
Figure 2.7: SEM characterization of liquefied human stool samples.....	37
Figure 2.8: Photos of bacterial cell culture.....	39
Figure 2.9: Different fluorescence microscope images (100 x) of Live/Dead BacLight stained liquefied stool samples	40
Figure 2.10: Flow cytometry for liquefied stool samples.	42
Figure 3.1: Design and working principle of the acoustofluidic synthesis platform for core-shell nanoparticle synthesis.....	53
Figure 3.2: The mixing process of DI water and fluorescence dye under 50 V _{PP} characterized using a fast camera (Photron, 500K-M1) at different total flow rates.....	56

Figure 3.3: Effect of the mixing performance of the acoustofluidic device on the size of PLGA-PEG NPs.....	58
Figure 3.4: Comparison of PLGA-PEG NPs synthesized by vortex mixing and acoustofluidic mixing.....	60
Figure 3.5: Comparison of average size of PLGA-PEG NPs synthesized with various parameters.....	62
Figure 3.6: Acoustofluidic synthesis of high molecular weight polymeric nanoparticles without aggregation.....	65
Figure 3.7: Size-tunable synthesis of PLGA-PEG nanoparticles from high-molecular-weight polymers.....	68
Figure 3.8: Synthesis of chitosan nanoparticles based on the nanocomplexation (NCP) mechanism using the acoustofluidic device.....	71
Figure 3.9: Sequential nanoprecipitation for core-shell PLGA70K-PEG2K/lipid nanoparticles synthesis.....	73
Figure 4.1: Principle of the disposable separation device.....	82
Figure 4.2: Schematic of the experimental setup for acoustic performance measurement.....	84
Figure 4.3: The unidirectional interdigital transducer (IDT) design with floating electrodes.....	89
Figure 4.4: Comparison of unidirectional IDT and bidirectional IDT.....	90
Figure 4.5: The performance of disposable acoustofluidic chips in the absence of fluid flow.....	91
Figure 4.6: Disposable acoustofluidic chips for particle defection in a continuous flow.....	95
Figure 4.7: The taSSAW field in disposable acoustofluidic chips for the separation of 1 μm fluorescent particles and 6 μm non-fluorescent PS particles.....	98
Figure 4.8: Disposable acoustofluidic chips for nano/micro particle separation in a continuous flow.....	100

Figure 4.9: Disposable acoustofluidic chips for bacteria separation.....	102
Figure 5.1: Design of a topological acoustofluidic chip with valley state modes.	113
Figure 5.2: Experimental characterization of chiral vortex streaming feature of edge state in fluids.....	115
Figure 5.3: Experimental demonstration of robust edge states for reversible particle manipulation in an acoustofluidic chip.	117
Figure 5.4: Topological acoustofluidic mapping of the anisotropic edge states on an anisotropic lithium niobate chip	120

Acknowledgements

First, I would like to thank my advisor, Dr. Tony Huang, for his tremendous help and support all the time. I appreciate the chance to pursue my research dream in microfluidics, which is different from my previous background on polymer processing. He guides me step by step from microfluidics, microfabrication to critical thinking, acoustic physics, and numerical simulations. He trains me to study deeply in math, understand well in physics, and explore life sciences for real-world applications. He cares not only my research but also my communication skill, presentation skill, and activities participation at Duke. His work style would be a valuable lesson for my life. I also very thankful for tremendous discussions with Prof. Luke Lee at Harvard University and Prof. Steven Cummer at Duke. Moreover, I would like to express my appreciation for my committee members, Dr. Pei Zhong, Dr. Xiaoyue Ni, and Dr. Mark Walters for their valuable time and perspectives.

Second, I thank all the lab members from my lab. Specially, I acknowledge Dr. Po-Hsun Huang, Dr. Zhenhua Tian, Dr. Chen Shen, Dr. Mengxi Wu, Dr. Hunter Bachman, and Jianping Xia for their helpful discussion. I also thank the help from Shujie Yang, Peiran Zhang, Jianping Xia, Yuyang Gu, Chuyi Chen, Zeyu Wang, Genosson Jin, Zhemiao Xie, Heying Zhang, Zhehan Ma, and Defei Liao.

Finally, my sincere thanks to my family and my friends for their long-term support and the staffs in my departments and duke clean room.

1. Introduction

1.1 Microfluidics

Microfluidics represent the field to process small amounts of fluids within a microscale channel, allowing the convergence of fluid mechanics with chemistry, physics, biology and material science.¹ The intrinsic microscale dimension of microfluidic devices endows it with possibilities for fluid manipulation beyond what is possible in conventional macroscale levels. This is due, in part, to the fact that fluid flow shifts from a turbulent regime dominated by inertial forces at the macroscale to a laminar regime dominated by inertial forces at the microscale. The ratio of inertial forces to viscous forces, which depends strongly on spatial dimension, is represented by Reynolds number (Re)²:

$$Re = \frac{\rho v L}{\mu} \quad (1.1)$$

where ρ , v , L , and μ refer to fluid density, fluid velocity, hydraulic diameter of microchannel, and fluid dynamic viscosity, respectively. When Re is less than 2000, the fluid flow begins to convert from chaotic, turbulent to smooth, laminar flow. In microfluidic channels, Re is approximately equivalent to 1, indicating a fully laminar flow system.³ For laminar flow, the fluid velocity between two side walls of microchannels is predicted as a parabolic distribution. Meanwhile, the diminutive scale of microchannels tremendously enlarges the surface area to volume ratio. This predictable flow profile and large surface area to volume ratio allows for precise fluid control, as well as rapid heat and mass transfer within microfluidic environments. When applied to sample process,

microfluidic devices allow for (i) rapid sample processing; (ii) a homogenous reaction environment; (iii) reduced reagent volumes; (iv) convenient modules for point of care diagnostics and (v) high sensitivity.^{1, 4} With these merits, microfluidic devices have spawned significant progress in many fields.

One notable area in which microfluidic devices have the potential to further development is the integration of microfluidic micromixing with nanoparticle technique for nanomedicine development.⁵ Nanomedicine systems typically require nanoparticles to be monodisperse, size-tunable and structure-controllable. Unfortunately, standard vortexing methods lack control over the mixing process, leading to poor reproducibility and polydispersity. These issues can be addressed with the emergence of different microfluidic methodologies such as hydrodynamic flow focusing (HFF) and tesla microstructures.^{5, 6} Furthermore, the mixing time in microfluidic devices can be estimated by the following equation:^{1, 5}

$$\tau_{mix} \sim \frac{w^2}{D} \quad (1.2)$$

Where, w and D represent diffusion length and diffusion coefficient, respectively. Typically, the microfluidic mixing time is calculated to be in the order of milliseconds. This ability to rapidly mix reagents makes microfluidic methods attractive for nanoparticle synthesis. In 2008, a microfluidic 2D HFF method was proposed to synthesize PLGA-PEG nanoparticles.⁵ Using rapid mixing, microfluidic methods generated nanoparticles with smaller size and better reproducibility than conventional

batch methods. Later in 2011, a 3D HFF microfluidic method demonstrated their ability to precisely tune nanoparticle size from 30 to 230 nm by varying polymer molecular weights and concentrations.⁷ This broad size range is sufficient for a multitude of drug delivery scenarios. Furthermore, novel lipid-PLGA core-shell nanoparticles have been fabricated using microfluidic device with Tesla microstructures; these nanoparticles combine the desired properties of polymeric nanoparticles and liposomes such as high drug loading and high serum stability.⁶ Due to their excellent controllability, microfluidic devices have been becoming an important platform for real-world nanomedicine and vaccine development. Similarly, a library of microfluidic devices has been designed for other promising applications such as cell separation and biomarker detection.⁸⁻¹⁰

1.1 Acoustofluidics

Despite the significant progress, passive microfluidic paradigms continue to suffer from a variety of issues including incomplete reactions in hydrodynamic mixing devices, limited tunability in hydrodynamic separation devices, as well as channel clogging in microstructure enabled separation devices.^{5, 11} The expanding fields of microfluidics, where external forces are applied to manipulate fluids, provide possibilities to overcome these constraints. To date, a variety of external force fields have been modulated into microfluidic devices for acoustic, magnetic and dielectrophoretic particle manipulation.¹² Compared with other methods, acoustic method is contact-free and label-free; this property has led to considerable interest in combining acoustics and microfluidic

techniques into “acoustofluidic” devices.¹²⁻¹⁴ Within acoustofluidic devices are three categories of forces for particle manipulation: traveling wave force, acoustic streaming, and standing acoustic radiation force.¹¹ Here, we will first focus on the acoustic radiation force before turning our discussion to acoustic streaming in next section.

Acoustic radiation forces for microfluidic particle manipulation stem from the scattering of acoustic waves in the vicinity of particles suspended in an acoustic field.¹⁵ Scattering along the direction of traveling wave propagation results in traveling wave forces. In standing acoustic wave fields, acoustic radiation forces arise from time-averaged force potential gradients in fluids.¹⁵ Due to this difference in force generation, travelling wave forces and standing acoustic radiation forces exhibit a large differential effects on particle manipulation. With travelling wave forces, particles are moved continuously over several wavelengths in the direction of wave propagation. However, the capability of travelling wave forces to manipulate particles is limited by a particle size/wavelength ratio ($\kappa = 2\pi R/\lambda$), above which effective particle translation can be achieved.¹¹ This ratio requires the fluid wavelength to be on the order of particle size and therefore it is difficult for travelling wave force to manipulate submicron particles. In contrast, in standing wave fields, particles are translated to pressure nodal or antinodal positions based on the acoustic contrast factor between particles and fluids.¹⁴ The standing acoustic radiation forces scale with particle volume, and therefore are able to manipulate particles with dimensions much smaller than acoustic wavelengths. The periodic pressure field between

adjacent standing nodes/antinodes is also more predictable than the attenuated travelling pressure field. Therefore, travelling wave forces are less utilized than standing radiation forces for particle manipulation.

The acoustic radiation force in fluids is mathematically expressed as the following equation:¹⁵

$$F^{rad} = -\pi a^3 \left[\frac{2\kappa_0}{3} \text{Re}[f_1 p_{in}^* \nabla p_{in}] - \rho_0 \text{Re}[f_2 v_{in}^* \nabla v_{in}] \right] \quad (1.3)$$

Where p_{in} , v_{in} and κ_0 represent incoming pressure amplitude, incoming velocity amplitude and compressibility of the fluid, respectively. In the standing acoustic fields used for particle manipulation, the size of the particles is usually much smaller than acoustic wavelength, and the radiation force becomes a gradient force and can be simplified:¹⁵

$$F^{rad} = -\nabla U^{rad} \quad (1.4)$$

Here U is the Gor'kov force potential and is given as:^{3, 15}

$$U^{rad} = \frac{4a^3}{3} \left(\frac{f_1}{2c_0^2 \rho_0} \overline{p_{in}^2} - \frac{3f_2}{4} \rho_0 \overline{v_{in}^2} \right) \quad (1.5)$$

$$f_1 = 1 - \frac{c_0^2 \rho_0}{c_p^2 \rho_p}, \quad f_2 = \frac{2(\rho_p - \rho_0)}{2\rho_p + \rho_0} - p_2 \quad (1.6)$$

where c_0 , ρ_0 , c_p and ρ_p are the speed of sound, the density of the fluid, speed of sound in particle, and the density of the particles. In a rectangular microfluidic chamber with planar side walls at $x=0$ and $x=h$, the incoming wave pressure becomes

$p = p_0 \cdot \sin(kx) \cdot \cos(\omega t)$. The acoustic radiation force further simplifies into the classical format presented by Yosioka and Kawasima.¹⁶

$$F_r = - \left(\frac{\pi p_0^2 V \beta_0}{2\lambda} \right) \cdot \varphi(\beta, \rho) \cdot \sin(2kx) \quad (1.7)$$

$$\varphi(\beta, \rho) = \frac{5\rho_p - 2\rho_0}{2\rho_p + \rho_0} - \frac{\beta_p}{\beta_0} \quad (1.8)$$

where, p_0 , λ , V , k , and x are the pressure amplitude, wavelength, particle volume, the wavenumber and the distance between particle and pressure node/antinode. The trajectories of particle movement can be numerically calculated based on forces balance using Newton's second law. In standing acoustic fields, particles are subjected to gravity, Stokes' drag, acoustic radiation and buoyancy, where the buoyancy force and gravitational force balance each other.³ The Stokes drag force is given by:³

$$F_{drag} = - 6\pi\eta r(\nu_p - \nu_0) \quad (1.9)$$

Where η , r , ν_p and ν_0 are the viscosity of the fluid, particle radius, particle velocity and fluid velocity, respectively. The fluid velocity within microchannels can be solved using balance laws in fluid mechanics. In a viscous compressible fluid, the governing equations of mass and momentum conservation are given by:¹⁷

$$\frac{\partial \rho}{\partial t} + \nabla \cdot (\rho \nu_0) = 0 \quad (1.10)$$

$$\rho \frac{\partial \nu}{\partial t} + \rho(\nu_0 \cdot \nabla) \nu_0 = - \nabla p + \mu \nabla^2 \nu_0 + \left(\mu_b + \frac{1}{3} \mu \right) \nabla (\nabla \cdot \nu) \quad (1.11)$$

Combining these theories of fluid mechanics, pressure acoustics, and solid mechanics provides the basis for numerical simulation that guide experimental work. In the next two sections, we will discuss in detail the formation and applications of acoustic micro-vortex streaming.

1.2 *Different Mechanisms for Micro-Vortex Streaming*

Acoustic micro-vortex streaming is defined as a rotational fluid flow stemming from the dissipation of acoustic energy into fluids.¹⁸ From a force analysis perspective, acoustic streaming is ascribed to time-averaged momentum flux.¹⁸ Based on the formation principle, acoustic streaming can be classified into bubble oscillation induced cavitation streaming, sharp edge oscillation induced vibration streaming, surface acoustic wave induced streaming, boundary layer induced streaming, and topological symmetry broken induced streaming.^{11, 17-19} These streaming types are generated from two types of acoustic waves: flexural acoustic waves and surface acoustic waves. The former refers to acoustic wave propagation through the bulk substrate, while the latter refers to wave transportation on the surface of the substrate. Here, we will discuss the three most important three categories of streaming: sharp edge oscillation induced vibration streaming, surface acoustic wave induced streaming and topological symmetry broken induced chiral vortices.

1.3.1. Sharp Edge Oscillation Induced Vibration Streaming

Acoustofluidic devices with sharp edge microstructures are often applied to generate vibrational streaming via the dissipation of acoustic energy in the vicinity of stably oscillating sharp edge tips.²⁰ These devices are comprised of a piezoelectric transducer, a glass coverslip and a single-layer polydimethylsiloxane (PDMS) microchannel with sharp edges (Figure 1.1). When the piezoelectric transducer is excited, acoustic flexural waves are generated to oscillate sharp edges; this oscillation induces acoustic energy dissipation, leading to vibration streaming. The reason that separates vibrational micro-vortex streaming from surface acoustic wave induced streaming is that the sharp edges oscillate only near the resonance frequencies of the devices. Thus, sharp-

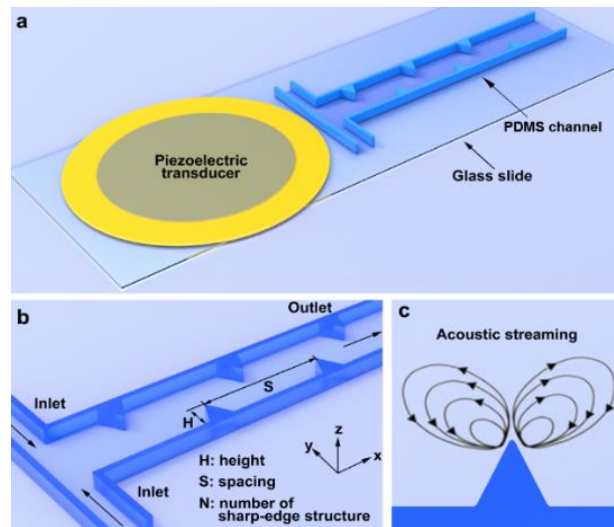


Figure 1.1: Micro-vortex streaming in sharp edge based acoustofluidic device. (a) Schematic of the sharp-edged based acoustofluidic micromixer device. (b) Schematic showing the detailed design of the sharp edge based microchannel. (c) Schematic showing the acoustic streaming effect induced by an acoustically oscillated sharp-edge structure. Photos reproduced from Zhao et al. in ref.²¹

edge vibration is a single oscillation mode, and a symmetrical micro-vortex pattern emerges for vibration streaming. Since it is the displacement of sharp edges scattered acoustic field that forms streaming flows, the streaming intensity can be tuned by modifying sharp edge structures, such as sharp-edge height (H), spacing (S) and the number of sharp-edge pairs (N) (Figure 1.1).

To date, the best way of characterizing vibration streaming is to track the trajectories of fluorescent particles. Using fluorescence microscopy, Huang et al., demonstrated the flow pattern of vibration streaming near sharp edge protrusion by tracing 1.9 μm diameter fluorescent particles at the device resonance frequency of 4.5 kHz.²⁰ Note that this resonance frequency is distinct from the resonance frequency of piezoelectric transducer. It has been experimentally observed that higher velocity streaming flows can be obtained using sharp edged with a larger height and a smaller sharp edge tip angle because such sharp edges will oscillate with higher amplitudes. This phenomenon can be illustrated by approximating sharp-edge oscillation as cantilever vibration, which is given as:²⁰

$$K = \frac{F}{\delta} = \frac{Ewt^3}{4L^3} \quad (1.12)$$

Here, K , δ , E , w , t , and L denote the spring constant, vibrational displacement, Young's modulus, cantilever width, cantilever thickness and cantilever length, respectively. When the material modulus E and thickness t are constant, a small angle tip (w) and a large height (L) lead to a small spring constant and a large vibration displacement.

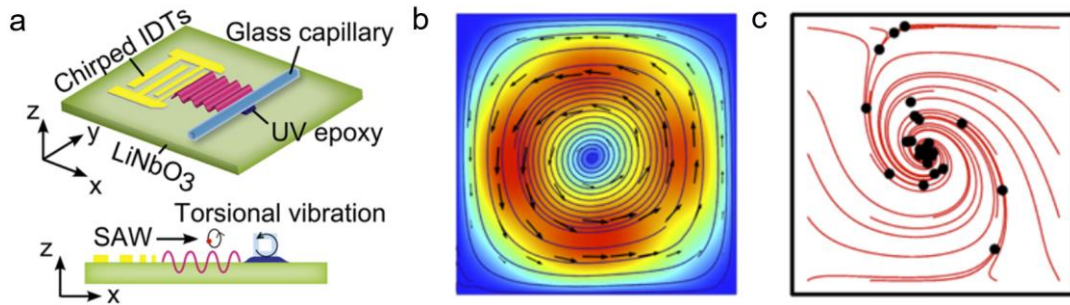


Figure 1.2: Micro-vortex streaming in surface acoustic wave devices (a) 3D view of the device. (b) simulated streamlines and velocity field for acoustic streaming. (c) simulated concentration of 500 nm polystyrene particles in fluids. Photos reproduced from Zhang et al. in ref.²²

Vibration streaming and cavitation streaming are both excited with flexural waves, though vibration streaming avoids the issue of bubble instability in cavitation streaming. Soft photolithography and PDMS materials can be used to fabricate different sharp edge based acoustofluidic devices that are operated within the frequency range of human hearing. Recent work has also demonstrated that higher frequencies in the MHz range can be applied to excite sharp edges fabricated from silicon materials, which minimize the amount of noise generated by sharp edge based acoustofluidic devices.

1.3.2. SAW Energy Dissipation Induced Streaming

Surface acoustic wave (SAW) induced streaming is the flow generated by viscous attenuation of acoustic energy in bulk fluids.¹¹ These devices consist of a lithium niobate substrate, a pair of interdigital transducers (IDTs), and a single-layer PDMS microchamber. When the transducers are excited, SAWs propagate on the surface of the lithium niobate and couples into the fluid at the solid/liquid interface. The acoustic

pressure amplitude decreases with distance from SAW source due to energy attenuation. This lossy energy transfer results in a steady momentum flux, leading to fluid circulation within the microfluidic channel.^{11, 18} Compared to vibration streaming, SAW induced streaming directly generates streaming via body forces and is applicable at a large frequency range (10-1000 MHz). The time-averaged acoustic body force at position (x, z) is expressed as:^{11, 23}

$$F_B = \rho_0 \beta U_1(x, z)^2 \quad (1.13)$$

$$U_1(x, z) = \xi_0 \omega e^{-\alpha(x - z \tan \theta_R)} e^{-\beta z \sec \theta_R} \quad (1.14)$$

Where β , U_1 , and θ_R are the fluid attenuation coefficient, the first-order amplitude of displacement velocity, and the Rayleigh angle, respectively.

It is important to note that, SAW induced streaming can also be demonstrated at low frequencies. For instance, Zhang et al. showed that at a frequency as low as 3.5 MHz, SAW induced torsional vibration mode could be harnessed to generate a single vortex within a glass capillary, as shown in Figure 1.2.²² However, in some scenarios, acoustic radiation force is preferred for separation of biological samples, which requires suppression of SAW streaming.

1.3.3. Topological Symmetry Broken Induced Chiral Vortex Feature

Originating from condensed matter physics, topological insulators have attracted tremendous attention because of their capability to overturn traditional view of wave propagation.²⁴ Among different topological materials, valley hall topological insulators

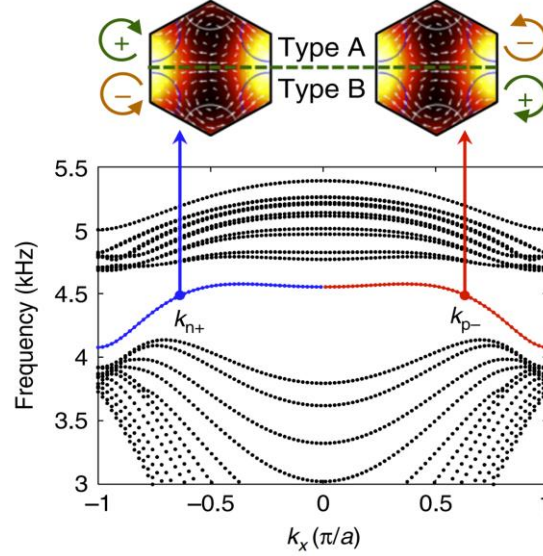


Figure 1.3: Chiral vortex of energy flux in topological phononic insulator. (Top) chiral vortex feature of edge states projected from different valleys. The color and arrows represent energy field and Poynting energy flow, respectively. (bottom) dispersion curves for topological edge states. Photos reproduced from Tian et al. in ref.²⁵

are extremely promising, as they can be easily realized by spatial inversion-symmetry broken. In addition to spin and charge, the valley provides a new degree of freedom for electrons. When the inversion symmetry is broken, the berry curvatures localized at K or K' valleys show non-trivial features and carry opposite signs.²⁴ Thus, electrons at different valleys obtain opposite velocities and move in opposite directions. When extended to phononic and photonics, this movement in opposite directions is characterized as the chiral vortex feature of energy flux at different valley points (Figure 1.3). The non-trivial berry curvature of topological materials can be estimated from eigenvalue problem of periodic lattice in momentum space, given as:^{26, 27}

$$H(\mathbf{k}) \psi_n(\mathbf{k}) = \lambda_n(\mathbf{k}) \psi_n(\mathbf{k}) \quad (1.15)$$

where $\psi_n(k)$ represents an eigenstate of the n th band at k . When k varies slowly along the band in the Brillouin zone, the system's evolution is defined as Berry phase:^{26, 27}

$$\phi_n = \oint \mathbf{A}_n(k) \cdot d\mathbf{k} \quad (1.16)$$

$$\mathbf{A}_n(k) = i \left(\psi_n(k) \left| \frac{\partial}{\partial R} \right| \psi_n(k) \right) \quad (1.17)$$

Here $\mathbf{A}_n(k)$ is termed as Berry connection and the curl of $\mathbf{A}_n(k)$ is Berry curvature:²⁶

$$\Omega_n(\mathbf{R}) = \nabla_{\mathbf{R}} \times \mathbf{A}_n(\mathbf{R}) \quad (1.18)$$

To date, valley related unconventional topological phenomena such as the valley hall effect,¹⁹ backscattering-immune wave propagation²⁴ and negative refraction²⁸ have been demonstrated. However, these investigations are mainly limited to solid domain or air domain. Fluids are another important medium for the life science; however, few wave propagation investigations have been done in fluids due to the difficulty of on-chip fabrication and complexity of solid-liquid coupling. In this dissertation, we will explore the generation of chiral vortex feature of topological insulators in fluids.

1.4. Applications of Micro-Vortex Streaming

In this section, we will summarize various applications achievable by suppressing or enhancing micro-vortex streaming. These applications are classified into (1) fluid manipulation using vibration streaming; (2) particle manipulation using micro-vortex streaming; and (3) particle manipulation via suppression of SAW streaming.

1.4.1. Fluid Manipulation Using Vibration Streaming

Vibrational micro-vortex streaming flows are generated at the tip of oscillating sharp edges with extremely high tunability.²⁰ By varying the structure and position of these sharp edges it is possible to achieve different vibrational streaming modes over a wide range of intensities. Vibrational micro-vortex streaming can be achieved in fluid flows spanning the entire microfluidic channel, as well as localized fluid flows. The two important applications of this vibrational micro-vortex streaming technology are fluid mixing and fluid pumping, both of which are essential functionalities for lab-on-a-chip applications and fully microfluidic analytic systems. This section will discuss these two applications along with other novel fluid manipulation applications.

First, Huang et al., demonstrated that vibrational micro-vortex streaming can be achieved in the vicinity of sharp edges within acoustic microfluidic channels, and this streaming can be harnessed to generate mixing by disturbing laminar fluid flow.²⁰ This effect was achieved using vertical, triangular sharp edges alternatively spaced along two opposing channel walls. By varying the acoustic frequency and driving voltage across the channel, they were able to achieve complete mixing in a fluid flowing at a rate of 4 $\mu\text{L}/\text{min}$. Meanwhile, numerical simulation indicated that sharp edges placed directly opposite each other would lead to incomplete mixing. This micro-vortex streaming and fluid mixing is also shown in their later work (Figure 1.4).^{29, 30} A clear interface between laminar flows is observed while the acoustics are off; however, complete mixing

is demonstrated by a uniform fluorescence intensity within the microchannels when the acoustic transducer is turned on. Unfortunately, despite its simplicity and stability, this sharp edge-based micromixer suffers from low throughput.

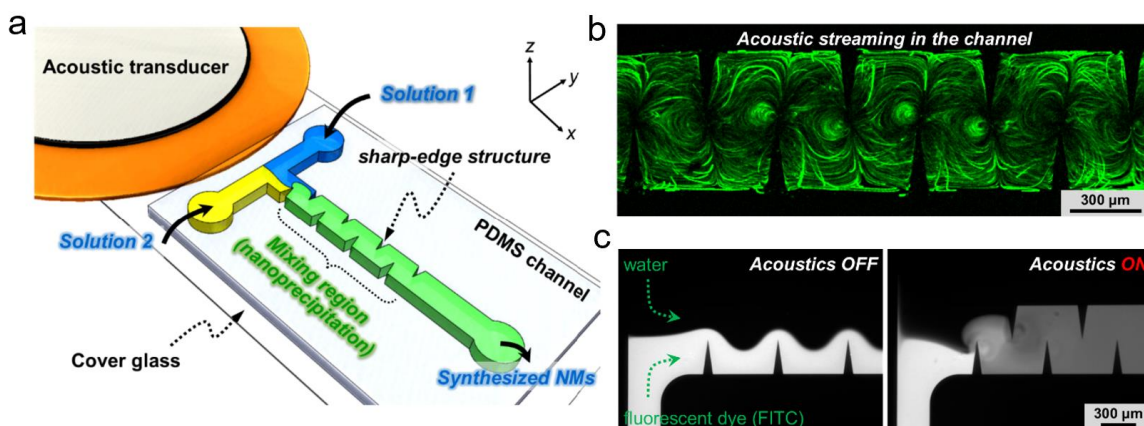


Figure 1.4: Fluid mixing in sharp edge based acoustofluidic devices. (a) schematic for the sharp edge-based device. (b) vibration micro-vortex streaming characterized by the trajectories of fluorescent particles. (c) mixing of DI water and fluorescent dye within microchannels. Photos reproduced from Huang et al. in ref.²⁹

Next, fluid pumping within microfluidic channels allows the development of point-of-care devices with the minimal external hardware. Due to the symmetrical pattern, vibration streaming has attracted few attentions for fluid pumping. By designing a rightward-tilted, rectangular sharp edges on channel side walls, Huang et al., were able to generate a net force that resulted in a pump flow rate of $8 \mu\text{L min}^{-1}$ with a pressure of 76 Pa. This pumping was realized by placing tilted sharp edges to the right so as to direct a net force toward right.³¹ This directional pumping flow can presumably be used to transport biological samples such as cell, virus and exosomes. Additionally, a

spatiotemporally controlled chemical generator was developed by this research team by placing sharp edges in the middle of microfluidic channels.

1.4.2. Particle Manipulation Using Micro-Vortex Streaming

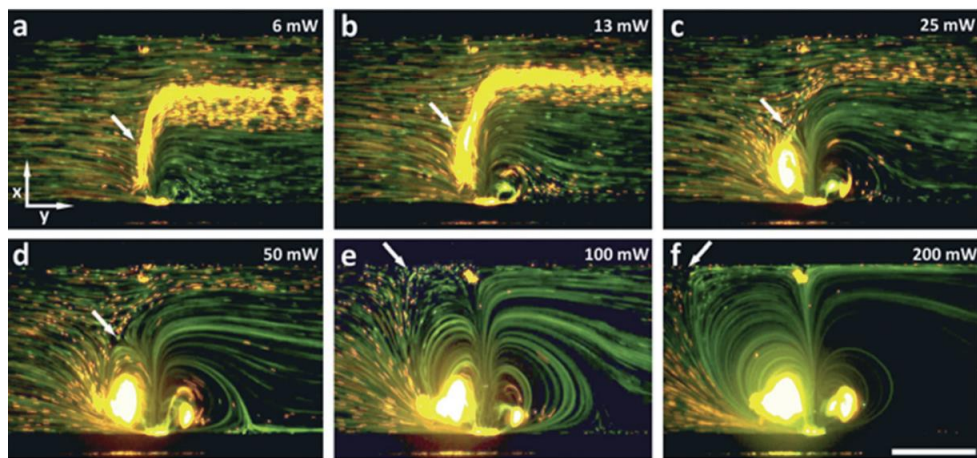


Figure 1.5: SAW induced micro-vortex streaming for selectively particle capture. (a-c) at low powers, the 2 μm (orange) particles are deflected away from the focused SAW beam. (d-f) at high powers, the 2 μm (orange) particles are trapped in the vortex center while the 1 μm (green) particles flow follow the streamlines. Scar bar: 200 μm . Photos reproduced from Collins et al. in ref.³²

Concentration and separation of biological samples, such as circulating tumor cells (CTCs) and exosomes, are essential to diseases diagnostics.^{33, 34} Micro-vortex streaming generated in the vicinity of focused SAW beams or oscillating structures have both been used to capture and concentrate large particles, while allowing small particles to continue flowing along streamlines.^{32, 35} This differential behavior allows for particle separation based on size. Recently, Collins et al., have investigated the capture efficiency and differentiation capability of SAW streaming for particles and cells within a 400 μm PDMS microchamber.³² They found that within a given system, the SAW streaming pattern

depended on driving power and lateral fluid flow rate. By varying the power and flow rate, they were able to selectively separate 2 μm PS particles from 1 μm particles, as well as isolate human breast cancer cells from red blood cells (Figure 1.5). However, one limitation of SAW streaming is that it is relatively weak, with a maximum sample flow rate of only 2 $\mu\text{L min}^{-1}$. In contrast, bubble oscillation-induced streaming is much stronger. Using bubble oscillation induced micro-vortex streaming, Jiang et al., were able to separate CTCs and circulating cancer associated fibroblasts (cCAFs) from clinical blood samples without damaging cell integrity.³⁵ To do so, they actuated a piezoelectric transducer at a frequency of 50.2 KHz, and were able to obtain high flow rates up to 70.4 $\mu\text{L min}^{-1}$. Despite these achievements, the stability of air bubble systems remains a concern.

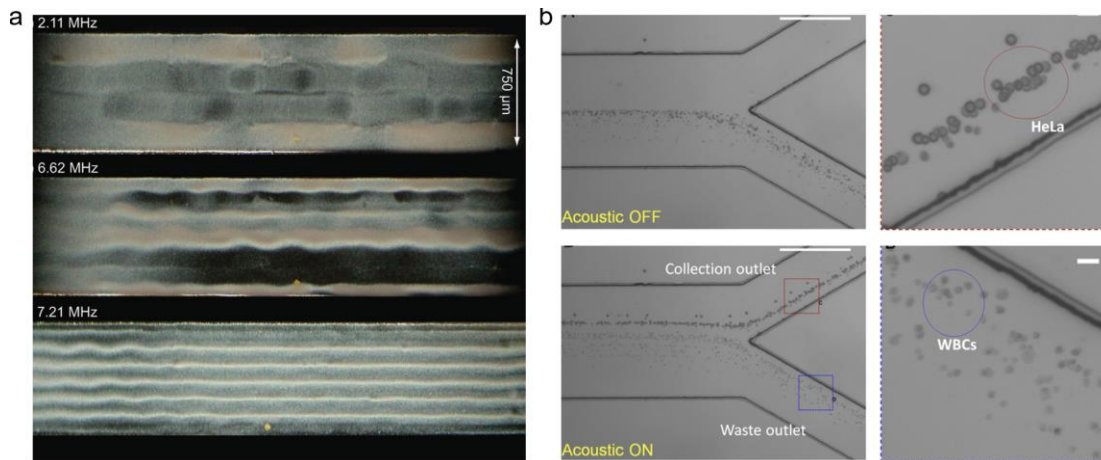


Figure 1.6: The suppression of micro-vortex streaming for particle manipulation. (a) The disappearance of Rayleigh streaming micro-vortices with the increment in standing pressure fields. Photos reproduced from Wiklund et al. in ref.¹⁸ (b) Standing surface acoustic waves are used for cell separation driven by acoustic radiation force. Photos reproduced from Li et al. in ref.³⁶

1.4.3. Particle Manipulation by Suppressing Micro-Vortex Streaming

Development of SAW streaming also include direction to suppress micro-vortex streaming and enhance acoustic radiation force for cell or particle manipulation.^{18, 36} The acoustic radiation force and acoustic streaming co-exist together in microfluidic channels. The question of which effects dominates depends on their respective intensities as they relate to particles. Therefore, two methods can be applied to overcome streaming. Firstly, standing acoustic wave fields can be constructed to partially cancel out momentum flux in opposite direction (Figure 1.6). Secondly, a large acoustic radiation force can be generated so as to overwhelm the effect of acoustic streaming. For the first method, Figure 1.6a shows how the generation of a standing wave can be used to significantly reduce acoustic streaming. At 2.11 MHz with a channel width of λ , Rayleigh streaming with a characteristics wavelength of $\lambda/4$ can be clearly observed, resulting in local particle depletion near each vortex. At 6.62 MHz with a channel width of 3λ , the acoustic radiation force can be observed in the particles' patterning. At 7.21 MHz with a channel width of 3.5λ , particle patterning clearly follows standing wave pressure fields and no Rayleigh streaming is evident. For the second method, Collins et al., found that in the same SAW device, $2\ \mu\text{m}$ PS particles were deflected by traveling wave force at low powers, while $2\ \mu\text{m}$ PS particles were captured by acoustic micro-vortex streaming at high powers.³² In Chapter 4, we will propose a new strategy to increase the acoustic radiation force while rendering the micro-vortex streaming effect negligible.

1.5. Dissertation Outline

In the remaining sections, I will discuss the enhancement of vibration streaming in chapters 2 and 3, the suppression of streaming by increasing acoustic radiation force in chapter 4; and the development of chiral vortex streaming in chapter 5. I will provide a summary in chapter 6. The contents of this dissertation are reproduced from published works and manuscript in preparation.

Chapter 2 of this dissertation is from the publication: Shuaiguo Zhao, Weihua He, Zhehan Ma, et al., *On-chip stool liquefaction via acoustofluidics*, *Lab on a Chip*, 19, 941-947, 2019. We have also included two figures from another publication into this chapter: *Lab on a Chip*, 21, 2453-2463, 2021.

Chapter 3 of this dissertation is from two publications: Shuaiguo Zhao, Po-Hsun Huang, Heying Zhang, et al., *Fabrication of tunable, high-molecular-weight polymeric nanoparticles via ultrafast acoustofluidic micromixing*, *Lab on a Chip*, 21, 2453-2463, 2021. Po-Hsun Huang*, Shuaiguo Zhao*, Hunter Bachman, et al., *Acoustofluidic synthesis of particulate nanomaterials*, *Advanced Science*, 1900913, 2019.

Chapter 4 of this dissertation is from one publication: Shuaiguo Zhao, Mengxi Wu, Shujie Yang, et al., *A disposable acoustofluidic chip for nano/micro particle separation using unidirectional acoustic transducers*, *Lab on a Chip*, 20, 1298-1308, 2020.

Chapter 5 of this dissertation is from one manuscript ready to be submitted: Shuaiguo Zhao, Zhenhua Tian, Chen Shen, et al., *Topological Acoustofluidics*, in preparation, 2022.

Chapter 6 of this dissertation contains a summary and potential directions for future work. I will discuss current limitations in micro-vortex streaming technologies and future research directions for topological acoustofluidics.

2. On-Chip Stool Liquefaction via Acoustofluidics

Microfluidic-based portable devices for stool analysis are important for detecting established biomarkers for gastrointestinal disorders and understanding the relationship between gut microbiota imbalances and various health conditions, ranging from digestive disorders to neurodegenerative diseases. However, the challenge of processing stool in microfluidic devices hinders the development of a standalone platform. Here, we present the first microfluidic chip that can liquefy stool samples via acoustic streaming. With an acoustic transducer actively generating strong micro-vortex streaming, stool samples and buffers in microchannel can be homogenized at a flow rate up to 30 $\mu\text{L}/\text{min}$. After homogenization, an array of 100 μm wide micropillars can further purify stool samples by filtering out large debris. A favorable biocompatibility was also demonstrated for our acoustofluidic-based stool liquefaction chip by examining bacteria morphology and viability. Moreover, stool samples with different consistencies were liquefied. Our acoustofluidic chip offers a miniaturized, robust, and biocompatible solution for stool sample preparation in a microfluidic environment and can be potentially integrated with stool analysis units for designing portable stool diagnostics platforms.

2.1. Motivation

Owing to the fact that stool samples are rich in constituents including bacteria,³⁷ cells,³⁸ biomarkers,³⁹ and viruses⁴⁰, processing and analyzing stool is essential to numerous disease diagnoses. For example, stool cultures enable the detection of pathogenic bacteria

for diarrheal diseases,⁴¹ while stool immunochemical tests contribute to the screening of colorectal cancer.⁴²⁻⁴⁴ In addition to conditions directly affecting the digestive tract, researchers have recently linked irregularities in gut microbiota with the risk and progression of neurodegenerative diseases such as Alzheimer's and Parkinson's disease.⁴⁵ ⁴⁶ However, current stool processing and analysis protocols not only require highly trained personnel and advanced instrumentation, but are also labor-intensive and time-consuming, thus limiting patients' access and lowering medical care efficiency. Additionally, the need for cross-instrumentation operation may lead to severe biohazard risks and operator-dependence can compound detection results.⁴⁷ Therefore, the development of rapid, reliable, and automated point-of-care (POC) devices for stool processing and analysis is critical for reducing biosafety concerns and improving diagnoses and healthcare.

The unique features of microfluidics, such as miniaturization, biohazard containment, high sensitivity, and reduced reagent consumption, make it excellent candidate for developing POC devices for stool processing and diagnosis.^{30, 48-67} Previously, microfluidic devices have demonstrated advances in stool analysis, ranging from on-chip detection of antigen^{68, 69} and bacteria,^{70, 71} and on-chip polymerase chain reaction (PCR)⁷² to molecular analysis of nucleic acids.^{73, 74} Despite these achievements, most microfluidic devices require off-chip stool processing, including vortex mixing for homogenization, and filtration or centrifugation for purification.^{68-70, 72, 74} These off-chip

requirements severely hinder microfluidics from evolving into next-generation fully automated POC devices, for which integration of stool processing and analysis is imperative. Currently, there are no on-chip methods that can perform stool homogenization and subsequent purification. For traditional microfluidic mixing methods which primarily rely on the design of channel structures,^{75, 76} the absence of external energy and weak mixing make it extremely challenging to liquefy stool samples, considering the large number of macromolecules and non-digested matter in stool.

In this work, we present the first on-chip method that can homogenize and purify complex stool samples. In the homogenization region, with an acoustic transducer actively oscillating sharp-edges in microchannel, strong micro-vortex streaming can be created to homogenize stool samples and phosphate buffered saline (PBS) at a flow rate of up to 30 $\mu\text{L}/\text{min}$. In the purification region, an array of 100 μm wide microstructures was designed as a filter to remove large debris. The chip demonstrates comparable biocompatibility to the standard method when considering the bacteria's integrity, viability, and proliferation ability. Our device's high biocompatibility, along with its continuous flow nature, are important for downstream applications that often require intact cells, such as cell culture,⁷⁷ flow cytometry,^{78,79} and cell detection.^{71,80,81} Furthermore, the strong acoustic streaming enables the liquefaction of stool samples with a large range of consistency. With its robust, biocompatible, and versatile nature, our acoustofluidic chip could provide a viable pathway to the adoption of microfluidics in stool research and

could also be integrated with other microfluidic units to expedite the development of portable tools for stool processing and analysis.

2.2. *Materials and Methods*

2.2.1. Stool Sample

Human stool samples were collected from a volunteer according to a protocol (2019-0115) approved by the Duke University Institutional Review Board. Informed, written consent has been obtained by the volunteer.

2.2.2. Fabrication and Operation of Acoustofluidic Devices

Figures 2.1A&B provide a schematic and photo of our sharp-edge-based acoustofluidic device for stool liquefaction, respectively. This acoustofluidic stool liquefier consists of an acoustic transducer, a glass slide, and a single-layer polydimethylsiloxane (PDMS) microchannel. The microchannel with sidewall sharp-edge structures was fabricated using deep reactive ion etching and a replica-molding technique, and then bonded onto a glass slide. Next, an acoustic transducer (AB2720B-LW100-R, PUI Audio, Inc., USA) was bonded onto the same glass slide using a thin epoxy layer (PermaPoxy™ 5 Minute General Purpose, Permatex, USA). The vibrations from the transducer oscillate the sharp

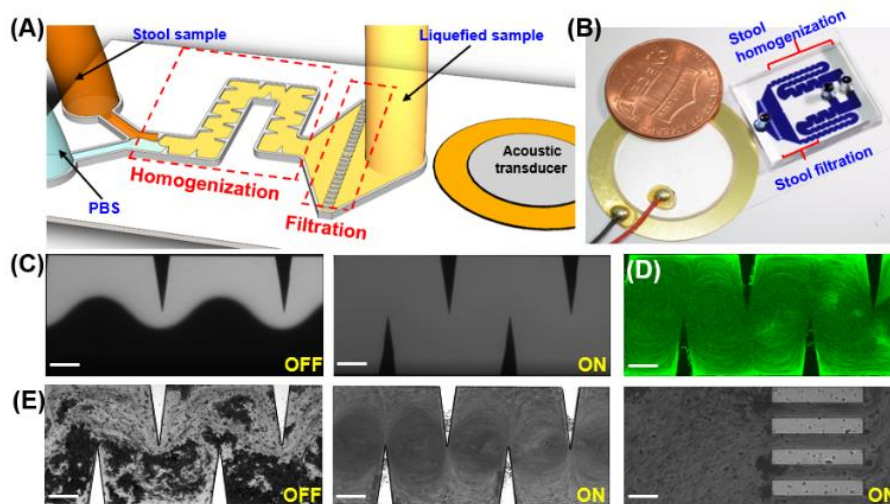


Figure 2.1: Device operation principle of micro-vortex streaming. (A) Schematic and (B) photograph of the acoustofluidic-based stool liquefier device. (C) Characterization of high-performance mixing of DI water and fluorescent dye at 40 V_{PP} and a total flow rate of 250 $\mu\text{l}/\text{min}$ (125 $\mu\text{l}/\text{min}$ in each parallel channel). With acoustics off (left), a laminar flow was observed and with acoustics on (right), complete mixing was obtained. (D) Characterization of strong acoustic micro-vortex streaming at 40 V_{PP} and a total flow rate of 200 $\mu\text{l}/\text{min}$ (100 $\mu\text{l}/\text{min}$ in each parallel channel). (E) The stool liquefaction process was shown as follows: with the acoustics off (left), a laminar flow of stool sample and PBS flowed through the microchannel; with the acoustics on (center), strong acoustic micro-vortex streaming was created to mix stool samples; at the end of the channel (right), an array of 100 μm parallel microchannels designed as filters to remove large debris. Scale bar: 200 μm .

edges, and create acoustic micro-vortex streaming which mixes the fluids in the channel.

The chip can be segmented into two functional domains: a homogenization region and a filtration region (Figures 2.1A&B). The former refers to a serpentine microchannel section decorated with sharp-edge structures that serve to liquefy stool samples, and act as the surrogate for the standard vortex mixer to produce a homogenous sample (Figure 2.1A and Figure 2.2); the latter denotes an array of parallel 100 μm wide microchannels that

function as an alternative to the standard filter to remove large stool debris (Figure 2.1A and Figure 2.2).

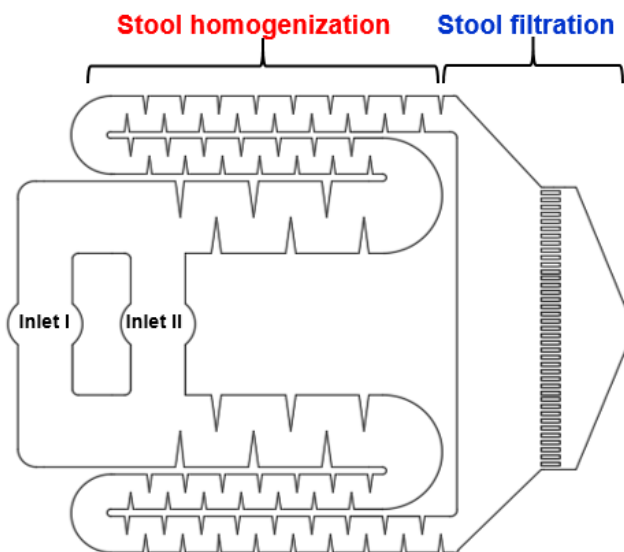


Figure 2.2: Detailed design of the acoustofluidic-based stool liquefaction device. In order to prevent clogging due to the thick stool sample, the stool homogenization region was designed with two parallel channels where width of large channel and small channel sections were 2 and 1 cm, respectively. Additionally, a 2.5 cm diameter puncher (Kai, Japan) was used to punch the inlets and outlet. In the stool filtration region, the gap between the microstructures is 100 μm .

To operate our acoustofluidic device, stool samples were first diluted in sterile PBS (20012-027, Life Technologies, USA) at a concentration of 500 mg/ml and incubated at 4 °C for 1 hr. After that, stool samples and PBS were co-injected into our acoustofluidic device through two distinct inlets using two 10 mL BD syringes and MicroLine™ tubing (59-8645, 1.3 mm ID and 2.3 mm OD, Harvard Apparatus, USA); the injection process was controlled by a syringe pump (neMESYS, Germany). While the liquids were being injected into the device, the acoustic transducer was activated at a voltage of 40 V_{PP} and a

frequency of 4.0 kHz using a signal generated by a function generator (AFG3011, Tektronix, USA) and magnified by an amplifier (25A250A, Amplifier Research, USA). Due to the strong acoustic streaming produced by the sharp edges, stool samples and PBS flows were homogenously mixed as they moved through the “liquefaction region”; the mixture then entered the “filtration region” where it was purified and large debris was removed.

Before the liquefaction of stool samples, we first optimize the device performance. To characterize the mixing performance of our device, DI water and fluorescent dye were injected through independent inlets into the microchannel. Unless otherwise specified, the flow rates of DI water and fluorescent dye were both 15 $\mu\text{L}/\text{min}$ (30 $\mu\text{L}/\text{min}$ in total). The mixing performance was then quantitatively characterized by the standard deviation of normalized gray scale values. Here, we systematically investigate the influence of the device parameters (PDMS thickness, glass thickness, and sharp-edge number, height, and distance) and the operation parameters (driving frequency and voltage) on the mixing performance. The microchannel for all experiments was 100 μm high, 600 μm wide, and 1 cm long, and the tip angle of sharp-edges were fixed to 15°. The No. 1 (130-170 μm , 48404-453, VWR, USA) and No. 2 (170-250 μm , 48382-136, VWR, USA) cover glasses were purchased from VWR, while the No. 0 cover glasses were purchased from Thor Labs (85-115 μm , CG00K1, Thorlabs, Inc., USA).

2.2.3. Standard Stool Liquefaction Procedure

In order to provide a benchmark comparison for our acoustofluidic liquefaction device, we also processed samples using a standard method. When reviewing the standard methods for stool liquefaction, we found that stool samples are first diluted in PBS with a concentration range of 50-500 mg/ml, homogenized via a vortex mixer, and finally filtered or centrifuged for purification.^{72, 82-85} Based on the standard procedure, we conducted the following three-step procedure for comparison to our acoustofluidic method. First, stool samples were diluted in sterile PBS with a concentration of 500 mg/ml and then incubated at 4 °C for 1 hr (this mirrored the incubation time of the acoustofluidic liquefaction process). Second, 1 min vortex mixing (Geneate, VWR, USA) was applied to a mixture of the stool sample and additional PBS that had been added at a 1:1 ratio (v/v), followed by 20 min incubation at room temperature. Third, the processed sample was filtered with a 100 µm sterile filter (22363549, Fisher Scientific Inc., USA) to remove large stool debris.

2.2.4. Morphology Characterization

Scanning electron microscopy (SEM) and optical microscopy were used to compare the performance of the two stool liquefaction methods based on debris size. For SEM imaging, the liquefied stool samples were first centrifuged and then re-suspended with a fixative solution. After incubating at 4 °C for 24 hrs, a drop of stool sample was

placed on an aluminum stub coated with a carbon adhesive tab, dried at room temperature, and sputtered with a thin layer of gold.

2.2.5. Bacterial Cell Culture

Stool culture was performed to evaluate the influence of the liquefaction procedure on the bacteria's proliferation ability. Culture medium was prepared by dissolving 7.5 mg eosin methylene blue (EMB) agar (70186, Sigma, USA) in 200 mL DI water. After transferring 20 mL culture medium into a 100 x20 mm culture dish (353003, Falcon, USA), 0.5 μ L of the sample was inoculated on an EMB agar plate following a "DUKE" pattern. Samples included the acoustically liquefied stool sample, standard liquefied stool sample, and a control with only PBS. The cultures were incubated aerobically at 37°C, and bacterial growth was examined at 18 and 36 hrs, respectively.

2.2.6. Bacterial Viability via Fluorescence Microscope and Flow Cytometry

To analyze cell viability with a fluorescence microscope, stool samples liquefied using either a standard method or our acoustofluidic device were using a commercial staining kit (Live/Dead BacLight, L7007, Invitrogen, USA). After 15 min incubation in dark at room temperature, a 2 μ L drop of each liquefied stool sample was placed on an agarose pad to immobilize the bacterial cells.⁸⁶ Then, the agarose pad was analyzed using an inverted microscope (Eclipse Ti, Nikon, Japan) equipped with a 100X oil immersion objective.

In order to analyze cell viability with a flow cytometer, the liquefied stool sample was first filtered with a 5 μm filter (7037350, Sterlitech, USA) to isolate bacterial cells and then stained with a Live/Dead BacLight kit (L34856, Invitrogen, USA). After a 15 min incubation, 10 μL of liquefied stool sample was diluted with 987 μL of PBS and then transferred to a 5 mL tube with cell-strainer cap (352235, Falcon, USA) for flow cytometry (BD FACSCanto B, USA). *Escherichia coli* (*E. coli*) bacterial cells purchased from ATCC were cultured in Miller's LB Broth (20716002, Cellgro, USA) and used for flow cytometry condition setting.

2.3. Results and Discussion

2.3.1. Rational Acoustofluidic Design to Improve Mixing Performance

Prior to stool liquefaction, the strong acoustic micro-vortex streaming effect, generated by our acoustofluidic device, was characterized. In Figure 1C, driven at a frequency of 4.0 kHz and an input voltage of 40 V_{PP} , our device was able to completely mix two laminar fluids of DI water and fluorescent dye at a total flow rate of 125 $\mu\text{L}/\text{min}$. In Figure 1D, at 4.0 kHz and 40 V_{PP} , clear acoustic streaming patterns were developed at a total flow rate of 100 $\mu\text{L}/\text{min}$ (for each parallel channel). This complete mixing and clear streaming pattern at a high flow rate demonstrates the capability of our device to create strong acoustic streaming, which endows it with the potential for stool liquefaction. Due to the viscous and inhomogeneous nature of stool samples, to perform stool liquefaction we introduced, stool samples and PBS into our acoustofluidic device at the same flow rate

of 15 $\mu\text{L}/\text{min}$ (total flow rate of 30 $\mu\text{L}/\text{min}$). Figure 1E presents the working process of our acoustofluidic stool liquefier. With acoustics off, the stool sample flows adjacent to PBS following a laminar pattern; we noted that some of the large stool debris is able to break the laminar barrier and reach the top of the channel due to its size and inertial effect. With acoustics on, the oscillations of the sharp edges cause the stool sample to be homogenized with the PBS via strong acoustic streaming in the homogenization region. At the end of the microchannel (*i.e.*, the filtration region), large debris and highly viscous portions of stool samples were filtered. Once the device was working steadily, a 1.5 mL centrifuge tube was used for collecting the liquefied sample over a 20 min period. Meanwhile, a portion of the same sample was liquefied using the standard procedure (*i.e.*, vortex mixing and a 100 μm sterile filter).

To realize the above-mentioned mixing performance, we enhanced the acoustic micro-vortex streaming by designing rational device parameters. We first determined the driving frequency by sweeping the input frequency from 2 kHz to 6 kHz with a minimum 100 Hz increment. The mixing performance was quantitatively characterized by the mixing index (M) in Figure 2.3 based on Equation 1^{20, 87}:

$$M = \sqrt{\frac{1}{n} \sum_{i=1}^n \left(\frac{I_i - I_m}{I_m} \right)^2} \quad (2.1)$$

Here, n , I_i , and I_m represent the sampled points along a line, the gray scale value of a point, and the averaged gray scale value of the line, respectively. A M of 0.1 is the cut off value for complete mixing, while M values of 0.0 and 0.5 correspond to completely

mixed and unmixed fluids, respectively.²⁹ When excited with a 3.9 kHz signal, devices achieved the lowest M of 0.05. As such, 3.9 ± 0.2 kHz was chosen as the driving frequency range to excite the different devices; the small frequency range was adopted due to the slight frequency shifts required for excitation of devices with different design parameters.

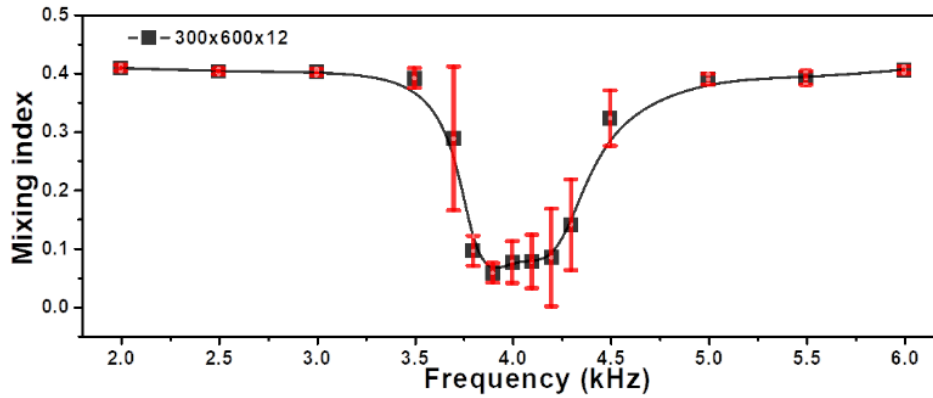


Figure 2.3: Dependence of mixing performance on driving frequency. The driving voltage is 25 V_{PP} and the total flow rate is 30 μ L/min. The device tested has a sharp-edge structure of 300 \times 600 \times 12, a glass thickness of 170-250 μ m, and a PDMS thickness of 4 mm.

Then, the influence of sharp-edge design was evaluated. Figure 2.4A shows that devices with sharp-edge height (H) of 300 μ m always retain the best mixing performance. This phenomenon is ascribed to larger vibration displacement in devices with larger H.²⁰ In Figure 2.4B, devices with a moderate sharp edge spacing (S) of 600 μ m show the best mixing performance. Considering the fixed length range of sharp-edges, a large S reduces the mixing sites and thus compromises the mixing performance, while a small S generates micro-vortex streaming close to each other and can suppress acoustic streaming. In Figure 2.4C, with increased sharp-edge pairs and mixing sites, N, the mixing performance is gradually improved. Although there is almost no difference between N=8 and 12 in Figure

2.4C, devices with $N=12$ was selected due to its slightly better performance at certain conditions, such as complete mixing at $35 \mu\text{L}/\text{min}$ and $25 V_{pp}$. With the determined sharp-

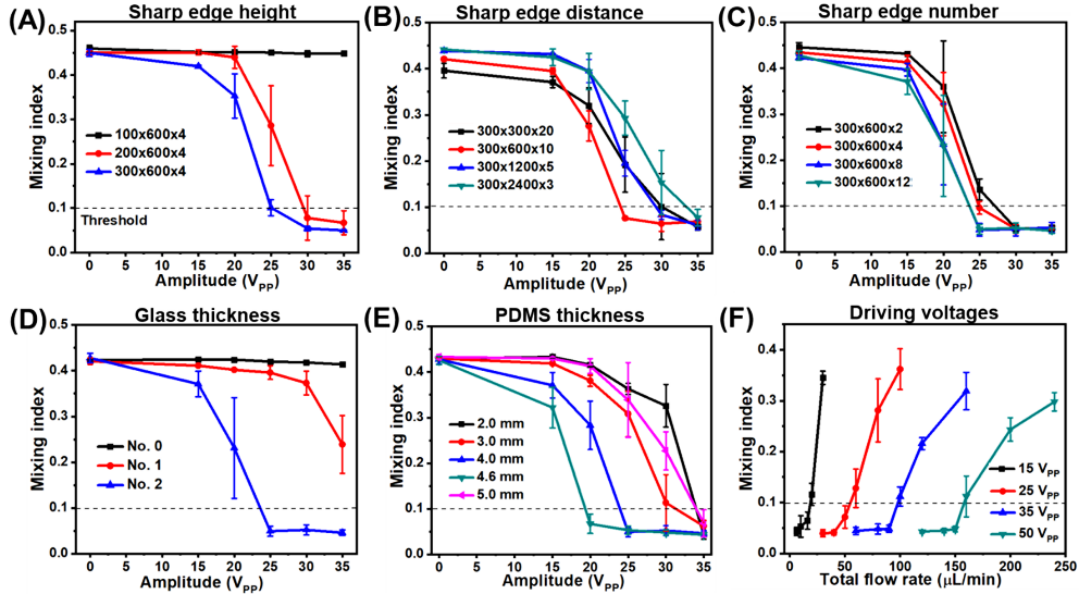


Figure 2.4: Rational design of device parameters by the characterization of mixing performance of the acoustofluidic devices. Plots of mixing indexes at different driving voltages with (A) different sharp-edge heights, (B) spacing between sharp-edges, and (C) different numbers of sharp-edge pairs. Here, 4 mm thick PDMS, No. 2 glass, and $30 \mu\text{L}/\text{min}$ total flow rate are applied for (A, B, and C). Plots of mixing indexes with different device and operation parameters: (D) glass thickness with 4 mm thick PDMS, (E) PDMS thickness with No. 2 glass, and (F) driving voltage with 4.6 mm thick PDMS and No. 2 glass. The sharp-edge structure is $300 \times 600 \times 12$ for (D, E, F) and the total flow rate is $30 \mu\text{L}/\text{min}$ for (A, B). The thickness is 85-115 μm , 130-170 μm , and 170-250 μm for No. 0, No. 1, and No. 2 glasses, respectively. The sharp-edge structure, depending on the height (H) in μm , spacing (S) in μm , and number of sharp-edge pairs (N), is denoted as $H \times S \times N$. Data represents average of $n = 3$ independent devices \pm standard deviation.

edge structure of $300 \mu\text{m} \times 600 \mu\text{m} \times 12$ pairs, we further investigated the influence of glass thickness, PDMS thickness, and driving voltages. From Figure 2.4D and 4E, the mixing performance strongly depends on the glass and PDMS thickness. The best performance appears at 170-250 μm thickness for No.2 glass and 4.6 mm thickness for PDMS. The

influence of glass and PDMS thickness can be understood by approximating the vibration of the acoustofluidic devices as a harmonic motion. As the PDMS thickness (mass) is increased, its vibration frequency decreases.⁸⁹ At a suitable thickness of glass and PDMS, the vibration frequency of the system matches well with the excitation frequency, and strong resonance vibration mode appears. Due to the resonance behavior, the mixing performance of the system depends non-linearly on device parameters. Devices with $300\ \mu\text{m} \times 600\ \mu\text{m} \times 12$ pairs, 4.6 mm PDMS, and No. 2 (170-250 μm) glass were subsequently applied. In Figure 2.4F, with increasing voltages, the maximum flow rate for complete mixing was 90 $\mu\text{L}/\text{min}$ at 35 V_{PP} and 150 $\mu\text{L}/\text{min}$ at 50 V_{PP} , respectively. These results indicate that our acoustofluidic device can provide strong micro-vortex streaming.

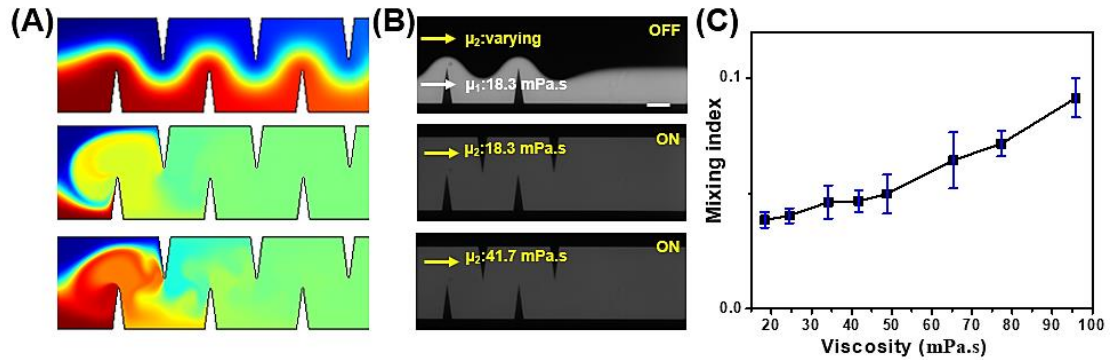


Figure 2.5: Numerical simulation and experimental results for mixing investigation of viscous PEGDA700 polymer solution. (A) Numerical simulations of PEGDA700 concentration profile for unmixed 18.3 mPa.s flow, mixed 18.3 mPa.s flow, and mixed 41.7 mPa.s flow, respectively. (B) Experimental results showing the mixed performance from acoustics off to acoustics on, where μ_1 is kept at 18.3 mPa.s and μ_2 is varied. When the acoustics are off, laminar flow is observed with a μ_2 of 18.3 mPa.s. When the acoustics are on, fluid μ_1 is completely mixed with μ_2 at 18.3 and 41.7 mPa.s, respectively. Scale bar: 200 μm . (C) Plot of mixing indexes for mixed PEGDA700 solutions versus varying viscosities of μ_2 .

Considering the high viscosity of the stool samples, the performance of the rational acoustofluidic devices was further verified by numerical and experimental investigation of the mixing between viscous PEGDA700 and water solutions. Based on the perturbation approach developed in our previous publications,^{17, 90} the simulation was performed using COMSOL 5.3 (the COMSOL Group). The viscosity of PEGDA700 is 95.9 mPa.s, which is much higher than that of water (0.89 mPa.s)⁹¹ and that of PLGA solution (6.7 mPa.s for 33K PLGA).⁹² We diluted the PEGDA700 solutions from 0% to 50% using DI water before the on-chip acoustofluidic mixing.⁹¹ For all measurements, the driving voltage is kept at 50 V_{PP}, and the total flow rate was fixed at 6 μ L/min. A 50% PEGDA-water solution (viscosity 18.3 mPa.s) was injected into one inlet as μ_1 , while PEGDA solution with varying concentrations was injected into another inlet as μ_2 . Due to the difference of dynamic viscosity between μ_1 and μ_2 , the ratio of the flow rate of the two fluids was changed to ensure that the interface of laminar flow was at the middle of the channel.

In Figure 2.5A, the numerical simulation demonstrates that the acoustic streaming in our device can mix highly viscous PEGDA700 polymers. The speed of sound, compressibility of the fluid, and the density for PEGDA700 solution is *ca.* 1,603 m/s, 3.47×10^{-10} Pa⁻¹, and 1,120 kg/m³, respectively.^{93, 94} Meanwhile, PEGDA700 is considered as an incompressible fluid in the simulation model. This prediction is confirmed by the concentration profile of unmixed and mixed PEGDA700 solutions in Figure 2.5B. Figure 2.5C shows the mixing indexes for eight various PEG700-water solutions (18.3-95.9

mPa.s). For all PEGDA700 solutions, the mixing index is below 0.1, indicating complete mixing. These results confirm the capability of our acoustofluidic device to mix highly viscous solutions.

2.3.2. Visual Comparison

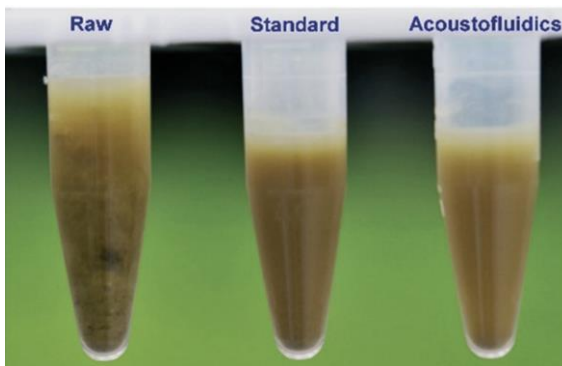


Figure 2.6: Photo of visual observation of human stool samples. “Raw”: an un-liquefied raw stool sample; “Standard”: a liquefied stool sample processed using the standard method (i.e., vortex mixing and a 100 μm sterile filter); “Acoustofluidics”: a liquefied stool sample prepared using our acoustofluidic device.

After liquefaction, we first visually compared the raw stool sample and liquefied stool samples. Due to the presence of macromolecules, particulates, and non-digested matters, the non-liquefied stool sample (i.e., the raw stool sample) was cloudy and contained flocculation, as shown in Figure 2.6. Both liquefied stool samples have a clearer appearance as a result of uniformly mixing the raw stool sample with PBS. While the acoustofluidically liquefied stool sample appeared similar to the sample liquefied with a vortex mixer, some precipitation at the bottom of the vortex mixed sample was observed; this was ascribed to the presence of large debris and was confirmed with the subsequent SEM observation. We repeated our experiments using independent samples received

from the same volunteer at different days, and we observed repeatable performance between our acoustofluidic device and the standard procedure. Moreover, the variation in consistency of stool samples at different days exhibits the capability of our device to liquefy stool samples over a range of consistencies; when measured by a rotary viscometer (NDJ-5S, well join, Amazon, USA), the viscosities of the diluted stool samples was found to range from 32 ± 15 mPa.s to 95 ± 21 mPa.s, corresponding to the viscosities of stool samples from 1618 ± 328 mPa.s to 7285 ± 1008 mPa.s. When comparing the consistency of stool samples, the amount of debris is a good indicator for the thickness of the sample. The presence of additional debris indicates a thicker sample that is more difficult to liquefy. Additionally, parameters such as dilution ratio, acoustic intensity, and frequency can be tuned to further accommodate the variation in stool sample.

2.3.3. Morphology Characterization

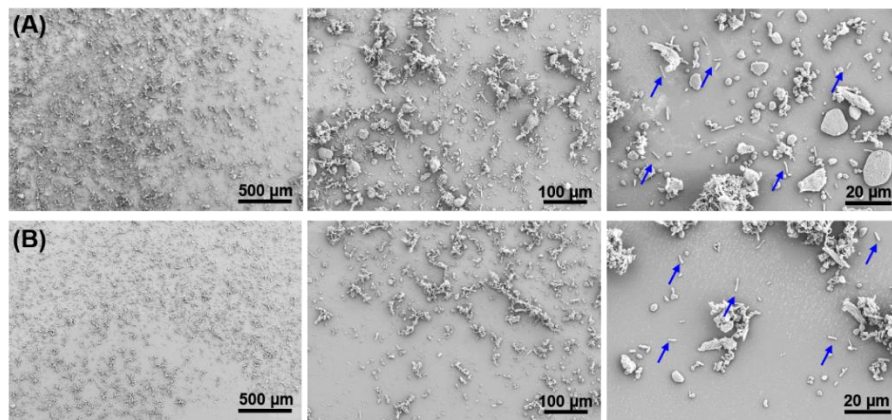


Figure 2.7: SEM characterization of liquefied human stool samples. These samples are prepared using (A) a standard method and (B) our acoustofluidic device. The blue arrows represent rod-shape bacteria.

Next, we used SEM images to examine the morphology of liquefied stool samples and assess the liquefaction performance of our acoustofluidic device. Figure 2.7 shows the SEM images of liquefied stool samples at different magnifications. At low magnification (left in Figure 2.7), we can see that sample liquefied using a vortex mixer contained many large abiotic impurities; however, samples liquefied with our acoustofluidic device appear to contain overall smaller constituents. This difference can be further clarified by images at high magnification (middle in Figure 2.7), where numerous debris in samples liquefied by the standard method is as large as 80 μm but only 40 μm in samples prepared with the acoustofluidic platform. At the highest magnification (right in Figure 2.7), bacterial cells, which would be analyzed in subsequent analysis, can be found in both samples. It is also encouraging that the rod-shape of the bacteria has been preserved in both methods, revealing negligible detrimental effects of acoustic streaming on bacteria integrity.

2.3.4. Bacterial Cell Culture

Stool culture is one of the most definitive methods for pathogenic bacteria detection in human stool samples, which depends on bacterial cells' ability to proliferate. Here, cultures of stool samples liquefied by both methods were investigated to compare the influence of liquefaction methods on bacterial proliferation. Considering that *E. coli* is the most abundant bacteria in a stool sample, the selective culture media, EMB agar, was employed. In Figure 2.8, only a slight puncture is observed in the control group (PBS only)

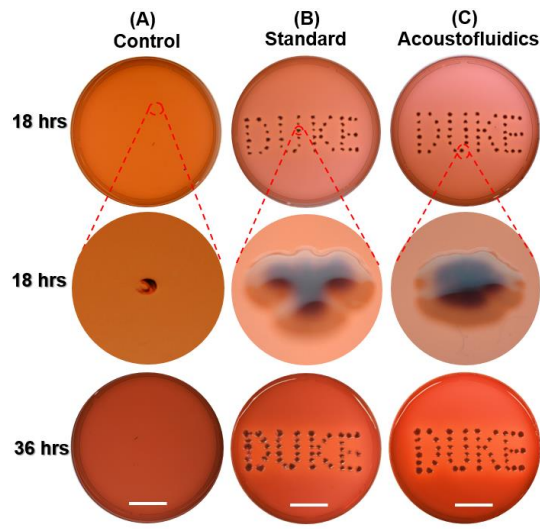


Figure 2.8: Photos of bacterial cell culture. The results show bacterial cells inoculated on EMB agar in 100x20 mm culture dishes at different incubation times for (A) negative control group (PBS only, without any stool sample), (B) liquefied stool sample prepared using the standard method, and (C) liquefied stool sample processed by our acoustofluidic device. Scale bar: 2.5 cm.

, while dark core-white shell colonies appear in both liquefied stool samples, suggesting a sterile condition. The whitish shell stems from growth of gram-negative bacteria incapable of fermenting lactose; and the dark core originates from the propagation of gram-negative bacteria capable of fermenting lactose, which creates an acidic environment and promotes the conjugation of eosin and methylene blue (Figures 2.8B&C at 18 hrs). Increasing the incubation time from 18 hrs to 36 hrs, these colonies have expanded in both liquefied samples, demonstrating favorable bacterial propagation ability in both methods (Figures. 2.8B&C). We did, however, note that the green metallic sheen, one of the important characteristics of *E. coli* culture, was not observed. This phenomenon is presumably due to the co-culture of interfering whitish bacteria due to

direct inoculation of stool samples on EMB. Similar lack of green metallic sheen has been reported for culture of milk samples⁹⁵ and culture of *E. coli* with interference of whitish colonies.⁹⁶ Overall, these results indicate that our acoustofluidic device is comparable with the standard method in maintaining bacterial cells' proliferation ability.

2.3.5. Fluorescence Microscope

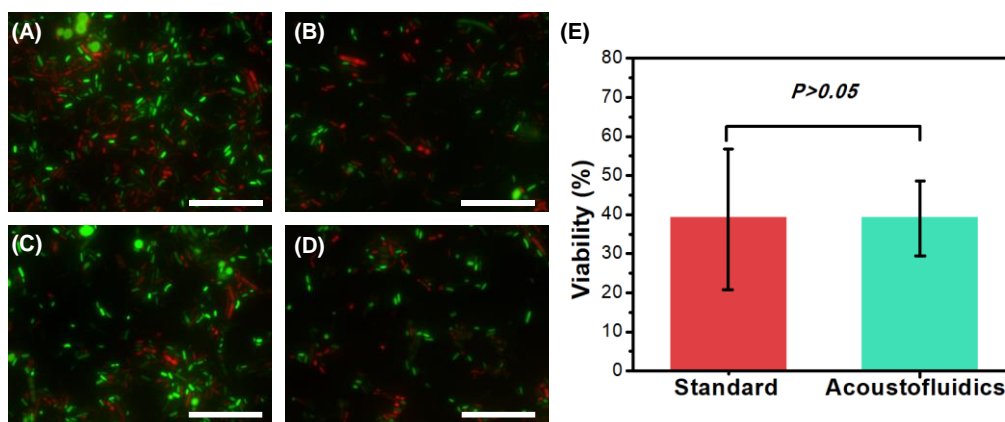


Figure 2.9: Different fluorescence microscope images (100 x) of Live/Dead BacLight stained liquefied stool samples prepared using: (A)-(B) a standard stool-liquefaction procedure; (C)-(D) our acoustofluidic stool liquefier. Green fluorescence represents live bacteria while red fluorescence refers to dead bacteria. (E) Comparison of bacterial cell viability for the two liquefaction methods. For each method, four independent experiments were conducted, and over 2800 bacterial cells were counted. $P > 0.05$ (ANOVA) represents that no significant difference between the two groups is observed. Scale bar: 50 μm .

Certain downstream applications of stool samples require intact live bacteria, such as flow cytometry,^{78, 79} bacteria detection^{71, 80} and culture,⁷⁷ and therefore microscope analysis was performed to assess bacteria viability. As shown in Figures. 2.9A-D, both live (green) and dead (red) bacterial cells can be found in liquefied stool samples prepared with either method. To measure the bacteria viability, a Matlab code was written to count

the number of live and dead bacterial cells. In total, over 2800 bacterial cells were considered for each method. According to Table S1, the viabilities were estimated, which are $39.2\pm 17.5\%$ and $39.1\pm 10.6\%$ for stool samples liquefied by standard method and our acoustofluidic liquefier, respectively (Table 1). With a P value >0.05 in statistics, our acoustofluidic liquefier presents similar capability as the standard method to preserve bacterial cells' viability.

Table 1: The number of live/dead bacteria in the stool sample on different days. Results were calculated using a fluorescence microscope image and a Matlab counting program.

Methods	Green	Red	Viability	Average
	154	632	19.3%	
Standard	519	478	52.0%	$39.2\pm 17.5\%$
	488	560	46.5%	
	769	780	49.6%	
Acoustofluidics	207	524	28.3%	$39.1\pm 10.6\%$
	581	883	39.6%	

2.3.6. Flow Cytometry

Flow cytometry, an important analysis method for human stool samples,⁹⁷ was also utilized to quantitatively characterize the liquefied stool samples. Bacterial cells in liquefied stool samples were stained with live/dead bacterial counting BacLight kit. Cultured *E. coli* cells were first analyzed for setting the measurement condition of flow

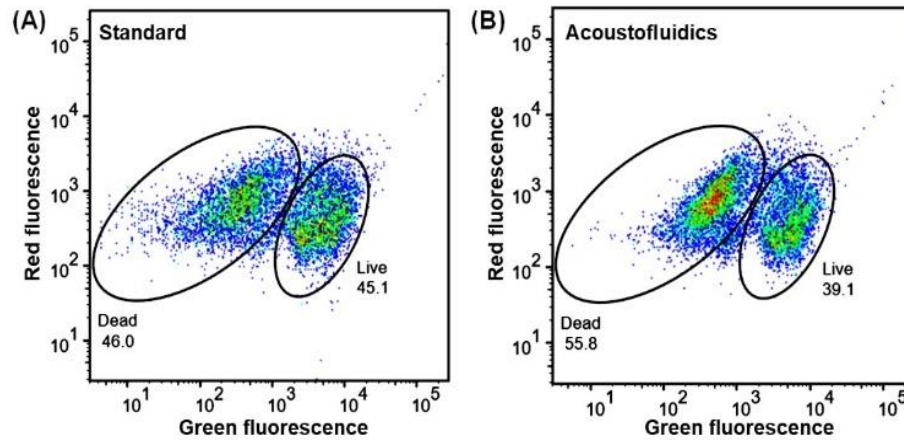


Figure 2.10: Flow cytometry for liquefied stool samples. Green fluorescence (SYTO 9) and red fluorescence (PI) plot of the bacterial cells from liquefied stool samples prepared by (A) a standard stool-liquefaction process and (B) our acoustofluidic stool liquefier. SYTO 9, a membrane permeable stain, is employed to identify live bacterial cells while PI, a membrane impermeable stain, is used to identify dead bacterial cells. The percentage of live bacterial cells was 39.1 % and 45.1 % for (A) and (B), respectively.

cytometry. First, a clear separation and strong correlation coefficient has been demonstrated between live and dead bacteria samples ($y=0.98x-1.92$, $R^2=0.997$), indicating an optimal measurement condition. Using these control settings, the bacteria viability in liquefied stool samples was investigated. In both plots of Figure 2.10, two different clusters, referring to live/dead bacterial cells, can be distinguished, but the distinction between groups is not as clear as cultured *E. coli*. This could be attributed to the complex bacterial constituents in stool samples. Another reason might be due to the presence of bacteria cells at an intermediate state of life/death. In this case, different intracellular stain ratios of SYTO 9 and propidium iodide (PI) occur and therefore some bacterial cells are located in the region between two clusters.⁹⁸ The percentage of live bacterial cells were 45.1 and 39.1%, for samples produced by the standard procedure and our acoustofluidic

device, respectively. This value is consistent with the value obtained from our fluorescence microscope analysis. All the above experiments reveal the biocompatibility and liquefaction capability of our acoustofluidic device for stool samples.

2.4. Conclusions

We have demonstrated an on-chip stool liquefaction, for the first time, using an acoustofluidic device. With a simple fabrication and operation, stool samples can be homogenized at a throughput of 30 $\mu\text{L}/\text{min}$ via strong acoustic streaming created by oscillated sharp-edge structures in the acoustofluidic device. Different characterizations show that our acoustofluidic device can not only liquefy stool samples but also preserve the viability, integrity, and proliferation ability of bacterial cells. Moreover, stool samples with different consistencies can be liquefied; this is extremely useful in clinical diagnostics due to large variations in the consistency of stool samples. Additionally, our device's ability to operate in a continuous manner could provide stool analytes for downstream applications at a consistent pace. With its unique characteristics of robustness, biocompatibility, tunability, automation, and a small footprint, our acoustofluidic stool liquefier is a promising candidate for on-chip stool liquefaction and can be potentially combined with downstream on-chip stool analysis units, expediting the development of POC stool processing and analysis platforms.

3. Size- and Structure-Controlled Synthesis of Polymeric Nanoparticles via Acoustofluidics

Size- and structured-controlled synthesis of polymeric nanoparticles, which can be preferentially delivered to tumors, shows great promise in drug delivery. Although a number of microfluidic approaches have attained reproducible nanoparticle synthesis, it is still challenging to fabricate nanoparticles in a size and structure-controlled manner. In this work, an acoustofluidic platform is developed to achieves important features for polymeric nanoparticle synthesis that are difficulties to be realized in hydrodynamic flow focusing method: (1) ultrafast mixing for size-tunable PLGA-PEG nanoparticle synthesis from both low-molecular-weight and high-molecular-weight polymers, (2) three reagents mixing for chitosan nanoparticles synthesis, and (3) sequential nanoprecipitation for PLGA-lipid core-shell nanoparticle synthesis. The developed platform expands microfluidic potential in nanomaterial synthesis, where high-molecular-weight polymers, multiple reagents, or sequential nanoprecipitations are needed.

3.1. Motivation

Polymeric nanoparticles are capable of encapsulating and delivering thousands of therapeutic molecules per particle for nanomedicine.⁹⁹ Among different nanoparticles, nanoparticle size plays a significant role in optimal organ and cellular uptake; high-molecular-weight polymeric nanoparticles can increase drug loading, prolong circulation half-life, and extend the drug release profile;^{4,7-12} core-shell hybrid nanoparticles such as PLGA-lipid are able to combine the desired properties of polymeric nanoparticles and liposomes such as high

drug loading and high serum stability; chitosan nanoparticles can be used for hydrophilic polynucleotides delivery. Using bulk synthesis methods, both low-molecular-weight and high-molecular-weight poly (lactic-co-glycolic acid) (PLGA) nanoparticles (>45 kDa) have been utilized largely in both research and biological applications.^{3,10-12} Multi-step and multi-fluid bulk synthesis methods also allow the design of novel multifunctional nanomedical systems.^{13,14} However, these bulk methods suffer from batch-to-batch inconsistencies and polydisperse outcomes.^{100,101}

Benefiting from microscale fluid environments, microfluidic platforms provide a promising alternative for reproducible polymeric nanoparticle synthesis.¹⁰²⁻¹¹¹ To date, microfluidic methods have demonstrated tremendous success in high-throughput synthesis of budesonide nanoparticles²⁷ and reproducible nanoparticle synthesis from various amphiphilic polymer systems, including poly (lactic-co-glycolic acid)-b-poly (ethylene glycol) (PLGA-PEG),^{28,29} lipid vesicles,^{30,31} and chitosan.³²

Despite the above-mentioned achievements, microfluidic methods still have several deficiencies in synthesizing polymeric nanoparticles. First, relying on diffusion between laminar flow boundary, HFF method depends strongly on fluid flow rate and are unable to mix multiple reagents.⁵ Second, high molecular weight polymers tend to aggregate within microchannels and thus the corresponding nanoparticles are difficult to fabricate through microfluidics.⁷ As a result, current microfluidic methods tend to mainly focus on synthesizing nanoparticles from low-molecular-weight polymers in single step mixing.^{28,29,32} Taking the

most widely utilized 2D HFF method as an example, high-molecular-weight polymers are concentrated along boundary interfaces and lead to channel fouling.^{7, 112} Although 3D HFF microfluidic devices were specifically designed to address high-molecular-weight polymer aggregation, these devices require precise control of the 3D fluid flow profile.^{7, 99} Third, difficulties remain in generating structured nanoparticles, such as two-layer or even three-layer nanoparticles. For 2D HFF, the sidewall sheath fluids impede it from the capability to sequentially assemble hierarchical nanoparticles.^{28,30} Usually, multiple microfluidic devices are applied. By employing two separate HFF and Tesla microfluidic devices, researchers realized sequential polymer assembly, but the intermediate procedures complicate fabrication and increase uncertainty.¹¹³ Therefore, developing new microfluidic methods to generate nanoparticles in a size and structure controlled manner from both low-molecular-weight and high-molecular-weight polymers is necessary.

In this work, we present a 2D acoustofluidic (*i.e.*, the fusion of acoustics and microfluidics)¹¹⁴⁻¹²² platform for the synthesis of chitosan nanoparticles and PLGA based nanoparticles with controlled size and structure, while eliminating polymer aggregation. Different from hydrophilic glass microchannels,¹²³⁻¹²⁵ our method exploits complete and ultrafast micromixing to realize nanoparticle synthesis in multi-fluid and multi-step way, and address polymer aggregation within the entire microchannel. By oscillating microscale sharp-edges with acoustic waves, our devices generate micro-vortex streaming to completely mix reagents in the entire microchannel.^{20, 29, 126} Using the fine-tuned devices achieved in Chapter 2,

we synthesized homogeneous PLGA-PEG nanoparticles with a tunable size from 55-120 nm from low-molecular-weight polymers; homogeneous PLGA-PEG nanoparticles with a tunable size from 75-255 nm from high-molecular-weight polymers. These uniform nanoparticles with a wide size range are difficult to fabricate by existing microfluidic methods or bulk methods.⁴ Additionally, our devices synthesized core-shell PLGA-PEG/lipid core-shell nanoparticles, providing a new method for sequential nanoprecipitation in a single device. Furthermore, we synthesized uniform chitosan nanoparticles by mixing three different reagents. With its 2D structure, and complete, sequential, rapid (<10 ms) micromixing, our acoustofluidic synthesis platform can harness the benefits of microfluidics in a wider variety of scenarios, such as synthesis of high-molecular-weight polymers, multiple reagents, and sequential nanoprecipitation.

3.2. *Materials and Methods*

3.2.1. Chemicals

PLGA-PEG-COOH with molecular weights of 10, 20, 40 and 50 kDa for PLGA and 5 kDa for PEG were purchased from PolySciTech (Akina Inc., West Lafayette, IN, USA). PLGA-PEG (70K-2K) and PLGA (5K-10K) were also purchased from PolySciTech (Akina Inc., West Lafayette, IN, USA). PLGA-PEG-COOH with molecular weights of 10 kDa for PLGA and 1 and 3 kDa for PEG were purchased from Nanosoft Polymers (Winston-Salem, NC, USA). PLGA-PEG (90K-10K) was purchased from Creative PEGWorks (DLG-10k90k31, NC, USA). 1,2-dipalmitoyl-sn-glycero-3-phosphocholine (DPPC, ~733 Da,

850355) and phosphoethanolamine-N-[methoxy (polyethylene glycol)-2000 (DSPE-PEG2000, ~2780 Da, 880135) were purchased from Avanti Poplar Lipids (Alabaster, AL). Low-molecular weight chitosan, adenosine triphosphate (ATP), cholesterol (C8667, ~386 Da), and purified water (W4502) were purchased from Sigma-Aldrich (MO, USA). Ethanol was purchased from VWR, USA. Phosphate-buffered saline (PBS) was purchased from Life Technologies (2046802, 10X, USA). Acetonitrile was purchased from Grainger (26WD84, NC, USA).

3.2.2. Device Fabrication

In this study, a piezoelectric element with a resonant frequency of 2.0 kHz was used as acoustic transducer (AB2720B-LW100-R. PUI Audio Inc., OH, USA). To fabricate the microchannel with sidewall sharp-edges, a SU8 mold was first prepared by standard photolithography and deep reactive ion etching. Then, the mixture of PDMS base and curing agent at a ratio of 10:1 (Sylgard 184, Dow Corning, MI, USA) was degassed and poured on the SU8 mold. Once cured at 65 °C for 1 h, the PDMS microchannel was peeled and bonded on a cover glass by oxygen plasma treatment. After that, the stack of the cover glass and the PDMS microchannel was baked at 65 °C for 12 h. Finally, an acoustic transducer was bonded on the same covers glass adjacent to PDMS channel using epoxy (PermaPoxy™ 5 Minute General Purpose, Permatex).

3.2.3. Nanoparticle Synthesis from Low-Molecular-Weight Polymers

PLGA-PEG precursor solutions were prepared by dissolving PLGA-PEG of different molecular weights in acetonitrile at three concentrations (5, 10, and 20 mg/mL). Unless otherwise indicated, the 10 mg/mL PLGA_{10K}-PEG_{5K} solution was used in most of the experiments. In the case of acoustofluidic synthesis, the two solutions were injected into the device through two separate inlets at varying flow rates. Unless otherwise stated, PLGA-PEG solution and water were injected both at the flow rate of 10 μ L/min. In the case of bulk synthesis, 50 μ L of PLGA-PEG in acetonitrile was mixed with 50 μ L of purified water on a vortex mixer for 1 minute.

3.2.4. Nanoparticle Synthesis from High-Molecular-Weight Polymers

For PLGA-PEG nanoparticle synthesis, three 1.0 mL syringes for polymer precursor solution and water were co-injected into the microchannel. The flow ratio for polymer and water was maintained at 1:10, unless otherwise indicated. The frequency for acoustofluidic device was set to approximately 4.0 kHz and the input voltage was 38 V_{PP}. To synthesize nanoparticles by 2D HFF, we fabricated microchannels with the identical geometry as the acoustofluidic device, except for the absence of sharp-edges. The flow rates of the polymer stream and the two water sheath streams were maintained at 1 μ L/min and 50 μ L/min, respectively, keeping a flow ratio of 1:100 for polymer stream to aqueous stream. For the synthesis of nanoparticles by bulk methods, 10 μ L of polymer

solution were mixed with 100 μ L water solution using a vortex mixer (MX-S, Scilogex, USA) for 1 min.

3.2.5. PLGA-PEG/Lipid Core-Shell Nanoparticle Synthesis

For PLGA-PEG/lipid core-shell nanoparticle synthesis, PLGA_{70K}-PEG_{2K} was dissolved in acetonitrile with a concentration of 2.5 mg/mL. The lipid solution, which composed of DPPC, DSPE-PEG2000, and cholesterol, were dissolved in ethanol at a concentration of 0.8 mg/mL, 0.8 mg/mL, and 1 mg/mL, respectively. To prevent aggregation between high-molecular-weight hydrophobic PLGA chains, polymers with a PEG chain is needed. Meanwhile, the surface areas of PLGA nanoparticles should be largely uncovered and exposed, to provide driving force for lipid-PLGA assembly by their hydrophobic attraction between the PLGA and the lipid tail.⁴⁶ Based on a previous publication,⁴⁷ a high ratio of PLGA to PEG (>10:1) can lead to partial coverage of PEG on the surface of PLGA nanoparticles. Thus, an ultra-high ratio of PLGA to PEG ratio (35:1) was chosen. The synthesis of core-shell nanoparticles included two stages with three inlets and one outlet. First, the solution of PLGA-PEG and water were separately injected into inlets and mixed to generate PLGA-PEG core. Second, lipid solution was injected in one middle inlet for self-assembly of lipid shell on the polymer core. The operation voltage was 45 V_{PP} and the flow rate of water was 20 μ L/min. For liposome and PLGA_{70K}-PEG_{2K} nanoparticle synthesis, the flow rates were both 3 μ L/min. For PLGA-PEG/lipid nanoparticle synthesis, the flow rate of PLGA-PEG solution was kept at 3 μ L/min, while

that of lipid solution increased from 1 $\mu\text{L}/\text{min}$ to 7 $\mu\text{L}/\text{min}$. For the nanoparticles stability studies in PBS and water, 25 μL of 10X PBS is pipetted into 50 μL PLGA_{70K}-PEG_{2K} solution or PLGA_{70K}-PEG_{2K}/lipid synthesized at a lipid flow rate of 1 $\mu\text{L}/\text{min}$, while three consecutive additions of 25 μL of 10X PBS were added into 50 μL PLGA_{70K}-PEG_{2K}/lipid and liposome solution, respectively.

3.2.6. Synthesis of Chitosan Nanoparticles

In this work, chitosan NPs were synthesized by mixing chitosan, purified water, and ATP solutions together at different flow rate ratios. The water phase served to prevent the chitosan solution from reacting with the ATP solution before synthesis. Once activated, our device mixed the three solutions together and thus produced chitosan NPs. To prepare the chitosan solution, we first conducted chitosan purification following the procedures reported elsewhere.¹¹² The purified chitosan was dissolved in acetic acid solutions to obtain chitosan solutions of two different concentrations, 1 and 0.5 mg/mL. The ATP solution was prepared by dissolving ATP in ultra-purified water at two different concentrations, 1 and 0.5 mg/mL. It is important to note that for chitosan NPs synthesis, pH values for both chitosan and ATP solutions are critical to whether ATP-initiated ionic gelation can occur and thus, produce chitosan NPs. As a result, in this work both of them were carefully adjusted to have a pH value of ~ 4 , which was reported as a suitable value for the synthesis of chitosan/ATP NPs.¹¹² For TEM imaging, TEM samples were prepared by dispensing a drop of the sample solution containing the synthesized chitosan NPs on

a 300-mesh carbon-coated copper grid for 30 minutes at room temperature. After the chitosan NPs were adsorbed on the grid, they were negatively stained with sterile-filtered uranyl-acetate aqueous solution and incubated for 5 minutes. The grid was finally washed twice with distilled water and dried at room temperature before imaging.

3.2.7. Sample Characterization

For sample characterization, the average size and size distribution were measured with the Malvern Zetasizer (Malvern Instruments, UK). For each measurement, 50 μL of the sample was pipetted in a Malvern cuvette (NC0628994, Fischer Scientific, USA). At least three measurements were conducted for each sample. For TEM imaging, 10 μL of the synthesized nanoparticle suspension was placed on a 300-mesh copper grid (CF300-Cu, Electron Microscopy Sciences, USA). After 10 min of incubation, a parafilm sheet was used to adsorb the excessive nanoparticle solution. Then, the grid was negatively stained with uranyl-acetate solution for 15 min. Finally, the grid was washed twice using distilled water and dried at room temperature. The morphology of the sample was then observed using a Tecanai G2 Twin TEM (FEI, USA).

3.3. Results and Discussion

3.3.1. Principle of the Acoustofluidic Synthesis Platform

Figure 3.1A shows the schematic design of the acoustofluidic synthesis platform. A PDMS microchannel with sidewall sharp-edges and an acoustic transducer are bonded adjacently on a cover glass.¹²⁷ When a driving voltage is applied, vibration from the

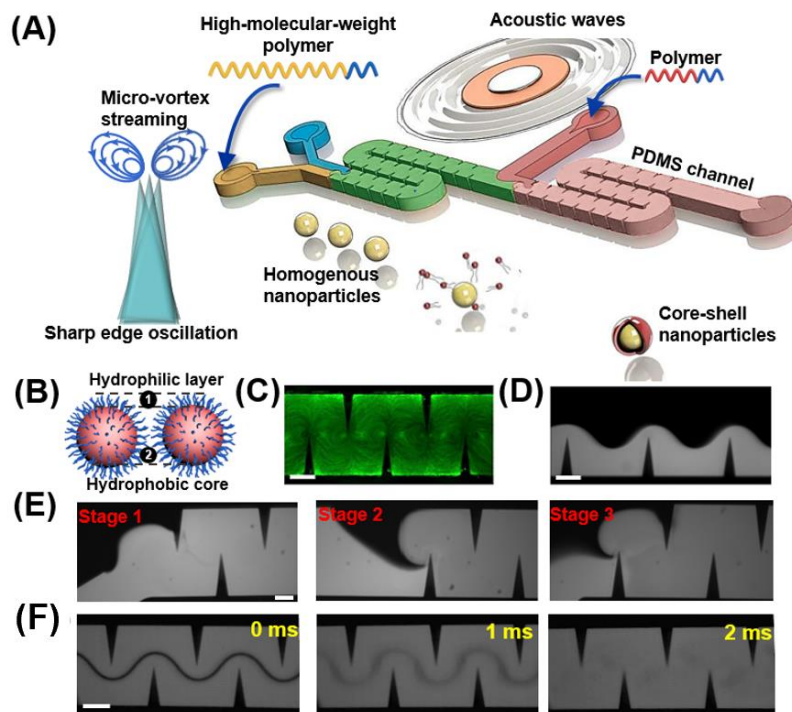


Figure 3.1: Design and working principle of the acoustofluidic synthesis platform for core-shell nanoparticle synthesis. (A) Schematic of high molecular weight polymeric nanoparticle/lipid core-shell synthesis using micro-vortex streaming. (B) Illustrative figure of the synthesized nanoparticle component layers, where the hydrophilic layer is used to prevent aggregation between high molecular weight hydrophobic polymer chains. (C) Stacked image of 10 pictures over 100 ms for 1.9 μm fluorescent beads trajectories showing the acoustic micro-vortex streaming. Scale bar: 200 μm . (D) With acoustics off, a laminar flow is observed in the microchannel. Scale bar: 200 μm . (E) With acoustics on, three-step sequential micromixing is achieved in a single device. In each step, different fluids are completely mixed at the tip of the first sharp edge structure they encountered. (F) characterization for the mixing time of water and PLGA_{50K}-PEG_{5K} at 30 mg/mL. Scale bar: 200 μm .

acoustic transducer oscillates sharp-edges within a microchannel. For amphiphilic polymers, this oscillation generates acoustic micro-vortex streaming to mix amphiphilic polymer solution and its anti-solvents (Figure 3.1A).^{128, 129} The amphiphilic polymers then self-assemble into nanoparticles. During this process, the hydrophobic polymer chains are

excluded from surrounding hydrophilic water molecules and arrange into hydrophobic cores, while the hydrophilic chains extend into water molecules and function as a steric hindrance layer to prevent aggregation between the hydrophobic cores¹³⁰⁻¹³² (Figure 3.1B).

The first feature of our device is to synthesize nanoparticles from both low-molecular-weight and high-molecular weight polymers. Specially, to prevent high-molecular-weight polymer aggregation within a microchannel, the acoustofluidic devices exploit complete, rapid micromixing to achieve successful polymer self-assembly and preserve the hydrophilic shell and hydrophobic core structure in Figure 3.1B. In 2D HFF, precipitated polymers are highly concentrated into a small interfacial region and numerous polymers entangle with each other, resulting in polymer aggregation.^{7,112} Using our micro-vortex streaming based devices (Figure 3.1C), the solvent exchange of polymer solution and its anti-solvent is completed within an entire microchannel (Figures 3.1D and E). This complete mixing disperses precipitated polymers uniformly within an entire microchannel and reduces random polymer entanglements, allowing the successful self-assembly of high-molecular-weight polymers. In terms of mixing time, bulk methods suffer from polydispersity due to slow mixing.¹⁰⁻¹² This slow mixing creates a non-uniform reaction environment and a temporally lengthy self-assembly process, leading to inhomogeneous nanoparticles larger than 200 nm.⁴ Instead, our acoustofluidic devices completely mix laminar fluids at the tip of the first sharp-edge they encounter, when acoustics switch from off to on (Figures 3.1D and E). This rapid, complete micromixing

provides a uniform reaction condition for monodisperse synthesis of high-molecular-weight polymeric nanoparticles, and then the hydrophilic surface layer on synthesized nanoparticles prevents aggregation via steric hindrance effect.

Another important feature of this acoustofluidic device is its ability to perform sequential nanoprecipitation. Considering that each micro-vortex streaming can serve as a mixing site, multiple-step (≥ 2) nanoprecipitation can be achieved conveniently by introducing middle inlets into microchannels (Figure 3.1E). This unique feature is critical for the future design of novel therapeutic compounding nanosystems, such as three-layer multifunctional nanoparticles from the combination of lipid/stimuli responsive peptide^{53,54} and PLGA/lipid nanoparticles^{13,14}.

For the third feature of ultrafast micromixing for multiple reagents reaction, the mixing time was characterized using fast camera microscope, as shown in Fig. 1F. Three fluids including water, 30 mg/mL PLGA_{50K}-PEG_{5K}, and water were injected at a flow rate of 25, 5, and 25 $\mu\text{L}/\text{min}$, respectively. The mixing time is observed to be less than 3 ms, indicating an ultrafast, complete mixing.

With the ability to exclude polymer aggregation, mix multiple reagents and realize sequential mixing, our acoustofluidic synthesis devices provide a pragmatic platform for synthesizing size- and structure-controllable nanoparticles from both low-molecular-weight and high-molecular-weight polymers, while maintaining the uniform reaction environment of microfluidics.

3.3.2. Controllable Synthesis of Low-Molecular-Weight Nanoparticles

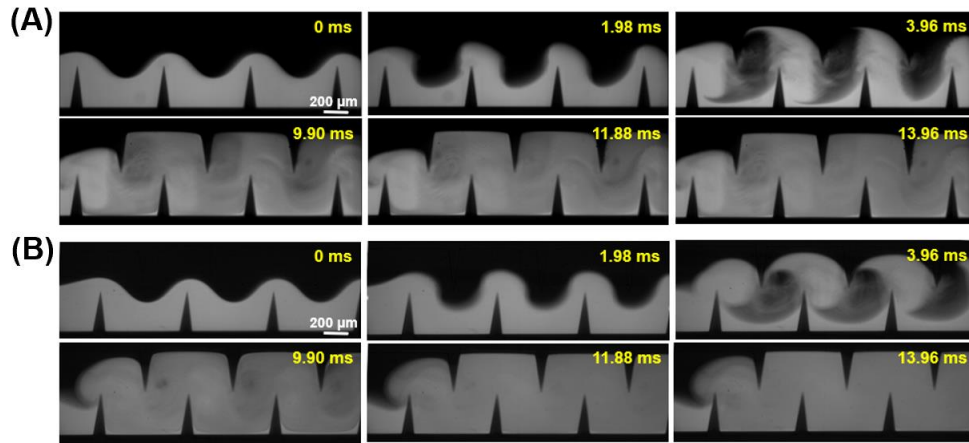


Figure 3.2: The mixing process of DI water and fluorescence dye under 50 V_{PP} characterized using a fast camera (Photron, 500K-M1) at different total flow rates. The total flow rates are (A) 150 $\mu\text{L}/\text{min}$ and (B) 90 $\mu\text{L}/\text{min}$, respectively. The flow rate ratio of DI water and fluorescence dye is maintained at 1.

Undoubtedly, the ultimate homogeneity and reproducibility of nanoparticles depend on the performance of the acoustofluidic synthesis device, that is, the mixing time. Therefore, we first characterized the mixing time of two reagents reaction. In Figure 3.2, the device was operated at a total flow rate of 90 $\mu\text{L}/\text{min}$ at 35 V_{PP} and 150 $\mu\text{L}/\text{min}$ at 50 V_{PP} , respectively. The average mixing time τ was also estimated by the following equation.¹³³

$$\tau = d_{mix} / V_{avg} \quad (3.1)$$

where, d_{mix} is the distance from unmixed to totally mixed regions, and V_{avg} is the average fluid velocity. At 150 $\mu\text{L}/\text{min}$, τ was calculated to less than 12 ms, being consistent with the experimental value of 11.88 ms (Figure 3.2A). At 90 $\mu\text{L}/\text{min}$, τ exhibited a calculated and experimental value of approximate 8.07 ms and less than 9.9 ms, respectively (Figure

3.2B). In previous microfluidic-based synthesis methods, τ was 189 ms in surface acoustic waves-based device,⁶⁰ 400 ms in 2D HFF device,³² 7-53 ms for turbulent jet platform,⁶¹ and 4-25 ms in star-based acoustic micromixer.²⁷ These results indicate that our acoustofluidic device can provide efficient and ultrafast reagent mixing for polymeric nanoparticle synthesis.

We then investigated the performance of synthesized nanoparticles on driving voltages. By altering the driving voltage and mixing performance, we synthesized PLGA-PEG NPs with our acoustofluidic device. With the numerical model we previously developed,¹⁷ we first predict the concentration distribution of solutions (*i.e.*, the mixing performance) under different vibration amplitudes of the sharp-edge structures (Figure 3.3A); as the vibration amplitude is increased from A_0 to A_3 , enhanced acoustic streaming improves the mixing performance. Improved mixing performance due to increased driving voltages is also confirmed in experiments (Figure 3.3B), where complete mixing is achieved after the first pair of sharp-edge structures when the device is activated with 30 V_{PP}. Dynamic light scattering analysis shows that as the driving voltage increases from 0 to 30 V_{PP}, the size distribution narrows and the NPs size decreases strikingly from ~17070 to 707 nm down to 65 nm (Figure 3.3C). When the acoustofluidic mixing is off (0 V_{PP}), NPs can still be formulated relying solely on the slow, diffusion-based mixing occurring in the interface of the water and polymer solution, with an average size of 168.3 ± 1.5 nm (polydispersity index = 0.22 ± 0.02). The diffusion-based mixing achieves complete solvent exchange on a

time scale longer than that for polymer aggregation; as such, the polymers nucleate less nanoparticle seeds and tend to aggregate on those seeds, eventually forming larger NPs.⁵ Activating our device at 10 V_{PP} alone can lead to a significant decrease in the NPs size by 33% to 112.7 ± 0.7 nm (polydispersity index = 0.19 ± 0.02). Increasing the driving voltage to 20 V_{PP} further reduces the NPs size to 78.4 ± 0.5 nm (polydispersity index = 0.16 ± 0.01). When driven at 30 V_{PP} , our device produces PLGA-PEG NPs as small as 64.7 ± 0.5 nm with an average polydispersity index of 0.13 ± 0.01 (Figure 3.3D). The reduces in size and

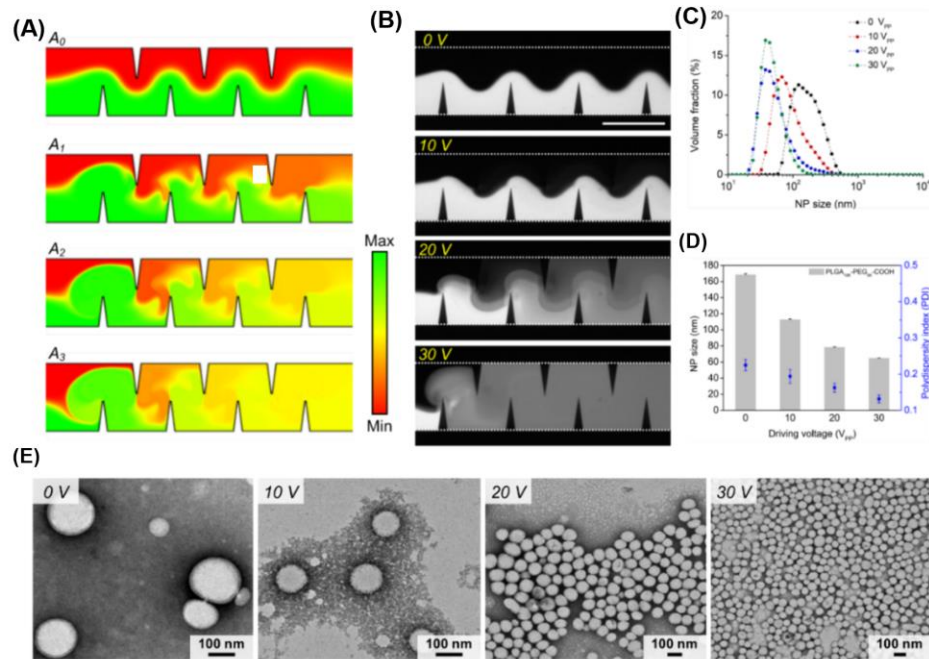


Figure 3.3: Effect of the mixing performance of the acoustofluidic device on the size of PLGA-PEG NPs. (A) Simulation results and (B) experimental results showing the concentration distribution, *i.e.*, the mixing performance, under different driving voltages. (C) Size distribution, (D) average size, and (E) TEM images of NPs synthesized by our acoustofluidic device under different driving voltages. As the driving voltage increases, the size distribution becomes narrower and the NPs size is reduced markedly. Experiments are conducted using 10 mg/mL PLGA_{10K}-PEG_{5K} under the driving frequency of 4.0 kHz and the flow rate of 10 μ L/min for both water and PLGA-PEG solution.

driving voltages are expected and can be attributed to the rapid solvent exchange facilitated by enhanced acoustic streaming. The size and uniformity of the NPs produced under different driving voltages are also confirmed by TEM examination (Figure 3.3E). These results show that our acoustofluidic method can reproducibly yield PLGA-PEG NPs with a size variation of ± 1 nm and a variation of ± 0.02 in polydispersity index among independent experiments, when using the same batch of PLGA-PEG precursor.

As a comparison to our acoustofluidic device, we synthesize PLGA-PEG nanoparticles using vortex mixing. The PLGA-PEG nanoparticles prepared by our acoustofluidic platform feature narrower size distributions than those prepared by vortex mixing, with the size-distribution curves nearly overlapping (Figure 3.4A). Our acoustofluidic device produces NPs with an average size of 64.7 ± 0.7 nm, which is $\sim 39\%$ smaller than those prepared by vortex mixing (106.3 ± 15.2 nm) (Figure 3.4B). TEM images confirm that our acoustofluidic device generates smaller NPs of uniform size, and that vortex mixing prepares larger NPs with a broader range of sizes (Figures 3.4C and D). Quantitatively analyzing the TEM images, we further verify that the size of the NPs prepared by the acoustofluidic device falls into a narrow size range with most of the NPs being around 50~70 nm (Figure 3.4E), while vortex mixing yields NPs with sizes ranging widely from 10 to 120 nm (Figure 3.4F). These results demonstrate that our acoustofluidic method can generate nanoparticles with smaller size and better uniformity.

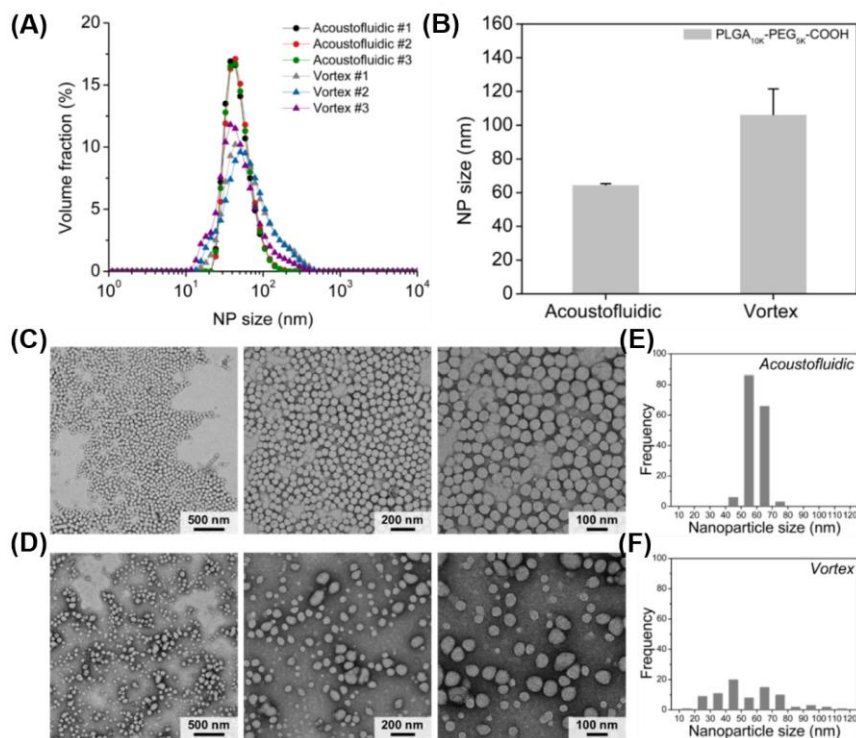


Figure 3.4: Comparison of PLGA-PEG NPs synthesized by vortex mixing and acoustofluidic mixing. (A) Size distribution and (B) average size of PLGA-PEG NPs synthesized by the two different methods. TEM images of PLGA-PEG NPs prepared by (C) acoustofluidic device and (D) vortex mixing. Histograms showing the size distribution of the PLGA-PEG NPs synthesized by (E) acoustofluidic device and (F) vortex mixing.

To further highlight the robustness of our synthesis method, we compare the size of nanoparticles produced by acoustofluidic device ($20 V_{PP}$) to those prepared by diffusion-based mixing ($0 V_{PP}$; OFF) and vortex mixing, using PLGA-PEG precursors with various molecular weights (MWs) (10K-1K, 10K-3K, 10K-5K, 20K-5K and 40K-5K) at different precursor concentrations (5, 10, and 20 mg/mL). The diffusion-based mixing is the scenario where the same synthesis device is used but not acoustically scenario where the same synthesis device is used but not acoustically activated, removing the acoustic streaming and leaving only diffusion to mix reagents. As the precursor concentration

increases, there is an overall increase in size for all the molecular weights tested, irrespective of the synthesis method (Figure 3.5A). For example, using the 10K-5K precursor, the acoustofluidic device yields PLGA-PEG NPs of 73.1 ± 1.58 , 83.2 ± 2.43 , and 132.6 ± 1.73 nm at the precursor concentrations of 5, 10, and 20 mg/mL, respectively. Similarly, using the 20K-5K precursor, the acoustofluidic device generates NPs of 73.3 ± 1.66 , 79.85 ± 1.33 , and 131.6 ± 3.7 nm at the precursor concentrations of 5, 10, and 20 mg/mL, respectively. Similar trends are observed for PLGA-PEG NPs prepared by the bulk mixing and diffusion-based mixing. The acoustofluidic device always produces the smallest NPs with highest reproducibility (*i.e.*, smallest size deviation) and tightest size distribution for all the molecular weights tested, regardless of the precursor concentration. These results demonstrate that our acoustofluidic device is well suited for polymer-based spherical NPs synthesis and that it allows for the reproducible synthesis of NPs using various molecular weights of a precursor at varying concentrations.

Adjusting the volumetric ratio of a polymer precursor in a bulk solution could significantly change the size of NPs synthesized. We synthesize NPs by gradually changing the flow rate of the polymer solution (from 1 through 9 $\mu\text{L}/\text{min}$), while keeping the total flow rate in the channel constant (10 $\mu\text{L}/\text{min}$). The ability to completely mix two solutions at varying flow rate ratios is first confirmed by experiments. Under the same voltage, our acoustofluidic device can completely mix PLGA-PEG precursor and water at varying flow rate ratios, thus yielding NPs with average sizes ranging from 57.27 ± 0.98

nm to 95.37 ± 0.99 nm (Figure 3.5B). The NPs size decreases as the flow rate ratio is decrease from 0.7 through 0.3, and interestingly, increases when the flow rate ratio is further decreased from 0.3 through 0.1. This trend suggests that the flow rate ratio of 0.3 may be the optimal ratio to produce the smallest NPs, and these results demonstrate that our device can control the NPs size by mixing two solutions at different flow rate ratios.

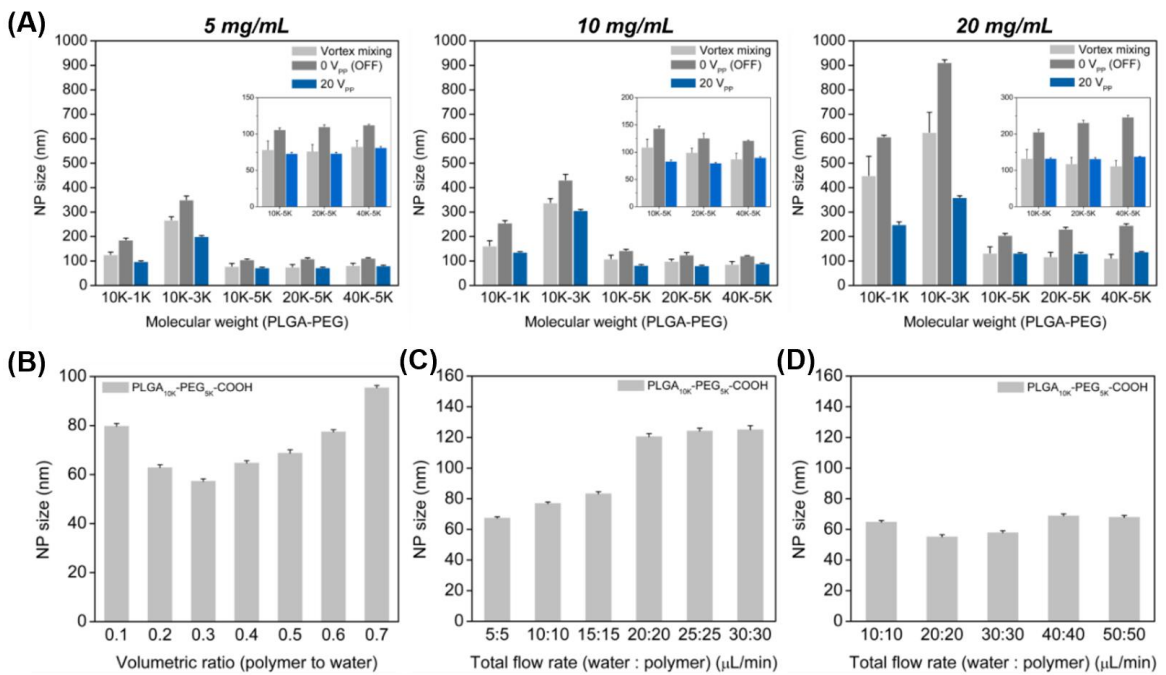


Figure 3.5: Comparison of average size of PLGA-PEG NPs synthesized with various parameters. (A) Dependence of the average size of synthesized PLGA-PEG NPs on the precursor concentration and molecular weight, when prepared using different methods: vortex mixing, diffusion-based mixing (0 V_{PP} / OFF) and acoustofluidic device (20 V_{PP} / ON). Results presented in (A) are obtained at a flow rate of 10 and 1 μL/min for water and PLGA-PEG solution, respectively. (B) Effect of the volumetric ratio of PLGA-PEG precursor in bulk solution on the NPs size. (C) Effect of the total flow rate on the NPs size under the driving voltage of 20 V_{PP}. (D) Effect of the total flow rate on the NPs size under the driving voltage of 50 V_{PP}.

To evaluate the dependence of NPs size on the total flow rate, we first synthesize NPs at different total flow rates under a low driving voltage ($20 V_{PP}$), where the flow rate ratio of PLGA-PEG precursor and water remains at one to simplify the experimental setup. As the total flow rate increases from 10 to 30 $\mu\text{L}/\text{min}$, the NPs grows from 67.3 ± 0.9 nm to 83.2 ± 1.4 nm and further raising the total flow rate from 30 to 40 $\mu\text{L}/\text{min}$ increases the NPs size by nearly 50 % to 120.5 ± 2.0 nm; increasing from 40 to 60 $\mu\text{L}/\text{min}$ leads to an increase less than 5% to 125.0 ± 2.7 nm (Figure 3.5C). As the total flow rate increases beyond a certain point (40 $\mu\text{L}/\text{min}$ in this case), the NPs size changes insignificantly and becomes independent of the total flow rate. Therefore, when synthesizing at relatively high flow rates, we must use higher driving voltages to maintain the mixing performance and therefore, the small NPs size. With a driving voltage of $50 V_{PP}$, for example, the NPs size are reduced by more than 50% both at the total flow rate of 40 and 60 $\mu\text{L}/\text{min}$; at even higher total flow rates, including 80 and 100 $\mu\text{L}/\text{min}$, the NPs size is maintained at 68.8 ± 1.3 nm and 67.9 ± 1.2 nm, respectively (Figure 3.5D). The ability to synthesize NPs at relatively high flow rates reveals the potential to use our platform for high-throughput synthesis of nanoparticles.

3.3.3. Controllable Synthesis of High-Molecular-Weight Nanoparticles

Our acoustofluidic devices' ability to perform complete and ultrafast solvent exchange can help prevent polymer aggregation. To test its effectiveness, we used the acoustofluidic devices to synthesize PLGA-PEG nanoparticles from different polymer

precursors, including those with high molecular weights and high concentrations. Currently, three major stages are believed to be involved in the synthesis of PLGA-PEG nanoparticles by nanoprecipitation.^{28,134, 135} First, after solvent exchange, hydrophobic PLGA chains precipitate from the surrounding water molecules by excluding them into certain ordered orientations, and disperse as unimers in the solvent mixture. Second, to increase the system entropy and minimize the orientations, neighboring unimers attract each other through PLGA chains and arrange into ordered oligomers (nuclei). The third stage is the diffusion-dominated addition of more unimers on nuclei. This process eventually terminates in the formation of kinetically locked PLGA-PEG nanoparticles, where the hydrophilic PEG groups on the nanoparticle surface shield their PLGA hydrophobic chains from the surrounding polar aqueous phase.¹³⁰

Based on the three stages, Figure 3.6A provides a hypothesis to illustrate the discrepancy between PLGA-PEG nanoprecipitation in 2D HFF and the acoustofluidic devices. For 2D HFF, the precipitated polymers are highly concentrated at a narrow region, thus pushing high-molecular-weight polymers close enough to each other (first stage in Figure 3.6A). Then, the chances for forming nuclei site are significantly enhanced, and many nuclei sites can be generated on one hydrophobic PLGA chain, resulting in polymer aggregates like dendrimers (second stage). Finally, these dendrimers connect to each other and lead to three-dimensional polymer aggregate network (three stage). Consequently, neighboring unimers fail to self-assemble into spherical nanoparticles, and

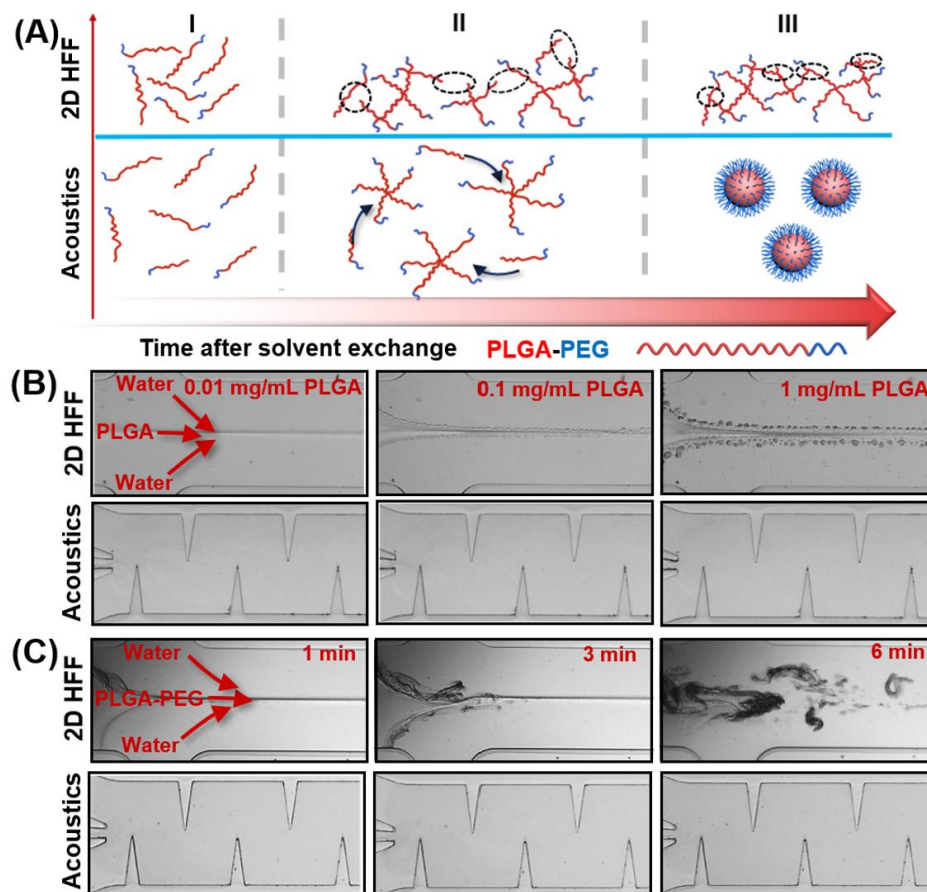


Figure 3.6: Acoustofluidic synthesis of high molecular weight polymeric nanoparticles without aggregation. (A) Schematic hypothesis illustrating the occurrence of polymer aggregation in the 2D HFF device and the absence of polymer aggregation in the acoustofluidic device. (B) The influence of polymer concentration on aggregation using the 2D HFF device from 0.01 mg/mL to 1 mg/mL PLGA (5K-10K). All microscopy images were captured at 1 min of operation. (C) Representative microchannel images showing the macroscopic nanoprecipitation evolution of PLGA50K-PEG5K at 50 mg/mL by 2D HFF and acoustofluidic devices. The microscopic images are taken at different time scale: left (1 min), middle (3 min) and right (6 min).

the hydrophilic PEG chains cannot completely shield PLGA chains from aqueous phase.

In contrast, the acoustofluidic devices uniformly disperse PLGA-PEG unimers within the entire channel, increasing the inter-distance between unimers (first stage in Figure 3.6A).

In the second stage, the dispersed unimers are able to arrange into spherical form due to its uniform dispersion and generate homogenous nuclei at the same timescale enabled by the ultrafast mixing. In the third stage, due to the homogenous dispersion of dispersed unimers and nuclei, the probability of adding unimers into nuclei is approximately equal, forming monodisperse PLGA-PEG nanoparticles. The hydrophilic PEG on the NP surface can then prevent the aggregation of nanoparticles and the adsorption of hydrophobic PLGA on PDMS microchannel walls.¹³⁰⁻¹³²

We then experimentally investigated the two fundamental mechanisms, *i.e.*, PEG chains and uniform-dispersed polymers (low polymer concentration), in preventing polymer aggregation within a 2D HFF and acoustofluidic microchannel (Figure 3.6B). For comparison, we constructed acoustofluidic devices with polymer solution flowing in the middle of the microchannel as 2D HFF devices. The mixing time (τ_{mix}) for 2D HFF is estimated by Equation 3.²⁸

$$\tau_{mix} \sim \frac{w_f^2}{4D} \approx \frac{w^2}{9D} \frac{1}{(1+R)^2} \quad (3.2)$$

Here, w_f is the width of focusing region, D is the diffusivity of solvent, w is the width of microchannel, and R is the total flow rate ratio of water to polymer. To decrease mixing time, we chose the flow rate ratio of water, polymer, and water to be 50:1:50. For $D=10^{-9}$ m²/s, $R=100$, and $w=600$ μ m, the focusing width and mixing time are calculated to be around 4 μ m and 4 ms, respectively, where the mixing time is small enough to generate homogenous nanoparticles.^{27,29} Compared to the 4 μ m synthesis width, the 600 μ m

acoustofluidic microchannel decreases polymer concentration almost 150 times. Figure 4B shows that decreasing concentration can evidently alleviate PLGA aggregation in 2D HFF device. At the same polymer flow rate of 1 $\mu\text{L}/\text{min}$ and a flow rate ratio of 10:1 at 8 V_{PP} , the acoustofluidic devices prevent polymer aggregation through concentrations ranging from 0.01 mg/mL to 1 mg/mL. For PEG chains, despite the occurrence of aggregation at 1 mg/mL PLGA (5-10K), aggregation disappears at 10 mg/mL PLGA_{10k}-PEG_{5k}. These results indicate the effectiveness of hydrophilic PEG and uniform dispersion in preventing aggregation.¹³⁰⁻¹³²

Figure 3.6C compares the macroscopic evolution of polymer aggregation within the microchannel using the acoustofluidic and 2D HFF devices for PLGA_{50k}-PEG_{5k} at 50 mg/mL. In 2D HFF, the flow rate ratio was still kept as 50:1:50, while this ratio was set to 15:3:15 for the acoustofluidic device to keep at a flow rate ratio of 10:1. When comparing nanoprecipitation, we found that the acoustofluidic device can successfully prevent polymer aggregation while such aggregation occurred quickly within 2D HFF microchannel (Figure 3.6C). At 1 min, slight polymer aggregation appeared at the interfacial region between aqueous sheath streams (2D HFF in Figure 3.6C). This event further accumulated from 1 min to 6 min and restricted the mobility of polymers, resulting in device fouling. When the concentration of PLGA_{50k}-PEG_{5k} was increased to 90 mg/mL in 2D HFF, microscale polymer fibers were observed both in the microchannel interior and on the microchannel wall in less than 10 s of operation. This observation suggests that

aggregation can occur not only between hydrophobic PLGA and PDMS, but also between hydrophobic PLGA molecules themselves.

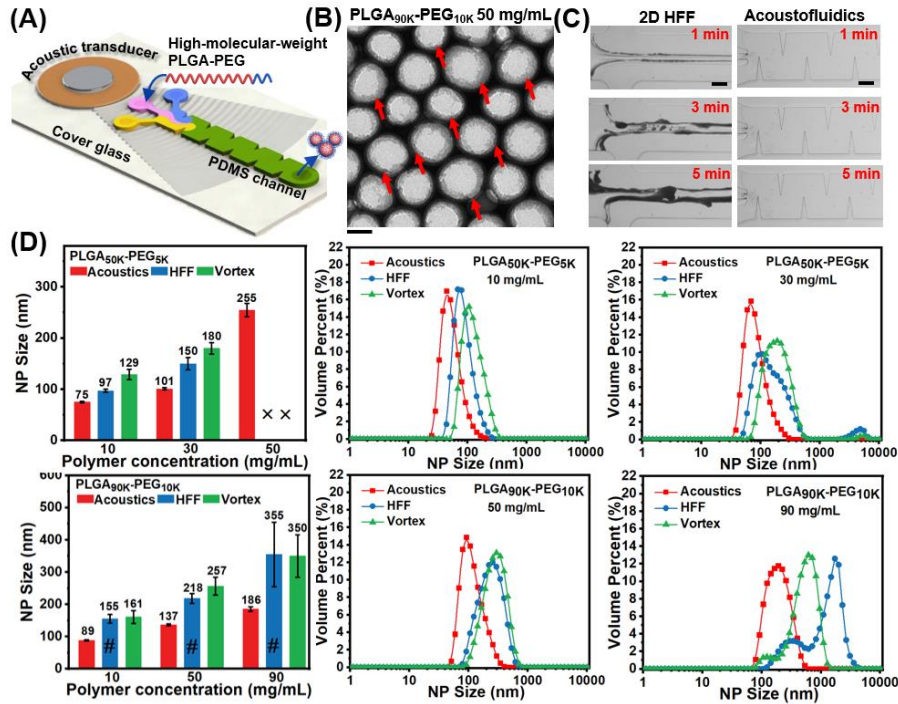


Figure 3.7: Size-tunable synthesis of PLGA-PEG nanoparticles from high-molecular-weight polymers. (A) Schematic of acoustofluidic device with high-molecular-weight PLGA-PEG injected in the middle of microchannel. (B) TEM image of acoustofluidic synthesized nanoparticles from PLGA_{90K}-PEG_{10K} at 50 mg/mL. The red arrows refer to the PEG shell layers. Scale bar: 100 nm. (C) Comparison of polymer aggregation of PLGA_{90K}-PEG_{10K} at 50 mg/mL within 2D HFF and acoustofluidic microchannel. Scale bar: 200 μm. (D) The dependence of nanoparticle sizes and size distributions of synthesized nanoparticles from PLGA_{50K}-PEG_{5K} and PLGA_{90K}-PEG_{10K} on polymer concentration, as well as the synthesis method. Here, X represents the failure of nanoparticle generation and # refers to the occurrence of polymer aggregation.

After validating the macroscopic elimination of polymer aggregation, we then compared the size and monodispersity of the synthesized nanoparticles. We first measured the mixing time of water, 30 mg/mL PLGA_{50K}-PEG_{5K}, and water at a flow rate of 25, 5, and 25 μL/min, respectively. The mixing time is observed to be less than 3 ms,

indicating an ultrafast, complete mixing (Figure 3.1F). Figure 3.7A shows the schematic of the acoustofluidic device with high-molecular-weight PLGA-PEG injected in the middle of the microchannel. Figure 3.7B is the TEM image of the acoustofluidic synthesized nanoparticles from PLGA_{90K}-PEG_{10K} at 50 mg/mL, where the PEG shell layers are clearly observed and represented by the red arrows. This successful assembly preserves the nanoparticle structure of PLGA core and PEG shell layer. In Figure 3.7C, polymer aggregation is prevented within the acoustofluidic microchannel, which is consistent with the construction of hydrophilic PEG shell layer on PLGA cores in Figure 3.7B. Figure 3.7D shows the average size and size distributions of PLGA_{50K}-PEG_{5K} nanoparticles and PLGA_{90K}-PEG_{10K} nanoparticles at different concentrations yielded by 2D HFF, bulk vortexing method, and the acoustofluidic devices. The driving voltage is kept at 38 V_{PP}. At PLGA_{50K}-PEG_{5K} 10 mg/ml, the flow rates were 25 μ L/min, 10 μ L/min, and 25 μ L/min for water, polymer and water stream, respectively. At high concentration and molecular weight, the flow rate is 25, 5, and 25 μ L/min for water, polymer and water stream, except for PLGA_{50K}-PEG_{5K} at 50 mg/mL (15, 3, and 15 μ L/min). For PLGA_{50K}-PEG_{5K}, three polymer concentrations (10, 30, and 50 mg/mL) were applied because at 90 mg/mL the microchannel is blocked immediately. For PLGA_{90K}-PEG_{10K}, polymer precursors with higher concentrations (10, 50, and 90 mg/mL) were applied since the longer hydrophilic PEG chains (10 K) could better prevent hydrophobic PLGA aggregation. The acoustofluidic synthesis platform consistently generated nanoparticles with the narrowest

dispersity and the smallest size and size variation among different measurements. In contrast, bulk and 2D HFF methods yielded nanoparticles with distinctly larger sizes and size variations, that is, poor reproducibility (Figure 3.7D). Especially for PLGA_{50K}-PEG_{5K} at 50 mg/mL, both 2D HFF and bulk methods were unable to produce nanoparticles owing to aggregation (indicated by X, Figures 3.6C, and 3.7D). These results demonstrate that the acoustofluidic synthesis platform allows the size-tunable synthesis of homogenous PLGA-PEG nanoparticles from high molecular weight polymers.

3.3.4. Multiple Reagent Mixing for Chitosan Nanoparticle Synthesis

In nanoparticle synthesis, rapid, yet uniform mixing of multiple liquids may be required. This requirement, however, is quite challenging for many existing microfluidics-based synthesis methods.^{7, 136, 137} With an active-mixing strategy, our platform can easily blend multiple liquids together at different flow rate ratios. As an example, our acoustofluidic device can mix three liquids at a flow rate ratio of 1:1:1 (Fig. 3.8A). When the transducer is off, the three liquids form a laminar flow (Figure 3.8A: Left), whereas when the transducer is on, they are rapidly and completely mixed after passing the first pair of sharp-edge structures (Figure 3.8A: Right). Having demonstrated the mixing of three liquids, we then synthesize chitosan NPs by mixing 0.5 mg/mL chitosan solution, water, and 1 mg/mL adenosine triphosphate solution (ATP), where the water stream serves to isolate the chitosan solution from the ATP solution to minimize pre-reaction between them before synthesis. In this demonstration, we fix the total flow rate in the

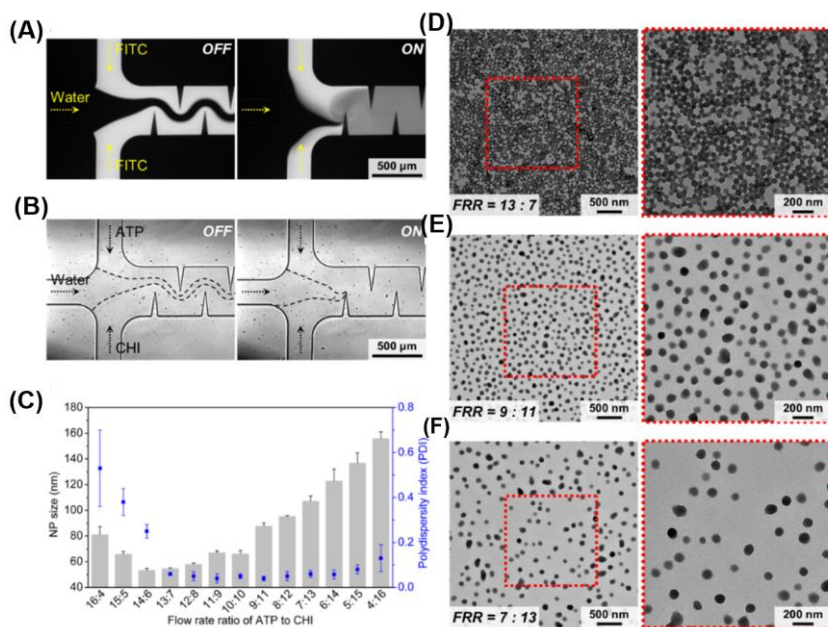


Figure 3.8: Synthesis of chitosan nanoparticles based on the nanocomplexation (NCP) mechanism using the acoustofluidic device. (A) Fluorescent images showing the mixing performance of our acoustofluidic device for mixing three liquids. (B) The acoustofluidic device in operation showing the synthesis of chitosan NPs by mixing together ATP (-), water and chitosan solutions (+). (C) Average size and polydispersity index of chitosan NPs synthesized at different ATP/chitosan flow rate ratios, where the total flow rate and flow rate of water are set to 30 and 10 $\mu\text{L}/\text{min}$, respectively, and the experiments are conducted under the driving voltage of 30 V_{PP} . TEM images of chitosan NPs synthesized at the flow rate ratio of (D) 13:7, (E) 9:11, and (F) 17:3, confirming the size of chitosan NPs synthesized.

channel and the water's flow rate to 30 and 10 $\mu\text{L}/\text{min}$, respectively, while varying the flow rate ratio of ATP/chitosan solutions from 16:4 through 4:16. When the device is off, chitosan solution, water, and ATP solution form a laminar flow having clear interfaces (Figure 3.8B: OFF); once activated, our device can completely mix these three solutions together without any fluidic interfaces observed (Figure 3.8B: ON), thus forming chitosan NPs *via* ATP-initiated ionic gelation.¹¹²

At first glance, each flow rate ratio yields a distinct size distribution, and reducing the flow rate ratio shifts the size distribution towards larger NPs sizes. By adjusting the flow rate ratio from 16:4 to 4:16, we can produce chitosan NPs with an average size ranging from 53 to 155 nm and a polydispersity index ranging from 0.04 to 0.53 (Figure 3.8C). When prepared at flow rate ratios from 16:4 to 14:6, the size of synthesized chitosan NPs decreases from 128 to 53 nm as the flow rate of the chitosan solution is raised, along with a wide size distribution (polydispersity index = 0.59 to 0.25). Between the ratios of 14:6 and 4:16, the size increases from 54 to 155 nm as the flow rate of the chitosan solution is increased, but features a narrow size distribution (polydispersity index = 0.06 to 0.16). Chitosan NPs produced at the ratio of 13:7 have a relatively uniform size of 54.6 ± 0.56 nm and a relatively narrow size distribution (polydispersity index = 0.06 ± 0.007), thereby identifying an optimal flow rate ratio to synthesize chitosan NPs using our device. Figures 3.8D, 3.8E, and 3.8F show the TEM images of chitosan NPs prepared at the ratio of 13:7, 9:11, and 7:13, respectively, confirming the size and uniformity of chitosan NPs we prepared. Supplementary TEM images also verify the size and uniformity for chitosan NPs synthesized at other flow rate ratios. Furthermore, we synthesize chitosan NPs using chitosan/ATP solutions of different concentrations (chitosan = 1.0 mg/mL; ATP = 0.5 mg/mL). After modifying the concentration, we produce the smallest chitosan NPs (49.5 ± 2 nm) at the flow rate ratio of 15:5, suggesting that 15:5 is the optimal flow rate ratio at these given concentrations. With this optimal ratio, we then demonstrate that the size of

chitosan NPs can be tuned from 42 to 98 nm by adjusting the driving voltage from 0 to 50 V_{PP} . These results demonstrate that by using our device, we can identify an optimal flow rate ratio, for given reagent concentrations, to prepare chitosan NPs with desired properties. The results also demonstrate that our platform can synthesize NPs where mixing multiple reagents at different flow rate ratios is required.

3.3.5. Sequential Nanoprecipitation for Core-Shell Nanoparticle Synthesis

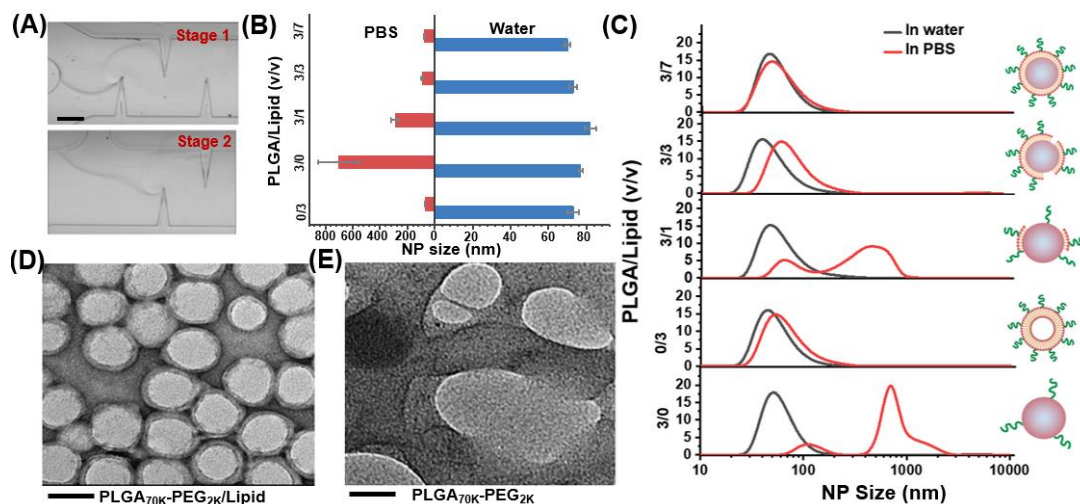


Figure 3.9: Sequential nanoprecipitation for core-shell PLGA_{70K}-PEG_{2K}/lipid nanoparticles synthesis. (A) Microscopic images showing the solvent exchange of PLGA-PEG solution with water solution in the first stage at the beginning of the sharp-edges, and the mixing of PLGA core solution with lipid solution in the second stage in the middle of the sharp-edges. Scale bar: 200 μm . (B) Determination of lipid coverage on PLGA_{70K}-PEG_{2K} NPs. As the ratio of PLGA to lipid increases, size of the hybrid PLGA_{70K}-PEG_{2K}/lipid is decreased. (C) Size distributions in PBS and water with the variation in the ratio of PLGA to lipid. Complete coverage of lipid on PLGA core is observed at a PLGA to lipid ratio of 3:7. Below this ratio, the inadequate lipid coverage leads to aggregated NPs in PBS. (D) TEM image of core-shell PLGA_{70K}-PEG_{2K}/lipid nanoparticles. Scale bar: 50 nm. (E) TEM imaging of polymer aggregation of PLGA_{70K}-PEG_{2K} nanoparticles. Scale bar: 50 nm.

Sequential nanoprecipitation for hierarchical nanoparticles preparation enables the development of novel multifunctional nanomedical systems. Specifically, PLGA-lipid nanoparticles can entrap hydrophilic agents in lipid shells and hydrophobic agents in PLGA cores.⁶⁹ Chitosan/Eudragit core-shell nanoparticles can release therapeutic molecules in the targeted PH environment.¹¹³ However, the current 3D microfluidic devices for sequential nanoprecipitation requires precise coaxial control¹²⁵ and the 2D devices complicate the intermediate procedures by using two separate devices.⁵ Here, we demonstrate a two-step sequential nanoprecipitation for core-shell PLGA_{70K}-PEG_{2K}/lipid nanoparticle synthesis with high molecular weights.

Figure 3.9A shows the two-step nanoprecipitation for generating core-shell PLGA_{70K}-PEG_{2K}/lipid nanoparticles. In the first stage, the PLGA_{70K}-PEG_{2K} solution is completely mixed within a water solution, forming the PLGA polymer core with few PEG chains extending into the water molecules. In the second stage, the polymer core solution is mixed again within a lipid solution. Due to the high ratio of PLGA to PEG (35:1), the majority of the surface area of the PLGA cores remains uncovered and exposed.⁴⁷ The small amount of PEG (2 kDa) is utilized to prevent aggregation between the high-molecular-weight PLGA molecules (70 kDa). Eventually, under the hydrophobic attraction between the PLGA and the lipid,^{138, 139} lipid molecules are assembled on the surface of the PLGA cores (Figure 3.9A). To ensure that the synthesized nanoparticles are hybrid particles rather than a combination of liposomes and PLGA nanoparticles,

different polymer components were used, such as PLGA-PEG alone, lipid (DPPC/DSPE-PEG) alone, or a combination of both. A sufficient coverage of lipid on a PLGA core would prevent aggregation of PLGA NPs in PBS.⁶⁹ Size stability of nanoparticles was analyzed in water and PBS as the lipid coverage changes by dynamic light scattering (Figure 3.9B). In Figure 3.9B, PLGA_{70K}-PEG_{2K} nanoparticles suffer from a dramatic increase in size from water to PBS, revealing a strong aggregation between uncovered polymer cores. Liposome nanoparticles only show a slight increase, exhibiting a favorable stability. By decreasing the PLGA_{70K}-PEG_{2K}/lipid ratio from 3:1 to 3:7, the hybrid PLGA_{70K}-PEG_{2K}/lipid nanoparticles stabilize in both water and PBS. The size increase in the case of 3:1 PLGA to lipid indicates that there is not enough lipid layer to further prevent the aggregation of PLGA_{70K}-PEG_{2K} NPs in water, and the addition of lipid layers leads to an increase in NP size. In Figure 3.9C, a single volume peak rather than a double peak is observed in the size distribution of PLGA_{70K}-PEG_{2K}/lipid with a ratio of 3:3 and 3:7. This further confirms the hybrid core-shell nanoparticles structure. The core-shell structure of PLGA_{70K}-PEG_{2K}/lipid was then revealed by TEM imaging (Figure 3.9D), while its counterpart of PLGA_{70K}-PEG_{2K} displays strong aggregation phenomenon and the absence of a shell layer (Figure 3.9E). These results suggest that lipid molecules are assembled on the PLGA core and that the acoustofluidic device is capable of conducting sequential nanoprecipitation.

3.4. Conclusions

We present an acoustofluidic platform to synthesize nanoparticles from high-molecular-weight polymers in a size and structure-controlled manner. By systematically evaluating the influence of device configuration parameters, the acoustofluidic devices are fine-tuned to achieve micromixing in the entire microchannel with a timescale down to 2-3 ms. The ability to perform ultrafast, complete mixing enables our acoustofluidic platform to synthesize reproducible PLGA-PEG nanoparticles with high polymer precursor molecular weight and concentrations that previously was not possible with bulk mixing or most microfluidic approaches. The underlying mechanism results from diminished polymer interaction by uniform dispersion. Nanoparticles produced by our acoustofluidic platform exhibited favorable monodispersity and smaller nanoparticle diameter relative to 2D HFF or bulk methods.

Additionally, this device provides a new method for sequential self-assembly in a single device within a 2D structure. The core/shell PLGA-PEG/lipid nanoparticles were prepared by the formation of PLGA core in the first stage and the coverage of a lipid layer in the second stage. As each sharp-edge structure acts as an active mixing site, three or four sequential nanoprecipitation steps could be achieved in the future for multi-layer nanoparticle self-assembly. These synthesis abilities are especially desired for novel multifunctional therapeutic nanosystems. With its simple 2D structure and complete, ultrafast mixing nature, our acoustofluidic-based synthesis platform can harness the

benefits of microfluidics in material synthesis to a broad set of scenarios, especially in applications where high-molecular-weight polymer, viscous polymers, or multiple polymer precursors are needed.

4. A Disposable Acoustofluidic Chip for Nano/Micro Particle Separation using Unidirectional Acoustic Transducers

Separation of nano/micro particles based on surface acoustic waves (SAWs) has shown great promise for biological, chemical, and medical applications ranging from sample purification to cancer diagnosis. However, the permanent bonding of a microchannel onto relatively expensive piezoelectric substrates and excitation transducers renders the SAW separation devices non-disposable. This limitation not only requires cumbersome cleaning and increased labor and material costs, but also leads to cross-contamination, preventing its implementation in many biological, chemical, and medical applications. Here, we demonstrate a high-performance, disposable acoustofluidic platform for nano/micro particle separation. Leveraging unidirectional interdigital transducers (IDT), a hybrid channel design with hard/soft materials, and the tilted-angle standing SAW (taSSAW), our disposable acoustofluidic devices achieve acoustic radiation forces comparable to those generated by existing permanently bonded, non-disposable devices. Our disposable devices can separate not only microparticles but also nanoparticles. Moreover, it can differentiate bacteria from human red blood cells (RBCs) with a purity of up to 96%. Altogether, we developed a unidirectional IDT-based, disposable acoustofluidic platform for micro/nano particle separation that can achieve high separation efficiency, versatility, and biocompatibility.

4.1. Motivation

Separation of nano to microscale particles such as exosomes,^{33, 140} bacteria,¹⁴¹⁻¹⁴³ and cells^{144, 145} is of great interest in a variety of assays from fundamental biological studies to medical applications, including drug screening, disease diagnosis, and cell biology.^{104, 105, 146} Towards the goal of separating bioparticles with high purity, yield, versatility, and biocompatibility, researchers are continuously developing new separation technologies by introducing a variety of physical principles, such as magnetophoresis,¹⁴⁵ dielectrophoresis,¹⁴⁷ acoustofluidics,¹⁴⁸ hydrodynamics,¹⁴⁹ and photophoresis.¹⁵⁰ Amongst these physical principles, surface acoustic wave (SAW)-based separation has recently emerged as a promising technology, because it does not require labelling of target particles/cells,^{110, 148, 151} uses relatively low electrical power,^{102, 148} and has high precision and versatility.^{66, 102, 152-159} With these advantages, SAW-based devices^{22, 33, 36, 110, 144, 155, 160-164} have shown outstanding potential for separating microvesicles from red blood cells (RBCs),¹⁶² exosomes from whole human blood,³³ human breast cancer cells from leukocytes,¹⁴⁴ and bacteria from peripheral blood mononuclear cells.¹⁴¹

Ideally, the SAW separation chips should be conveniently replaced and disposed. Disposable chips will help supply a sterile system, eliminate sample cross-talk, and facilitate simple maintenance. However, in most SAW separation chips, the microfluidic chamber is permanently bonded onto a piezoelectric substrate and excitation transducers. Since the piezoelectric substrate and excitation transducers are often too expensive to be

disposed, this limitation necessitates cumbersome cleaning processes and can induce cross-contamination, especially for biological and clinical samples. Therefore, it is important to develop disposable SAW chips in which the microfluidic cartridges can be separated from the piezoelectric substrate and excitation piezoelectric transducers. Thus, only the microfluidic cartridges are disposable, while the piezoelectric substrate and excitation piezoelectric transducers are reusable. To date, disposable SAW devices have been introduced into different scenarios due to their significance for real-world applications. Examples include droplet splitting¹⁶⁵ and sorting,^{110, 166, 167} and particle pattern,^{168, 169} deflection,¹⁶¹ and separation.¹⁷⁰ For separation, Ma *et al.* separated 15 μm polystyrene (PS) particles from 10 μm PS particles in a disposable microchannel with polydimethylvinylsiloxane (PDMS) post using traveling SAWs.¹⁷⁰ Despite these progressions, the performance of the currently demonstrated disposable SAW devices are not as good as the permanently bonded SAW devices. For example, nanoparticle separation or cell separation using a disposable SAW device has not been demonstrated. This is likely due to the weak acoustic energy in disposable SAW devices.

In this work, we present a unidirectional interdigital transducers (IDTs) based, tilted-angle standing SAW (taSSAW) chip for high-performance separation of nano-to-micro sized particles in a continuous flow. To effectively transmit acoustic energy into our disposable acoustofluidic (*i.e.*, the fusion of acoustics and microfluidics)^{22, 56, 61, 103, 115, 117, 170-183} devices, a hybrid hard/soft polydimethylsiloxane (PDMS) microchannel was designed.

The hard PDMS, which is different from the commonly used soft PDMS^{184, 185}, has a low acoustic attenuation coefficient^{186, 187} and can be fabricated as an ultra-thin PDMS film, enabling the increase of acoustic pressure in disposable microchannels. As a result, the intensity of acoustic radiation force achieved in our disposable acoustofluidic device is comparable to that in permanently bonded devices. Four different sized particles were precisely deflected into separate and distinguishable streams, indicating its accuracy and versatility. We have achieved separation of different particles with a wide size range from 200 nm to 10 μm in a single device, including the separation of 2 and 4.5 μm polystyrene (PS) particles, 110 nm PS and 1 μm PS particles, 400 nm PS and 660 nm silicon dioxide (SiO_2) particles, and 100 nm PS and 200 nm Silver (Ag) particles. Additionally, our disposable device showed a separation purity of up to 96% when separating *Escherichia coli* (*E. coli*) from human RBCs.

Compared to previous reported disposable acoustofluidic devices that use travelling SAW or standing SAW with bidirectional IDT designs,^{110, 161, 165, 169, 170} our taSSAW device generated with a unidirectional IDT design has the advantage of generating a stronger acoustic field and achieving a larger separation displacement (distance variation between two types of particles in the direction perpendicular to fluid flow). This advantage is achieved by the unidirectional IDT design, the taSSAW design, and the hybrid hard/soft PDMS microchannel. Our unidirectional IDT based taSSAW device drives particles using a strong, periodic acoustic radiation force. With strong acoustic gradients and large separation displacements, our

disposable acoustofluidic chip is capable of precisely separating not only microparticles but also nanoparticles. In contrast, the existing disposable acoustofluidic devices can only manipulate large micro-objects.^{161, 169, 170} Our chip is also the first disposable acoustofluidic device that demonstrates separation of biological cells. With its advantages of being versatile, precise, label-free, and low-cost, we believe that our unidirectional IDT based disposable devices can facilitate the development of acoustofluidic technologies into point-of-care systems.

4.2. Materials and Methods

4.2.1. Device Fabrication

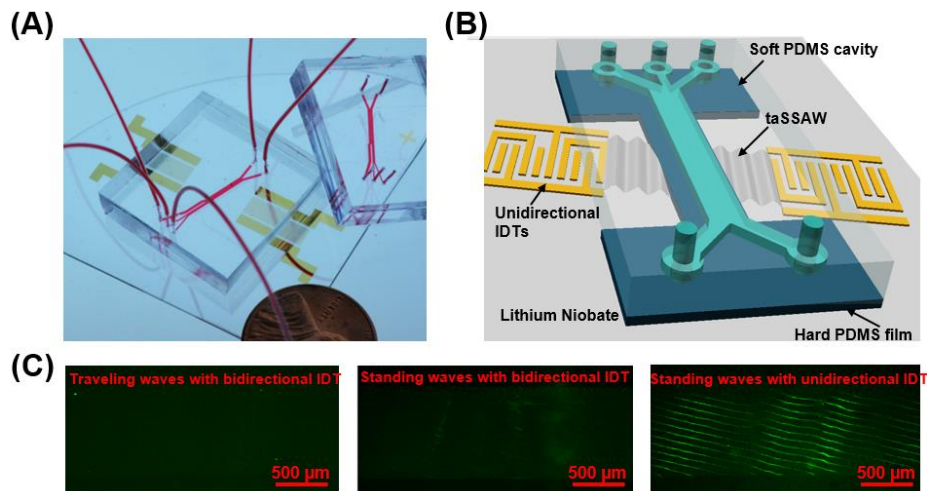


Figure 4.1: Principle of the disposable separation device. (A) Photograph and (B) schematic for the disposable acoustofluidic separation chip using unidirectional IDT based taSSAW design. (C) Patterning of 400 nm PS particles within disposable hard/soft microchannels with a 13 μm hard PDMS film at 20 V_{PP} using traveling waves with a bidirectional IDT design (left), standing waves with a bidirectional IDT design (middle), and standing waves with a unidirectional IDT design (right), respectively. For all these three designs, disposable microchannels were placed on SAW substrates with a relative orientation of 15° to IDT for comparison.

As shown in Figure 4.1A, the unidirectional IDT based disposable acoustofluidic chip consists of a reusable SAW transducer and a disposable microchannel. To fabricate a reusable SAW transducer, a 128° Y-cut X-propagation LiNbO₃ (PWLN-431232, Pmoptics, USA) wafer was chosen as the piezoelectric substrate. A set of 80 pairs of unidirectional IDTs were patterned onto the LiNbO₃ using photolithography, followed by a deposition of Cr (50 Å) and Au (500 Å) through e-beam evaporation (CHA Industries, USA). After a lift-off process, IDTs were obtained with a feature size of 10 μm and a wavelength of 120 μm, corresponding to a resonance frequency of 33.13 MHz.

In Figure 4.1B, the disposable microchannel was fabricated by bonding the top soft PDMS cavity to the bottom Gelest hard PDMS film. The top PDMS cavity with 800 μm width and 75 μm depth was obtained by standard soft-lithography. Briefly, after obtaining an SU-8 mold, a 10:1 mixture of soft PDMS base and curing agent (Sylgard184 Silicone Elastomer Clear, Ellsworth, USA) was degassed, poured onto the mold, cured for 1 h and peeled off. To fabricate the Gelest hard PDMS film, a 1:1 mixture of PDMS base and curing agent (PP2-RG07, Gelest, Inc., USA) was spin-coated on a clean silicon wafer via a spin coater (WS-650MZ-23NPPB, Laurell Inc., USA) and partially cured at 65 °C for 20 min. Gelest hard PDMS is a different composite material relative to Sylgard 184 PDMS, and has not been applied in acoustofluidic devices previously. The hardness was measured as 8.62 MPa for Gelest hard PDMS, and 4.11 MPa for Sylgard soft PDMS using nanoindenter (Hysitron Ubi-1, USA). The acoustic attenuation coefficient and speed of

sound in Gelest hard PDMS and Sylgard soft PDMS were also measured (Figure 4.2). Then, this Gelest hard PDMS film was bonded with the Sylgard soft PDMS cavity and baked at 65 °C overnight. During this process, the soft PDMS cavity was treated with oxygen plasma to enhance its bonding strength with the Gelest hard PDMS film. Finally, with van der Waals forces induced self-adhesion, the disposable microchannel was gently pressed and attached to a SAW substrate at a relative orientation of 15° through markers on LiNbO₃, forming a disposable acoustofluidic chip.

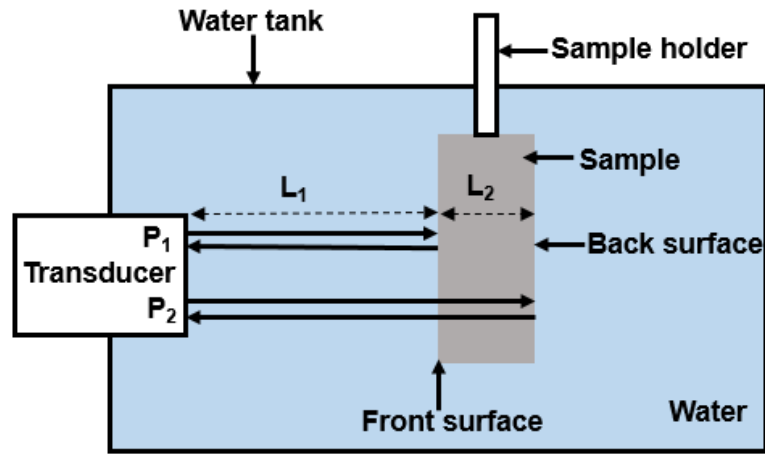


Figure 4.2: Schematic of the experimental setup for acoustic performance measurement. A sample with a thickness of L_2 is submerged in water. One transducer facing the sample at a known distance of L_1 excites an acoustic wave and receives its reflection from the back and front surface of the sample.

Table 2: Acoustic performance comparison between “hard PDMS” and “soft PDMS”

Material	Speed of sound (m/s)	Acoustic attenuation coefficient (dB/cm)				
		1 MHz	2 MHz	3 MHz	4 MHz	5 MHz
“Hard PDMS”	1166 m/s	1.8	2.6	3.5	3.8	4.4
“Soft PDMS”	996 m/s	2.0	5.3	9.2	12.9	18.3

For the comparison of different disposable acoustofluidic devices, disposable microchannels with different types of PDMS film were fabricated, including $13 \pm 0.8 \mu\text{m}$ (2,200 rpm/min for 3 mins) and $20 \pm 1.5 \mu\text{m}$ (1,500 rpm/min for 3 mins) Sylgard soft PDMS films, and $13 \pm 0.5 \mu\text{m}$ (1,500 rpm/min for 3 mins) and $20 \pm 1 \mu\text{m}$ (1,000 rpm/min for 3 mins) Gelest hard PDMS films. Gelest hard PDMS curing agent and base were mixed at a ratio of 1:1, while soft Sylgard PDMS curing agent and base were mixed at 1:10. Note that attempts have been made but failed in fabricating a PDMS film at a mixing ratio of 1:1 using Sylgard 184 PDMS. The thickness of PDMS films was measured using a profilometer (Dektak 150, Bruker, USA). These different disposable PDMS channels were then assembled on the same IDT substrate, respectively. For the comparison of non-disposable and disposable acoustofluidic devices, the same IDT substrate is then permanently bonded with soft PDMS cavity through oxygen plasma treatment, to fabricate non-disposable acoustofluidic devices. For clarification, the Gelest hard PDMS and Sylgard soft PDMS will be referred as “hard PDMS” and “soft PDMS” in the later sections.

4.2.2. Experimental Setup

Different PS particles included non-fluorescent PS particles (10 μm , 6 μm , 4.5 μm , and 1 μm Polysciences, USA), green fluorescent PS particles (2.0 μm , 1.0 μm , 400 nm, and 110 nm, Bangs Laboratories, USA), Ag nanoparticles (200 nm, 796360, Sigma-Aldrich, USA) and SiO₂ nanoparticles (660 nm) were suspended in DI water containing 0.5 %

sodium dodecyl sulfate (SDS) as samples. To prepare the mixture of bacteria and RBCs, *E. coli* (8739, ATCC, USA) was cultured in a sterilized Miller's LB Broth medium (20716002, Cellgro, USA), and then stained with a BacLight kit (L7007, Invitrogen, USA). After that, 3 μL of RBCs (SER-10MLRBC, Zen-Bio, USA) and 20 μL of cultured *E. coli* were mixed in 1 mL PBS filtered with a 0.2 μm filter (514-0072, VWR, USA). The final concentration for RBCs was calculated as approximately 1.1×10^7 particles/mL using a hemocytometer, and that for *E. coli* was measured as approximately 5.0×10^6 particles/mL via a microreader (BioTek, USA). Before experiments, all the microchannels were treated with 1% bovine serum albumin (Sigma-Aldrich, USA) solution for 5 min to prevent the adsorption of particles on microchannel.

During all the measurements, SAW devices were driven by a function generator (E4422B, Agilent, USA) and an amplifier (25A250A, Amplifier Research, USA). The targeted sample and sheath fluids were injected into microchannel inlets by a syringe pump (neMESYS, Cetoni GmbH, Germany). The flow rate of sample and two sheath fluids were set as 2, 2, and 6 $\mu\text{L}/\text{min}$, respectively, for particle and bacteria separation unless otherwise stated, while they were 0.3, 10, and 10 $\mu\text{L}/\text{min}$, respectively, for hydrodynamic focusing. For particle deflection and separation, and bacteria separation, SAW devices were placed on a Peltier cooling system (TEC1-12730, Hebei I.T., China) and experimental processes were monitored with a charge-coupled device (CCD) (CoolSNAP HQ2, Photometrics, USA) on an upright microscope (BX51W1, Olympus, Japan). For

particle velocity test, the processes of particle patterning at different input voltages were recorded with a high-speed camera (500K-M1, Photron, Japan) on an inverted microscope (Eclipse Ti, Nikon, Japan) and analyzed using ImageJ (NIH, USA). Separated samples were collected from two microchannel outlets with 1.5 mL microtubes (8081811, Sarstedt, Germany).

4.2.3. Sample Characterization

In order to provide a benchmark comparison for our acoustofluidic devices, SEM and flow cytometry were applied to analyze separation performance. For SEM imaging, separated particles were dropped on a clean silicon wafer, dried in a chemical hood, sputtered with gold, and then observed with an electron microscope (FEI XL30, FEI, USA). For flow cytometry, 50 μ L of mixed *E. coli* and RBCs, separated *E. coli*, and separated RBCs were diluted with 1 mL PBS in a 5 mL tube (352235, Falcon, USA), respectively. After that, the samples were tested by a flow cytometer (BD FACSCanto B, USA) and analyzed using FlowJo software (FlowJo, FlowJo, LLC, USA).

4.3. Results and Discussion

4.3.1. Characterization of Disposable Acoustofluidic Chips with Hybrid Hard/Soft Material Design

To develop a disposable acoustofluidic chip for bioparticle separation, we introduce taSSAWs generated by unidirectional IDTs into a disposable PDMS microchannel. Figures 4.1A and B illustrate the concept and working mechanism for the disposable acoustofluidic chip, which consists of a reusable SAW substrate and a

disposable PDMS microchannel. The SAW substrate is a LiNbO₃ patterned with a pair of parallel unidirectional distributed IDTs (Figure 4.3) to address the weak acoustic energy generated in disposable microchannels. In Figure 4.4, the unidirectional IDT proves to have a much larger transmission energy of S21 in the “toward” configuration relative to the “away” configuration, while bidirectional IDT has almost equivalent S21 in “toward” and “away” configurations, demonstrating the directionality of our unidirectional IDTs. Specifically, the peak value of S21 for unidirectional IDTs is *ca.* -5 dBm while it is *ca.* -11.2 dBm for bidirectional IDTs, indicating that under the same experimental conditions, unidirectional IDTs can generate SAWs with higher vibrational amplitudes than traditional bidirectional IDTs. The disposable microchannel has a soft PDMS cavity enclosed by a hard PDMS film. Under the Van der Waals forces induced self-adhesion,^{165, 188} the closed, disposable microchannel was assembled between IDTs on the LiNbO₃ at an orientation of 15° relative to IDTs. When the IDTs are activated, two identical and opposing traveling SAWs would be generated, and propagate along the surface of the LiNbO₃. These traveling SAWs constructively interfere with each other and form a standing SAW. Such a standing SAW generates parallel pressure nodal lines at the specific angle of 15° with respect to the disposable microchannel, termed as “taSSAW” (Figure 4.1B). This taSSAW transmits through the hard PDMS film and couples into disposable microchannels. Once transmitted taSSAWs meet with particles, acoustic radiation force would be exerted on particles toward the pressure nodal lines.^{34, 122} With particle

patterning, we further compared traveling waves with a bidirectional IDT design, standing waves with a bidirectional IDT design, and standing waves with a unidirectional IDT design in Figure 4.1C. The results demonstrate that standing waves with a unidirectional IDT design can generate much stronger acoustic field and larger acoustic radiation force on particles than the other two designs.

Different particles with different intrinsic physical properties (such as size, density, and compressibility) would experience differential acoustic radiation forces and move differently in the microfluidic channel. This discrepancy in movement can be leveraged to achieve micro/nano particle separation. Meanwhile, as the pressure nodal lines lie across the whole disposable microchannel at the angle of 15° , the separation

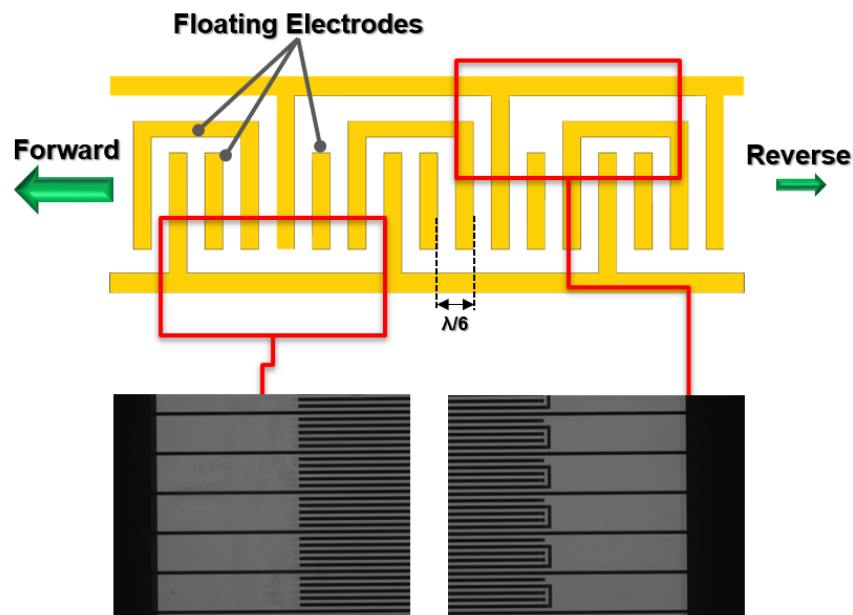


Figure 4.3: The unidirectional interdigital transducer (IDT) design with floating electrodes. The floating electrodes increase the intensity of the forward wave by decreasing the reverse Rayleigh-mode surface acoustic waves (SAWs).

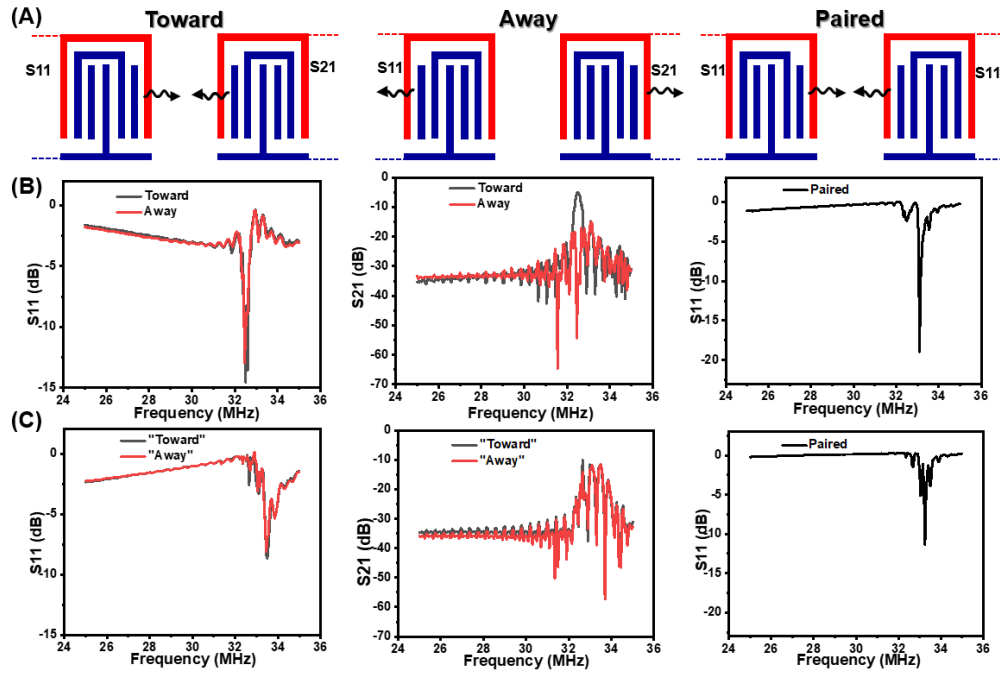


Figure 4.4: Comparison of unidirectional IDT and bidirectional IDT. (A) Schematic toward, away, and paired IDT configurations for the reflection S_{11} and transmission S_{21} measurements. Here, “toward” configuration means that two identical SAWs propagate toward each other, while “away” configuration means that two identical SAWs propagate against each other. For both “toward” and “away” configurations, one side of the IDTs is measured as S_{11} and the other side is measured as S_{21} . “Paired” configuration means that a pair of IDTs are connected together and both measured as S_{11} . (B) Unidirectional IDT response as a function of frequency, for the “toward”, “away” and “paired” configurations. (C) Bidirectional IDT response as a function of frequency, for the “toward”, “away” and “paired” configurations. For comparison, the bidirectional IDT are simply designed in an inverse layout for the “toward” and “away” configurations. The results show that the unidirectional IDT has a smaller S_{11} than the bidirectional IDT at the resonance frequency in all three configurations, suggesting a weaker reflection and a stronger resonance effect. More importantly, the unidirectional IDT has a much larger S_{21} in the “toward” configuration relative to the “away” configuration, while the bidirectional IDT has almost equal S_{21} in the “toward” and “away” configurations, demonstrating the directionality of our unidirectional IDT.

displacement would be much larger than the acoustic wavelength. Once finished with a given acoustic separation test, the disposable microchannel can be easily replaced by peeling off the used PDMS-based microfluidic channel and aligning a clean microchannel assembly to the same SAW substrate. Hence, our devices can avoid cross-contamination; meanwhile, they can significantly reduce the average cost for multiple tests, since only the low-price PDMS channel needs to be replaced, while the expensive LiNbO₃ substrate and excitation piezoelectric transducers are reusable.

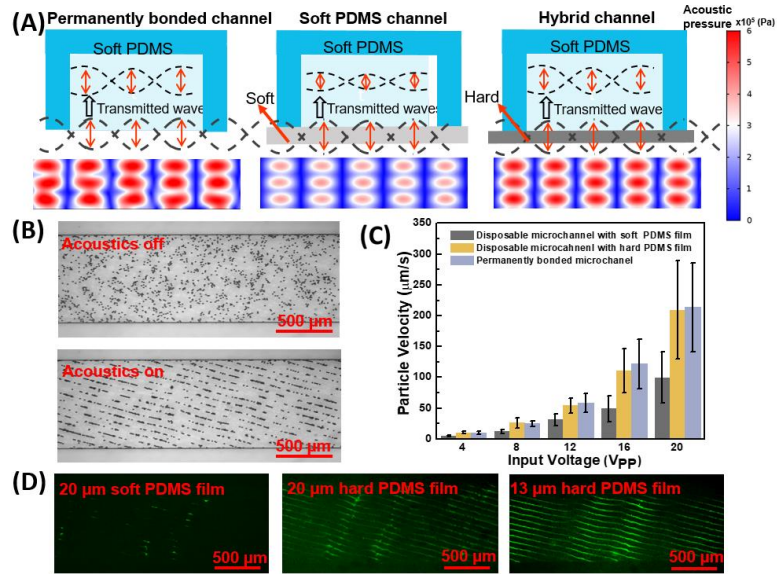


Figure 4.5: The performance of disposable acoustofluidic chips in the absence of fluid flow. (A) Schematic illustrations and corresponding numerical simulations for permanent bonded channel, disposable soft microchannel with a 20 μm soft PDMS film, and disposable hybrid hard/soft channel with a 13 μm hard PDMS film illustrate the influence of coupling layer in acoustic pressure transmission. (B) Patterning of 10 μm PS particles in a disposable acoustofluidic device with a hybrid hard/soft PDMS channel. (C) Quantitative performance comparison of a permanently bonded acoustofluidic device to a disposable device by measuring 10 μm particle velocity during their patterning at different input voltages. (D) Comparison of the tASSAW field by patterning 400 nm PS particle in a disposable channel with a 20 μm soft PDMS film (left), a 20 μm hard PDMS film (middle), and a 13 μm hard PDMS film (right).

The performance of the disposable acoustofluidic device is related to the transmitted taSSAW in closed, disposable microchannels, which generates acoustic radiation force on particles/cells. The acoustic radiation forces are proportional to the square of acoustic pressure.¹⁴⁶ To enhance the acoustic pressure within the disposable microchannel, we employed a hybrid hard/soft PDMS channel to enhance the acoustic transmission. In particular, we bonded a Sylgard soft PDMS cavity onto a 13 μm Gelest hard PDMS film (Figure 4.5A). For comparison, the soft PDMS channel in Figure 4.5A has a thickness of 20 μm due to fabrication limitation. Gelest hard PDMS has a much smaller acoustic attenuation coefficient (≈ 4432 dB/m) than Sylgard soft PDMS (≈ 23798 dB/m), which can reduce acoustic attenuation in PDMS film (Table 2). Additionally, the larger acoustic impedance of Gelest hard PDMS (≈ 1.13 MPa·s/m) compared to Sylgard soft PDMS (≈ 0.96 MPa·s/m) enables a smaller impedance mismatch between water (≈ 1.49 MPa·s/m) and PDMS film, enhancing acoustic transmission (Table 2). Thus, whereas 61.9% of the acoustic pressure is transmitted into soft PDMS channel, the transmitted acoustic pressure is increased to 92.1% in the new hybrid hard/soft PDMS channel (Numerical simulation in Figure 4.5A). When compared to a permanently bonded device, the magnitude of the acoustic radiation force is only reduced by 15.2% within the disposable device using the hybrid hard/soft PDMS channel, whereas the radiation force is reduced by 61.7% within the disposable device using the soft PDMS channel. With this

larger acoustic radiation forces, our disposable device using the hybrid hard/soft PDMS channel would improve its capability to manipulate small particles.

We next quantitatively analyzed the taSSAW acoustic field in permanently bonded devices and disposable devices by calculating particle velocity during manipulation. In Figure 4.5B, when the taSSAW was applied, 10 μm PS particles were patterned homogeneously and periodically along the pressure nodes, indicating uniformly coupled acoustic waves. We have also observed diffractive effects within both disposable microchannels and permanent bonded channels,¹⁸⁹ which do not adversely affect the particle separation process. During this acoustic patterning process, particles were subjected to an acoustic radiation force, which aligned particles from random dispersion to pressure nodes; as such, the particle velocity provides an indication of the acoustic radiation force.¹⁶⁸ The quantitative characterization of 10 μm PS particle velocities during their patterning is given in Figure 4.5C. To ensure accuracy, disposable microchannels with different PDMS films and permanent microchannel were attached on the same SAW substrate. To check the variability between experiments, we measured the particle velocities of four different disposable hybrid channels on the same SAW substrate at 20 V_{PP} (28.2 dBm). The results from these experiments yielded an average velocity of $202 \pm 16.3 \mu\text{m/s}$ (\pm one standard deviation), demonstrating the consistency of our disposable acoustofluidic devices. In comparison with the commonly used, permanently bonded device, the results indicate a 43% to 55% loss of particle velocity when using the

disposable device with a soft PDMS bottom film, but only a 2% to 10% loss for our devices with a hybrid hard/soft PDMS across varying input voltages from 4 to 20 V_{PP} (14.2 to 28.2 dBm). Based on the numerical simulations in Figure 4.5A, the numerical loss difference between disposable devices using the hybrid channel and soft channel is approximately 46.5%, which matches well with the experimental difference (41%-45%). Note that a small mismatch (*c.a.* 10%) exists between the experimental and numerical calculation of the acoustic radiation force discrepancy for disposable devices, which can be attributed to the deviation in the calculation of the acoustic attenuation coefficient. To further examine the influence of the coupling layer on taSSAW field, 400 nm PS particles were patterned using disposable devices with different PDMS film (Figure 4.5D). Clearly, nanoparticles were patterned periodically along the tilted-angle direction via the transmitted taSSAW on both hybrid hard PDMS channels, even with a thickness of 20 μm. With its larger acoustic radiation force, our disposable device has a much greater capability for manipulating small particles. Overall, these results imply that the intensity of acoustic waves generated in our disposable devices is comparable to that in commonly used, permanently bonded devices.

Compared to the reported 85% to 90% loss of particle velocity in previous disposable devices,^{16, 35-39} which cannot be used to separate nanoparticles, the significant improvement in our disposable acoustofluidic device can be attributed to the following reasons. First, the taSSAW generated by unidirectional IDTs provides a strong acoustic

field. Second, in our hybrid hard/soft microchannel design, hard PDMS has a much smaller acoustic attenuation coefficient, larger acoustic impedance, and a smaller film thickness than commonly used soft PDMS, which significantly improves acoustic energy transmission.

4.3.2. Disposable Acoustofluidic Chips for Particle Deflection

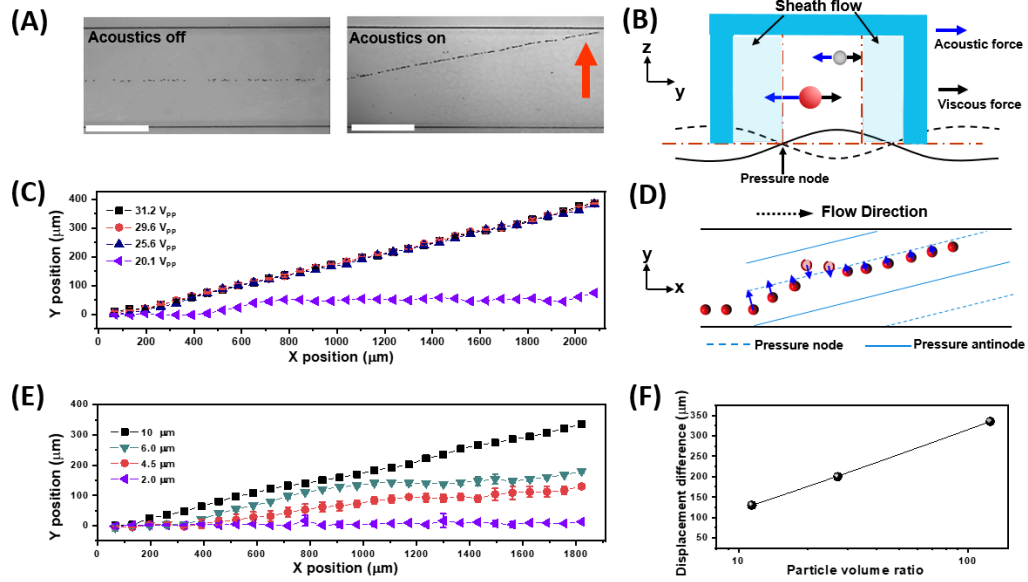


Figure 4.6: Disposable acoustofluidic chips for particle deflection in a continuous flow. (A) Trajectories of 6 μm PS particles with and without taSSAW acoustic field. Scar bar: 500 μm . The red arrow represents the direction of particle deflection, which is consistent with the entire article. (B) Trajectories of 6 μm PS particles at different acoustic intensities. (C) Trajectories of 10, 6, 4.5, and 2.0 μm PS particles at the same acoustic intensity. (D) Schematic for particle position adjacent to pressure node. (E) Schematic of size-based particle deflection with respect to net forces. (F) The relationship between displacement difference and particle volume ratio.

Separation of bioparticles results from discrepancies in their deflections. Using our disposable acoustofluidic devices, we analyzed the relative deflection displacement of particles before conducting particle-separation experiments. To ensure accuracy, three-

inlet hydrodynamic focusing was applied, allowing particles to enter consistently into the same position in the acoustic field. As shown in Figure 4.6A, when the taSSAW was not applied, particles flowed through the microchannel in a single stream. Once the taSSAW was applied, particles were deflected along the pressure node line. The deflection of the particles are determined by the acoustic radiation force (F_r), which pushes particles toward pressure nodal lines, and the Stokes drag force (F_d), which hinders the motion of particles¹⁴⁶ (Figure 4.6B). These two forces can be expressed as follows:

$$F_r = - \left(\frac{\pi p_0^2 v \beta_f}{2\lambda} \right) \varphi \sin(2kL) \quad (4.1)$$

$$F_d = -6\pi\eta r v \quad (4.2)$$

$$\varphi(\beta, \rho) = \frac{5\alpha_p - 2\alpha_f}{2\alpha_p + \alpha_f} \frac{\beta_p}{\beta_f} \quad (4.3)$$

where p_0 , λ , φ , k , and L represent acoustic pressure amplitude, acoustic wavelength, acoustic contrast factor, acoustic wavenumber, and the distance from particle position to the pressure node, respectively, and β_f , η , and ρ_f are the compressibility, viscosity, and density of fluid, respectively. β_p , ρ_p , v , r , and v are the compressibility, density, volume, radius of particles, and the relative velocity of particle to fluid, respectively. Among these parameters, the acoustic contrast factor φ determines the direction of acoustic radiation force. PS particles have positive φ (0.437), and therefore were deflected to pressure nodes.

Figure 4.6C displays the influence of acoustic intensity on the deflection distances (distance of migration of one type of particles in the direction perpendicular to fluid flow) of 6 μm PS particles. With increasing voltage from 20.1 to 31.2 V_{PP} (28.6 to 32 dBm), the

extent of particle deflection first increases, and then remains unchanged. According to Equation (4.1), the increase in drive voltage from 20.1 to 25.6 V_{PP} (28.6 to 30.3 dBm) increases the acoustic radiation force and therefore the net force. In this way, particles at 25.6 V_{PP} (30.3 dBm) would move closer to the tilted-angle pressure node. With a further increase in the drive voltage from 25.6 to 31.2 V_{PP} (30.3 to 32 dBm), particles remained at positions adjacent to pressure node, and cannot pass through the pressure node. Otherwise, the strong acoustic radiation force would drive particles back to pressure node quickly (Figure 4.6D). In other words, the angle of particle deflection is limited by the tilted angle of pressure nodes. Therefore, the difference in displacement between particles can actually be reduced at a high acoustic intensity, meaning that a moderate acoustic intensity is needed to achieve optimum separation performance.

Figure 4.6E shows the relationship between particle deflection and particle size (2, 4.5, 6, and 10 μm). This is in good agreement with the fact that in Equations (4.1) and (4.2), the acoustic radiation force increases proportionally to the volume (r^3) of the particle, but the Stokes drag force increases proportionally to the radius of particle (r). As a result, particles with a larger size move closer to the tilted-angle pressure node, while particles with a smaller size do not have enough net force to move to the pressure node, as shown in Figure 4.6B. Figure 4.6F shows the relationship between particle volume ratio and deflection displacement difference. Here, 2 μm particles were selected as the base, and compared to 10, 6, and 4.5 μm particles, respectively. Based on Equation (4.1), a larger

particle volume ratio should lead to a larger difference in acoustic radiation force, and thus a larger difference in deflection displacement. This reasoning is in good agreement with the result in Figure 4.6F, demonstrating the excellent controllability and sensitivity of our disposable acoustofluidic chips. Our device's controllability enables the deflection of a single stream of particles, while its sensitivity allows the precise size-based differentiation while using a single frequency in a single device.

4.3.3. Disposable Acoustofluidic Chips for Nano/Micro Particle Separation

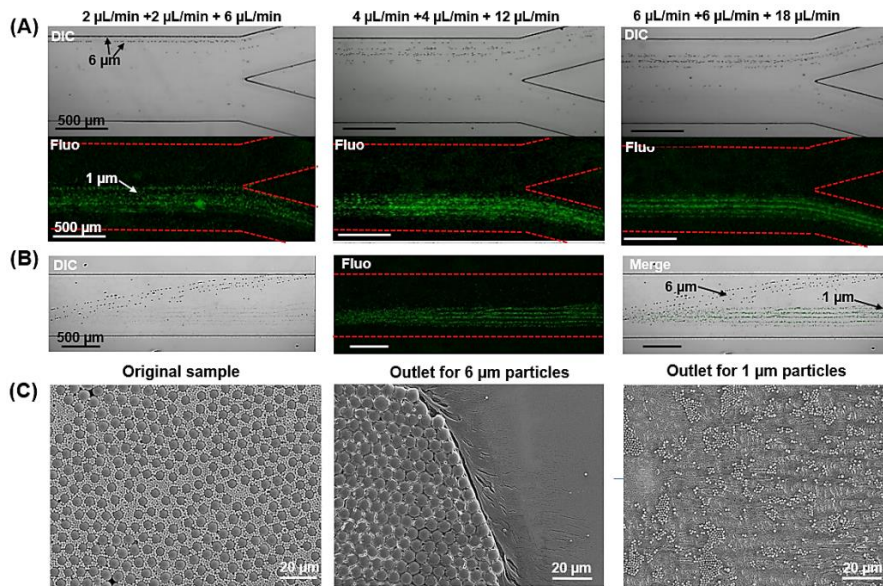


Figure 4.7: The taSSAW field in disposable acoustofluidic chips for the separation of 1 μm fluorescent particles and 6 μm non-fluorescent PS particles. (A) High-performance separation was maintained despite the increased throughput. 2+2+6 $\mu\text{L}/\text{min}$: the flow rates of the sample and the two sheath fluids were 2, 2, and 6 $\mu\text{L}/\text{min}$, respectively. (B) Bright-field, fluorescent, and merged images within the acoustic working region. The flow rates of the sample and the two sheath fluids were 2, 2, and 6 $\mu\text{L}/\text{min}$, respectively. (C) SEM images showing the sample before (the mixture of 1 and 6 μm particles) and after acoustic separation (collected from two outlets of the disposable microchannel).

After exploring the dependence of particle deflection on acoustic intensity and particle size, we demonstrated the separation of 1 μm and 6 μm particles in a continuous flow, as shown in Figure 4.7. Here, the diameters of 1 and 6 μm particles are approximately equivalent to that of *E. coli* and human RBCs, respectively.^{141, 190} Thus, these particle sizes will provide insight into our upcoming bacteria and RBC separation experiments. The separation performance was evaluated using the fluorescent and stacked bright-field images at the outlet region. Figure 4.7A shows the separation performance between 1 and 6 μm particles at different flow rates. The flow rate of the first sheath flow for sample focusing is the same as the sample flow rate, while the second sheath flow for sample transfer is three times the sample flow rate. For example, 2, 2, and 6 $\mu\text{L}/\text{min}$ were used for the sample, first and second sheath flows, respectively. At the same time, the acoustic intensity was optimized to maintain enough lateral displacement for 6 μm particles. Specifically, the drive voltage is 22.8 V_{PP} (29.3 dBm) at the sample flow rate of 2 and 4 $\mu\text{L}/\text{min}$, but 29.1 V_{PP} (31.4 dBm) at the sample flow rate of 6 $\mu\text{L}/\text{min}$. Overall, the deflection of 6 μm particles caused by the acoustic radiation force decreased with increasing sample flow rate. Despite this decrease, most of 6 μm particles were still driven to the upper outlet and successfully separated from 1 μm particles at the sample flow rate of 6 $\mu\text{L}/\text{min}$. Some 1 μm particles were also deflected, but this slight deflection did not push the 1 μm particles far enough, and the majority of them still exited through the bottom outlet. Figure 4.7B displays the images in the working region of the disposable

acoustofluidic device. The acoustic radiation force pushed 6 μm particles along the pressure nodes and separated them from the original mixture. Figure 4.7C provides scanning electron microscope (SEM) images of the original and separated samples. At a sample flow rate of 2 $\mu\text{L}/\text{min}$, 50 μL of each solution was collected, concentrated, and then went through SEM. In the original sample, a uniform mixture of 1 and 6 μm particles was observed. After separation, only a few 1 μm particles were found in the outlet for the separated 6 μm particle specimen, while 6 μm particles are absent in the 1 μm particles specimen, indicating an effective separation.

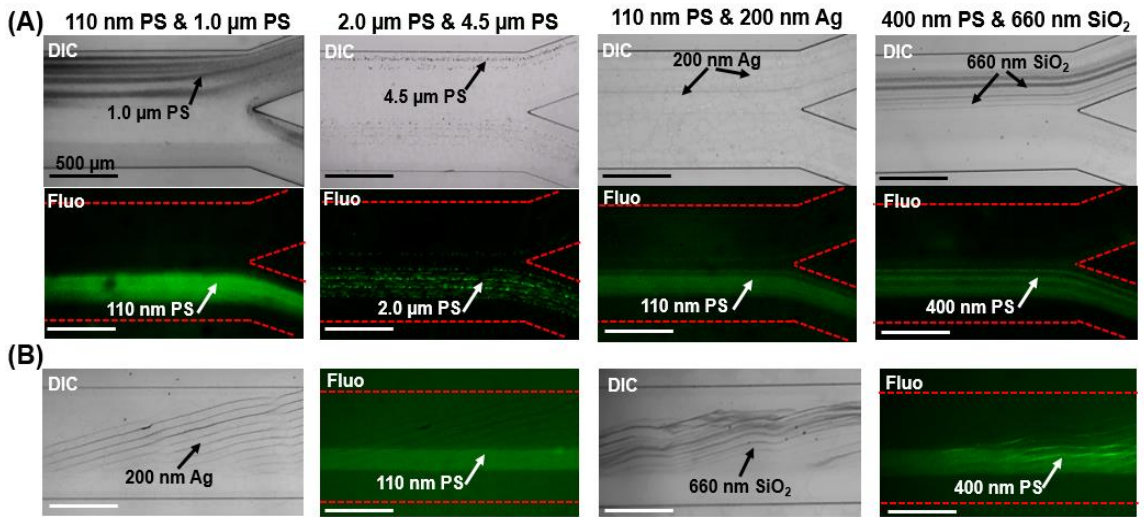


Figure 4.8: Disposable acoustofluidic chips for nano/micro particle separation in a continuous flow. (A) Bright-field and fluorescent images at the outlet region for different mixtures of dissimilarly sized particles. These combinations are shown from left to right as 110 nm and 1.0 μm PS particles, 2.0 μm and 4.5 μm PS particles, 110 nm PS particles and 200 nm Ag particles, and 400 nm PS particles and 660 nm SiO_2 particles. (B) Bright-field, fluorescent, and merged images within the acoustic working region for the separation of 110 nm PS particles from 200 nm Ag particles, and 400 nm PS particles from 660 nm SiO_2 particles.

With the disposable acoustofluidic device, separation of nano-to-micro particles with small size differences and small particle size (*i.e.*, nanoscale) also becomes feasible. We demonstrate the efficient separation of 110 nm PS and 200 nm Ag particles, 400 nm PS and 660 nm SiO₂ particles, 110 nm and 1 μm PS particles, 1 μm and 4.5 μm PS particles, 2 μm and 4.5 μm PS particles, 2 μm and 6 μm PS particles, and 6 and 10 μm PS particles. According to the influence of acoustic intensity on particle separation, the drive voltage was optimized as 35.2 V_{PP} (33.1 dBm) for 1 μm PS, 200 nm Ag, and 660 nm SiO₂ separation, but 24.9 V_{PP} (30.1 dBm) for 4.5 μm PS separation. In Fig. 8A, in different scenarios, the large particles, which were subjected to a large acoustic radiation force, have been deflected away from the small particles. Meanwhile, small particles remained in the sample stream and exited microchannel through the bottom outlet. With the disposable device, we first demonstrated the size-based PS microparticle separation, with a very small size down to 200 nm, with a very small size difference in 2 μm and 4.5 μm, and with a very small size ratio in 6 and 10 μm (Figure 4.8A). We then showed the nanoparticle separation for 110 nm PS particles and 200 nm Ag particles, 400 nm PS particles and 660 nm SiO₂ particles (Figures 4.8A and B). To achieve favorable separation performance, the flow rate of sample and two sheath fluids for nanoparticle separation was tuned to 2, 2, and 5 μL/min, respectively. The large acoustic radiation force experienced by the 200 nm Ag and 660 nm SiO₂ nanoparticles, resulting from their significantly larger acoustic

contrast factor relative to PS particles (φ is 0.437 for PS, 2.295 for Ag and 1.786 for SiO₂),¹⁹¹ pushes Ag and SiO₂ particles.

4.3.4. Disposable Acoustofluidic Chips for Bacteria Separation

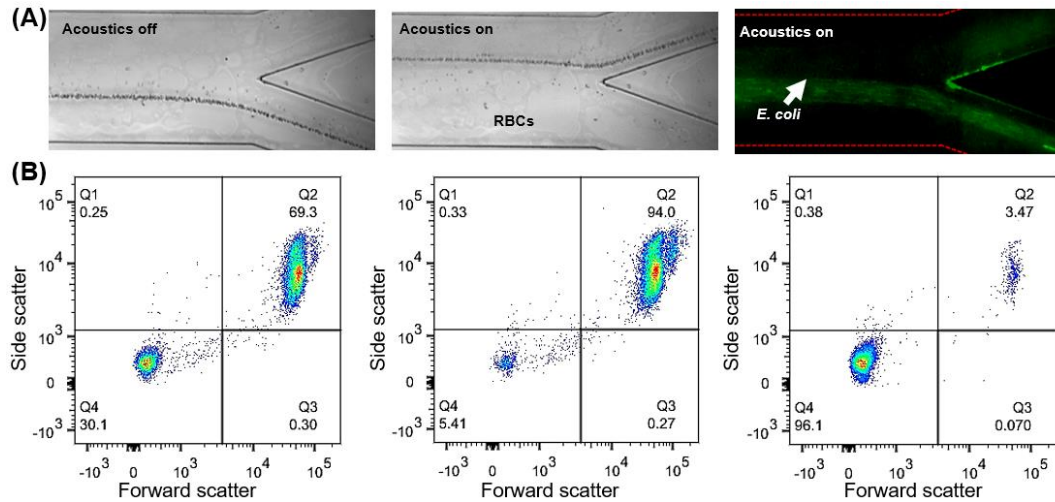


Figure 4.9: Disposable acoustofluidic chips for bacteria separation. (A) Bright-field and fluorescent images for bacteria separation *via* the disposable acoustofluidic chip. (B) Flow cytometry results of the *E. coli* and RBCs mixture, the separated *E. coli*, and the separated RBCs.

To further demonstrate its capability for purification of biological samples, our disposable acoustofluidic chips were used to separate *E. coli* bacteria from human RBCs in phosphate buffered saline (PBS). The capability of separating bacteria from human blood cells would promise rapid diagnosis in blood related diseases such as sepsis.^{141, 143,}
¹⁹⁰ In order to observe the *E. coli* bacteria clearly, they were stained with a live/dead BacLight kit (L7007, Invitrogen, USA).¹⁹² Accordingly, images of the live bacteria with green fluorescence were recorded. Fig. 6A shows the bright-field and fluorescence images for RBCs and *E. coli*, respectively. When exposed to the taSSAW field at 25.6 V_{PP} (30.3

dBm), the majority of the RBCs were pushed away from the bottom outlet to the upper outlet. Specifically, an acoustics on-off-on process was recorded to show the movement trajectories of RBCs. In comparison, even with the acoustic signal on, *E. coli* continued to exit the channel through the sample stream (right image in Figure 4.9A), demonstrating an excellent separation from RBCs. We further characterized the performance of bacteria separation using a flow cytometer. Figure 4.9B shows the flow cytometry results of the original mixture, the separated *E. coli*, and the separated RBCs. In the plot of forward scatter (FSC) and side scatter (SSC) (Fig. 9B), *E. coli* and RBCs populations can be distinguished easily due to their large size difference. For the original sample, the ratios of RBCs and *E. coli* to the total number of cells were 69.3% and 30.1%, respectively. After separation, this ratio for the RBCs increased to 94.0% in the top outlet collection, while it increased to 96.1% for *E. coli* in the bottom outlet collection. The viability of bacteria was also measured as 99.8% before SAW separation and 97.5% after SAW separation, showing good biocompatibility of our disposable acoustofluidic devices. In previous research, Ai. et al. separated peripheral blood mononuclear cells (PBMCs) from *E. coli* with a purity of 95.65% using a permanently bonded SAW device, where the concentration of *E. coli* and PBMCs were both approximately 3×10^6 particles/mL.¹⁷⁰ These results indicate that our disposable acoustofluidic device can achieve comparable cell/bacteria separation performance relative to the permanently bonded SAW devices, validating its potential for future real-world applications.

4.4. Conclusions

In this work, we developed a disposable acoustofluidic platform by assembling a disposable microchannel onto a reusable piezoelectric substrate coated with IDTs. A pair of unidirectionally distributed IDTs was designed to generate a strong taSSAW field. To improve acoustic energy transmission, a hybrid hard/soft PDMS channel design was employed, in which a hard PDMS film with a thin thickness and a low acoustic attenuation factor was used as the microchannel bottom enclosure. We then demonstrated a strong taSSAW acoustic field within disposable microchannels by concentrating 400 nm PS particles along tilted-angle pressure nodes. Particle velocity measurements also reveal that the intensity of acoustic radiation force achieved in our disposable acoustofluidic chips is comparable to that in devices with permanently bonded channels. The ability to distinguish the deflection distances of four different sized particles indicates the favorable controllability and sensitivity of our disposable devices.

For particle separation, our unidirectional IDT-based disposable acoustofluidic chips can separate nano-to-micro particles, and also differentiate bacteria from human RBCs. We demonstrated that particles with a wide size range from 200 nm to 10 μm can be separated. For example, the separation of 2 and 4.5 μm PS particles with relatively small size difference indicates the accuracy and sensitivity of our disposable devices. And the separation of 200 nm Ag particles from 110 nm PS particles and 660 nm SiO_2 particles from 400 nm PS particles suggest the capability of our disposable device for nanoparticle

separation. Additionally, an efficiency up to 96% was achieved for bacteria and human RBCs separation. With its features of being biocompatible, label-free, efficient, versatile, and cost-effective, this technology would significantly expedite the implementation of acoustic separation systems into practical biomedical and clinical applications, such as cell phenotyping, sample purification, cell and bacteria separation.

5. Topological Acoustofluidics

Topological wave materials offer thriving possibilities for unconventional wave-matter interactions in the fields of photonics, acoustics, and elastodynamics. However, topological phenomena are mainly limited to one single medium and the potential of topological materials that support multi-physics coupling remains unexplored. Here, we realize valley-hall topological insulators at the interface of a phononic platform that supports surface acoustic waves and a fluidic layer, referred to as topological acoustofluidics. The multi-physics effect is manifested by experimentally observed chiral vortices in water fluids analogous to the valley vortex fields in wave dynamics by tracking fluorescent tracer nanoparticles, which are facilitated by the energy transport from the solid domain to the liquid domain. Topologically protected edge states are constructed along a Z-shaped interface in fluids that can generate topological pressure well to reversibly manipulate pseudo-biological polystyrene particles. A ring resonator is further demonstrated on an anisotropic substrate which exhibits a new degree of freedom to topological materials. These results demonstrate the rich physics and promote the study of topological materials across multiple physical interfaces, and open doors towards the application of topological insulators in life sciences.

5.1. Motivation

Topological insulators are materials that behave as insulators in the bulk but support backscattering-immune conduction for electrons on their surface.²⁸ Originating

from condensed-matter physics, their studies have recently expanded to the realm of phonons and photons, overturning some of the traditional views on wave propagation. For example, unidirectional wave transport,¹⁹³ negative refraction,²⁸ and non-Hermitian acoustics¹⁹⁴ have been realized using sonic crystals in air. Thanks to the advancement of modern microfabrication technologies, topological insulators have recently been realized on solid-state photonic²⁸ and phononic on-chip platforms²⁴. This chip-scale renovation is pushing the surging topological physics to real-world applications, such as terahertz photonic communication,¹⁹⁵ topological photonic laser¹⁹⁶ and phononic beam splitter.²⁴ Despite its great success in solid and airborne systems, the demonstration of topological states in liquids is scarce.

Liquids that are similar to solids and gases constitute another fundamental medium of wave propagation and are essential in life sciences. Vortex states, one prominent feature in topological wave phenomena, have been difficult to measure in solid or air medium.^{197, 198} A liquid medium, however, offers unique advantages for the direct visualization of topological spin textures by decorating tracer particles. For example, topological valley vortex state, topological skyrmion, meron, and anti-meron state may map to unique streaming patterns. Similar visualization technique has been developed in superfluid for observation of quantum turbulence and vortices, but is absent in topological photonics and phononics. Besides, the unusual states in topological matter could provide exotic possibilities for robust manipulation and transport of biological

samples in life sciences. For example, the valley vortex state can be applied to clockwise or counterclockwise biological particle rotation in a synchronous direction. The back-scattering immune edge state could enable back-movement immune transport of biological samples and novel ring resonator for viral biosensing. While topological transport of water waves was realized in a time-reversal symmetry-broken system,¹⁹⁹ the active-liquid and large-scale dimension limit the system for practical applications. Up to now, the direct realization of topological fluid phenomena on a single chip, that is, microfluidics is extremely difficult and has not been reported due to fabrication difficulties and the complexity of the multiphysics nature of the system. Specifically, the coupling effect between the solid substrate and the fluid adds to the complexity of both numerical modeling and experimental demonstration.

Another difficulty in implementing on-chip topological waves for life science is that the on-chip substrate is typically anisotropic. This anisotropy alters the edge states of the system and makes edge state bandwidth dependent on wave propagating directions. Recently, an unusual anisotropy of topological edge mode for superconductivity has been revealed in natural occurring materials.^{200, 201} This anisotropy is crucial because edge state bandwidth changes with its orientation relative to the substrate and because edge states in different orientations are required in beam splitter and ring resonator. Additionally, the orientation angle can serve as a new degree of freedom to tune topological wave

propagation. However, the realization of angle-dependent topological edge states on an artificial platform remains unexplored.

Here, we propose the concept of an on-chip, passive-liquid topological valley hall insulator for surface acoustics waves (SAWs) in solid and fluid domains, defined as topological acoustofluidics. The main idea is to utilize lithium niobate-based valley phononic crystals (VPCs) and microfluidics to provide a chip-scale platform for topological phenomena investigation in multiphysics systems and particle manipulation in life sciences. Topological phenomena are realized in the substrate and the fluid domain by coupling effect and energy transport. Remarkably, we experimentally observed chiral vortex streaming along the topological interface, which allows back-movement immune transport of nanoparticles, analogous to the back-scattering immune wave transport. Different from the solid domain or the air domain, the topologically protected edge states are also able to generate topological pressure wells for reversible particle manipulation localized in unit cell dimension. Moreover, we found that the bandwidth of edge states depends strongly on the anisotropy of the lithium niobate substrate, which translates to the orientation angle of the topological interface. Leveraging this angle-dependent topological state, we constructed a ring resonator for potential biosensor applications. These results suggest rich physics stemming from the energy transport and coupling effects across different physical systems. It is hoped that the work will promote

topological materials in multiple physical systems and open new routes for the application of topological matter in life sciences.

5.2. Methods

5.2.1. Sample Fabrication

The fabrication process begins with excitation interdigital transducers (IDTs) pattern transfer by photolithography onto the piezoelectric lithium niobate (LiNbO_3) wafer, followed by metal (Cr/Au 5/150 nm) deposition by an electron-beam evaporator. After a lift-off process in acetone, a metal (Ti/Cu 10/200nm) seed layer is deposited on LiNbO_3 wafer by a second electron-beam evaporator. The phononic structure patterns were transferred on the LiNbO_3 wafer by photolithography and development of a AZ9260 photoresist in a AZ400K 1:4 developer. With 30 μm AZ9260 photoresist as a mask, the phononic crystals of copper pillars were electroplated on the LiNbO_3 wafer. Then, acetone, APS-100 copper etchant and buffered oxide etchant solution were sequentially used to remove the photoresist and copper seed layer between phononic structures. Finally, a PDMS microchamber with punched holes for fluid injection was bonded on the device chip for characterization.

5.2.2. Experimental Measurement

The fabricated topological acoustofluidic devices were characterized by tracking fluorescent polystyrene particles in the water layer. Before fluorescent particle solution loading, we injected a 5% Pluronic F-127 (Sigma-Aldrich) solution into PDMS

microchamber and maintained the solution for 10 mins to avoid particle adhesion on copper pillars. Once mounted on a microscope stage, the devices were driven by a continuous sinusoidal signal sweeping from 22-26 MHz generated by a functional generator (E4422B, Agilent, USA) and magnified by an amplifier (25A250A, Amplifier Research, USA). The chiral vortex streaming was monitored with an inverted fluorescent microscope (Eclipse Ti, Nikon, Japan) and the particle concentration was recorded with an upright fluorescent microscope (BX51W1, Olympus, Japan). For transmission measurements, a gaussian pulse was generated by a function generator (AFG3011, Tektronix, USA) and magnified by the amplifier before being sent to the excitation IDTs, while the transmitted signal was received by output IDTs and measured by an oscilloscope (Tektronix, DPO3034). The experimentally measured spectra are normalized to acoustic wave transmission in fluids at the same distance.

5.2.3. Numerical Simulation

All full-wave simulations were carried out through a commercial finite-element solver (COMSOL Multiphysics 6.0). In band structure and band diagram calculations, an eigenfrequency study was conducted with Floquet periodic boundaries. In intensity, pressure and velocity fields calculations, the frequency domain study was performed with the low-reflection boundary imposed on the outer boundaries. The top layer of water fluid is modeled by a soft boundary, considering the in-plane vibration of copper pillars. And, the 'piezoelectric effect multiphysics' is applied to couple the solid mechanics module and

electrostatics module; ‘acoustic-structure multiphysics’ is applied to couple the solid mechanics module and pressure acoustics module; laminar flow module is applied to calculate fluid flow pressure and velocity. For material properties, the anisotropic LiNbO₃ are $c_{11} = 202$ Gpa, $c_{22} = 193$ GPa, $c_{33} = 221$ GPa, $c_{44} = 75.3$ GPa, $c_{55} = 56.8$ GPa, $c_{56} = c_{65} = -5.9$ Gpa, $c_{66} = (c_{11} - c_{12})/2 = 77.9$ Gpa. The properties of electroplated copper pillars are density 8,960 kg m⁻³, Poisson ratio 0.34, Young’s modulus 95 GPa determined by nanoindentation (Bruker Hysitron TI980 Triboindenter), height 28 μm measured by 3D optical profiler (Zygo NewView 5000).

5.3. Results and Discussion

5.3.1. Design of On-Chip Topological Acoustofluidic Device

Figure 5.1a displays a schematic of our topological acoustofluidic device. In our implementation, the SAWs on the lithium niobate chip, known as Rayleigh waves, are periodically modulated by copper-based VPCs in the water domain, leading to band-like valley states. The copper pillars are electroplated in a hexagonal lattice (Figure 5.1b) and can transport valley state energy from solid VPC domain to liquid water domain. As shown in the unit cell of Figure 5.1c, when the small pillar vibrates vertically, the large pillar transfers its gyro rotation energy to vortex energy in the fluid domain by solid-fluid coupling effect. The topologically protected phononic edge state therefore can be constructed in water at the interface between inverted valley hall phases VPC1 and VPC2.

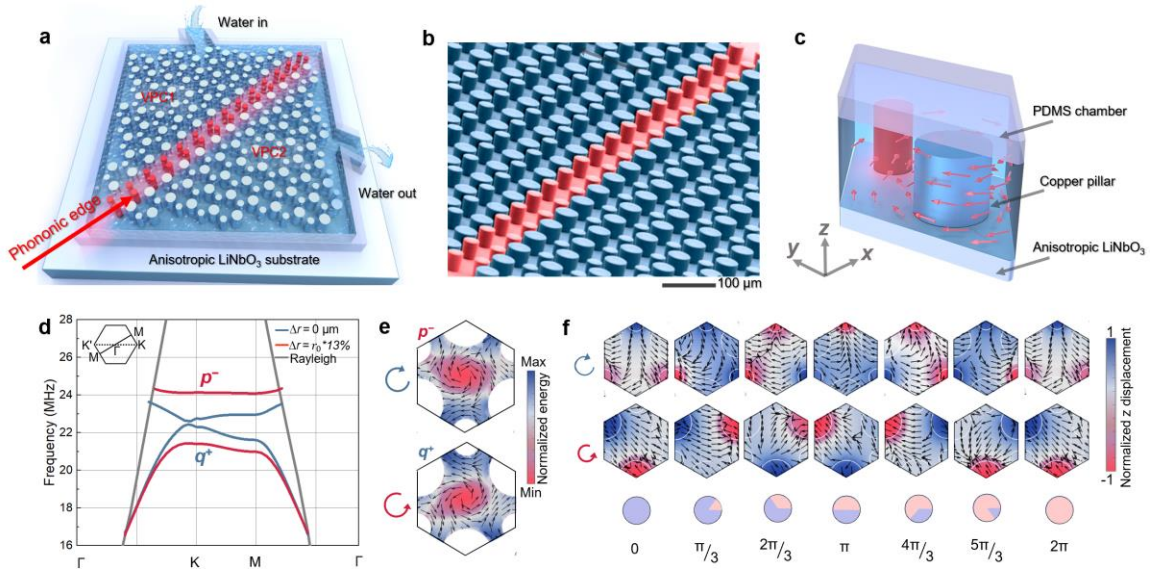


Figure 5.1: Design of a topological acoustofluidic chip with valley state modes.

a, schematic of the proposed topological acoustofluidic device on a 128° Y-cut X-propagation lithium niobate wafer, where VPCs in water fluids are bonded with a PDMS microchamber. b, SEM image of the electroplated copper pillars in a hexagonal lattice with lattice constant $a=72\ \mu\text{m}$. c, schematic of a valley mode in one unit cell with two dissimilar copper pillars surrounded by water fluids. The diameters for large and small pillar are d_L and d_S , respectively, while the height for the copper pillar and water fluid is h_C and h_W , respectively. The red color scale and red arrows represent z -oriented displacement of small pillar and valley vortex around large pillar, respectively. d, Band structure of the water layer integrated VPC on lithium niobate for SAWs. The red and blue lines represent dispersions without and with inversion symmetry, and the grey lines denote the sound line of SAW in water fluids. e, Simulated mode profiles at the first band (q^+) and second band (p^-) of the K valley in d. The color scale denotes z -oriented energy field, while black arrows show the Poynting energy flow. f, Time evolution of simulated displacement field and Poynting energy flow of q^+ and p^- valley states.

The parameters of the unit cell, that is, pillar sizes d_L and d_S , pillar height h_C , and water height h_W are rationally designed to ensure that: (1) a large bandgap is opened to achieve narrow edge-state confinement by enlarging sublattice asymmetry; (2) well-defined non-trivial berry curvature by reducing sublattice asymmetry; and (3) the fluid height h_W , is

not too small so that the valley state energy can be transferred successfully from solid domain to liquid domain.

Figure 5.1d shows the band structure before and after breaking the spatial inversion symmetry of the system. When $d_L=d_S=0.4a$, the VPC preserves C_6 symmetry and features Dirac cones in the momentum space (K and K' valley). When $d_L \neq d_S$, the inversion symmetry is broken to C_3 symmetry, and a band gap is opened from 21.5 MHz to 24.5 MHz near the Dirac frequency. To reveal the features of valley states in water fluids on a solid chip, we investigated the eigenstates at the first (p) and second band (q^+) of K valley, as depicted in Figure 5.1e. In contrast to the gyro rotation in the solid domain,²⁴ the valley states in solid/liquid domain carry anticlockwise and anticlockwise vortex convoluting around Gamma point in the lattice. Clearly, p state carries a clockwise energy flux, while q^+ state carries an anticlockwise energy flux. In Figure 5.1f, this opposite chirality is further illustrated by six sequential instants of q^+ and p valley states at a phase step of 60° . Not only the energy flux but also the pillar displacement moves in opposite directions as a periodic function of time from $t=0$ to $t=2\pi/\omega$. The feature at K' valley is then straightforwardly predicted by time-reversal symmetry.

5.3.2. Experimental Visualization of Chiral Vortex Streaming at Valley Projected Edge State

Next, as shown in Figure 5.2, we construct a kink type straight interface by combing two VPCs with opposite phases. At the same band, the opposite chirality at K and K' valley is ascribed to the inversed pillar size difference ($\Delta d = d_L - d_S$), as displayed by

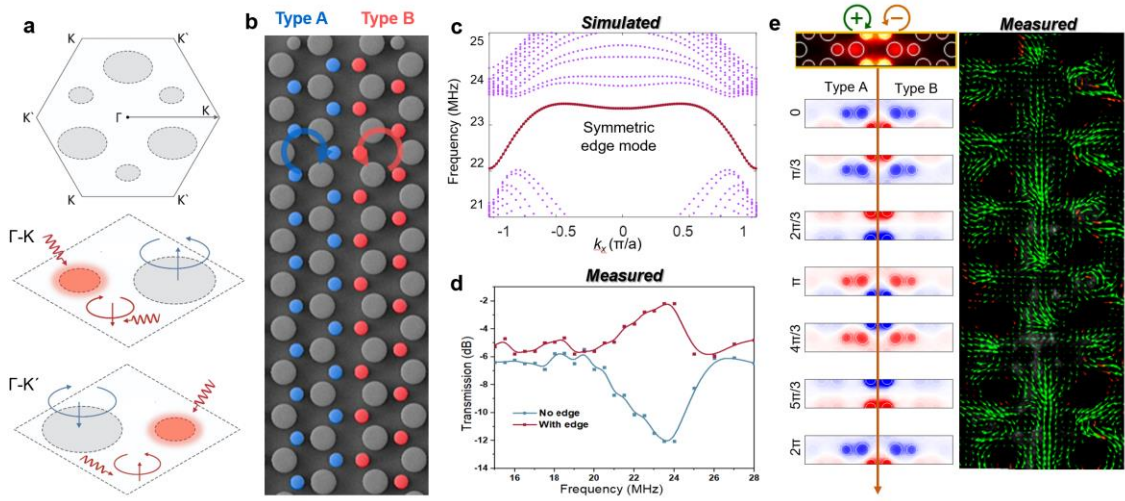


Figure 5.2: Experimental characterization of chiral vortex streaming feature of edge state in fluids. a, schematic of the proposed topological acoustofluidic device on a 128° Y-cut X-propagation lithium niobate wafer, where VPCs in water fluids are bonded with a PDMS microchamber. b, SEM image of the electroplated copper pillars in a hexagonal lattice with lattice constant $a=72 \mu\text{m}$. c, schematic of a valley mode in one unit cell with two dissimilar copper pillars surrounded by water fluids. The diameters for large and small pillar are d_L and d_S , respectively, while the height for the copper pillar and water fluid is h_C and h_W , respectively. The red color scale and red arrows represent z-oriented displacement of small pillar and valley vortex around large pillar, respectively. d, Band structure of the water layer integrated VPC on lithium niobate for SAWs. The red and blue lines represent dispersions without and with inversion symmetry, and the grey lines denote the sound line of SAW in water fluids. e, Simulated mode profiles at the first band (q+) and second band (p-) of the K valley in d. The color scale denotes z-oriented energy field, while black arrows show the Poynting energy flow. f, Time evolution of simulated displacement field and Poynting energy flow of q+ and p- valley states. the hexagonal structure of pillars in real space and valley points in momentum space (top in Figure 5.2a). Therefore, two VPCs with opposite phases can appear at K valley: VPC1 of clockwise feature with $\Delta d = d_L - d_S$ (middle) and VPC2 of anticlockwise feature with $-\Delta d = d_L - d_S$ (bottom). Figure 5.2b shows the fabricated interface between VPC1 and VPC2 with opposite Δd on each side. Based on the bulk-edge correspondence, a pair of valley-

projected edge states appear at the interface: one at K valley propagates forward, and the other at K valley propagates backward.²⁰² This prediction is consistent with the simulations in Figure 5.2c. In Figure 5.2c, the dispersion of the valley kink state denoted by the solid and dashed red lines represent edge states projected from the K and K' valleys, respectively. For a certain wavevector, there is only one edge state within the bandgap due to their opposite group velocity.

We then experimentally measure the acoustic transmission in VPCs with a straight interface or no interface to verify the existence of edge states in solid/liquid domains. In Figure 5.2d, an evident dip in transmission, from 22 MHz to 25 MHz, is shown in a VPC without an interface. In contrast, for VPC with a straight interface, the transmission almost reaches unity. This clear difference indicates that the valley projected edge state can propagate along the interface in the water domain. One of the most important features of topological edge states is the chiral vortex along the interface. Figure 5.2e shows the simulated chiral vortex feature of acoustic pressure fields along the straight interface in fluids. Different from a solid or air domain, the fluid domain enables the visualization of these spin textures by tracking the trajectories of fluorescent particles. Figure 5.2f experimentally confirmed this chiral vortex by the clockwise and counterclockwise vortex streaming of 200 nm PS particles in fluids along the straight interface. Data is processed from video through a PIV program in MATLAB. For valley edge state coupled from the solid domain to the liquid domain, the valley edge state of SAWs first induces gyro-rotate

5.3.3. Topological Pressure Wells at Edge-State Pathways for Reversible Particle Manipulation

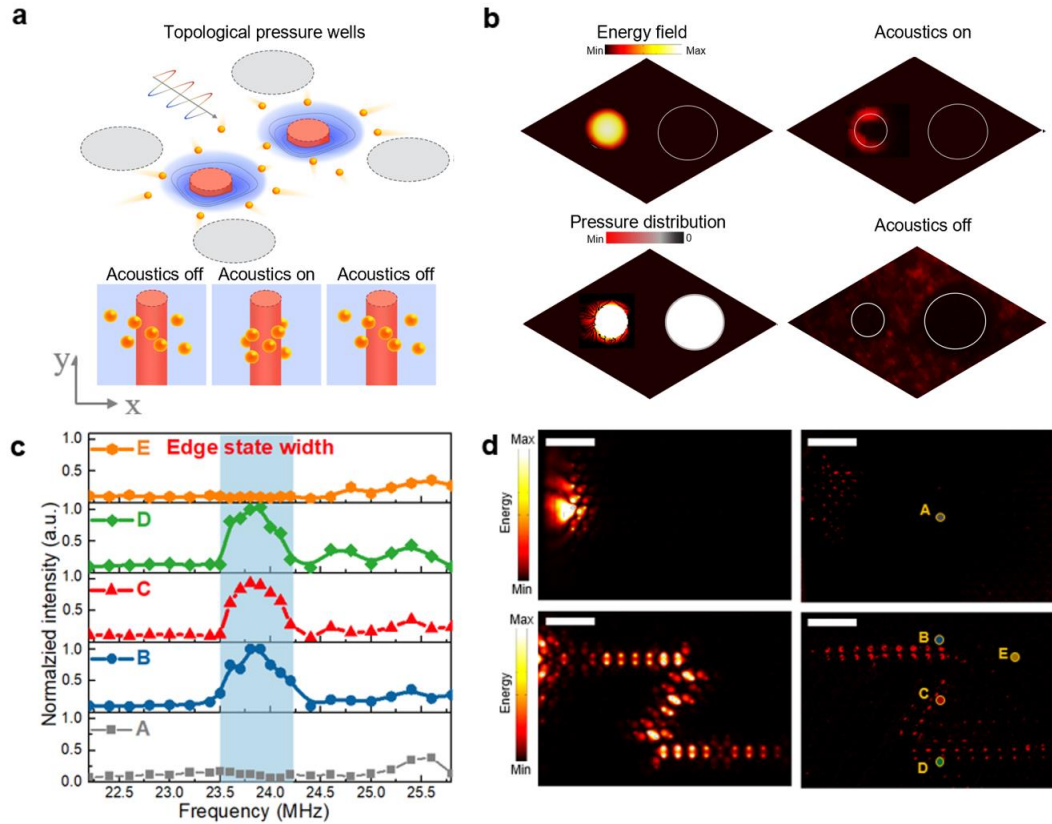


Figure 5.3: Experimental demonstration of robust edge states for reversible particle manipulation in an acoustofluidic chip. a, Schematic of topological fluid pressure wells around domain interface for reversible particle manipulation. The red color and blue color represent energy field and fluid pressure field, respectively. b, Simulated energy field and fluid pressure field in unit cell dimension around domain interface (top). Measured fluorescent intensity distribution of fluorescent particles around domain interface with acoustics on and off (bottom). c, Measured fluorescent intensity spectra at positions far from (point A), near (points B, C, and D) and without (point E) domain interface in d. The blue region represents the frequency range of the edge state. d, Simulated energy field and measured fluorescent intensity distribution for VPCs with a Z-shaped interface and no interface at the frequency of 23.85 MHz, respectively.

of large copper pillars, and this rotation is transferred to fluids in the form of vortices surrounding large pillars. Then, three large pillars work together to generate anti-vortices convoluting around the hexagonal structure center. Moreover, the back-movement immune transport of the nanoparticles is consistent with the backscattering-immune wave propagation. These results prove the valley edge states in fluids and provide a technology to visualize topological spin textures.

In solid or air domain, the chiral vortex feature appears at the Gamma point of the lattice. In contrast, in solid/fluid domain, there exist topological pressure wells surrounding small pillars in unit cell dimension. This phenomenon appears when the height of the water fluid is close to that of copper pillars. To verify robust topological pressure wells, we fabricated a sample by integrating VPC1 and VPC2 with a Z-shaped interface in the water domain for particle manipulation. Figure 5.3a shows a schematic for topological pressure wells to reversibly manipulate particles. With SAWs on, particles are concentrated on small pillars; with SAWs off, particles are released from small pillars. Figure 5.3b shows that the simulated pressure well matches well with movement of particles in unit cell at domain interface. In the top panel, the simulated maximum energy field is on solid-state small pillar, while the minimum pressure field is near small pillar. In the bottom panel, the measured experiments show the concentration of 1 μm PS particles on small pillars with SAWs on, and the release of those particles with SAWs off. This reversible particle manipulation is driven by acoustic radiation force, which pushes

PS particles to pressure minimum region. This remarkable feature unveils the unique topological phenomena in a multiphysics coupled system and could find potential applications in localized biological sample manipulation.

On the other hand, another prominent feature of the valley projected edge state is their robustness to sharp corners due to the absence of inter-valley scattering. To characterize the robust propagation of valley edge states, we measured the fluorescent spectra at selected spots far from (point A), near (points B, C, and D) and without (point E) Z-shaped interface, as shown in Figure 5.3c. The measured intensity at points B-D is much higher than that at points A and E in the edge state frequency range of 23.4 MHz-24.2 MHz. Note that, beyond this range, the fluorescent intensity distribution at different points becomes complex and indicates a random behavior, due to the reflection and refraction of SAWs within VPCs and at the domain interface. Figure 5.3d displays simulated energy field and measured fluorescent intensity at the frequency of 23.85 MHz. Being in good agreement with simulation, the measured intensity is well distributed along a Z-shaped interface, in striking contrast to the rapid annihilation when the interface is absent. These results confirm the robustness of topological edge states in liquid domain coupled from solid state edge states and enable reversible particle manipulation localized in one unit cell.

5.3.4. Topological Acoustofluidic Mapping of the Anisotropic Edge States on Lithium Niobate

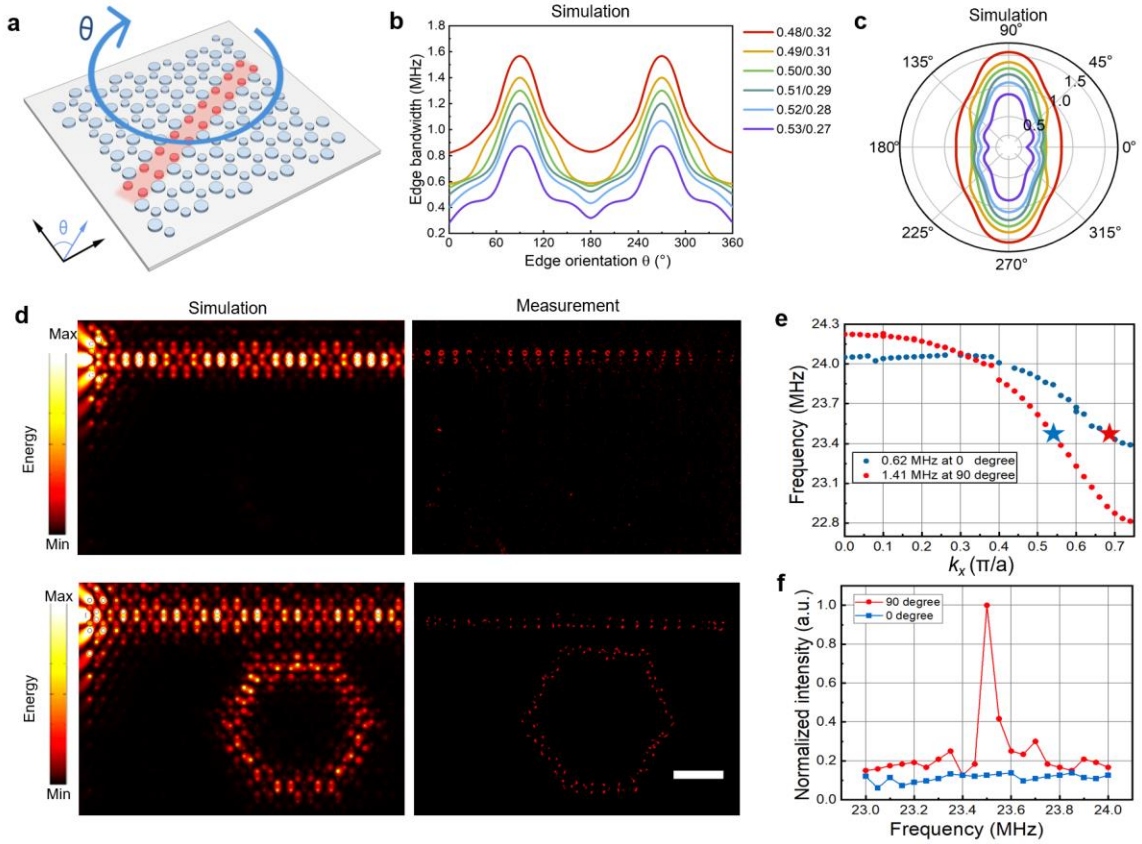


Figure 5.4: Topological acoustofluidic mapping of the anisotropic edge states on an anisotropic lithium niobate chip. a, Schematic for the rotation angle θ between the domain interface and x-axis of lithium niobate chip. b and c, Plot of simulated bandwidth of edge state bandwidth relative to θ , showing a two-mode symmetric anisotropy. (r_a/r_b =radius ratio of large pillar and small pillar). The largest bandwidth of 1.5 MHz appears at 90° for 0.48/0.32. d, Simulated energy field and measured acoustofluidic fluorescent mapping of the waveguide-ring resonator at 23.4 MHz for 0° and 90° . e, Simulated edge state lines at 0.48/0.32 with rotation angles 0° and 90° , respectively. The red and blue stars at 23.4 MHz represent the resonance frequency of the waveguide-ring resonator. f Measured fluorescent intensity spectra for the simulated waveguide and ring resonator at 23.4 MHz for 0° and 90° .

In Figure 5.4a, an anisotropic edge state occurs when the topological domain interface rotates at an angle of θ to the x-axis of lithium niobate chip. Without anisotropic

property of substrate, the edge state with the same lattice parameters is isotropic as a function of rotation angle. Figures 5.4b and c show the plot of the simulated edge state bandwidth relative to θ . With decreasing asymmetry between dissimilar pillars, the bandwidth decreases and gives rises to the maximum value at 90° and 270° , suggesting a two-mode symmetric anisotropy.

Leveraging this anisotropic edge mode, we constructed a waveguide-ring resonator, as shown in Figure 5.4d. The waveguide-ring resonator consists of two interfaces: one straight interface for waveguide with two ports on top, and one closed hexagonal ring on the bottom, *i.e.*, the ring resonator. Once excited by SAWs, the valley-momentum locking limits the pseudospin in solid-state copper pillars to the two spin-preserving scattering channels due to the backscattering-immune transport. These two channels include the forward channel in the straight interface and the counterclockwise circulation channel in the hexagonal loop, respectively. At 90° , there is energy and fluorescent field in the ring resonator, but these fields are absent for 0° . This can be understood by examining the simulated band diagram and fluorescent spectra in Figures 5.4e and f. The resonance frequency of the ring resonator is 23.4 MHz and located in the middle of 90° waveguide spectra, while it is almost at the periphery of 0° waveguide spectra. Our studies here clearly demonstrate the advantage of anisotropic edge state that is readily realized from a realistic anisotropic substrate. It thus could be utilized directly

in a broad range of topological material designs, where the anisotropy can provide a new degree of freedom.

5.4. Conclusions

In conclusion, we have used the solid-liquid coupling between water domain and copper phononic crystals to realize topological phenomena on microfluidic platform. Based on this approach, we experimentally visualize the chiral vortex streaming and backscattering-immune transport of topological edge states by tracking fluorescent particles in water fluids. Distinct features arising from a coupled multiphysics system are observed that are absent in single domains such as solid or air, namely the topological pressure wells in unit cell dimension adjacent to the domain interface. Localized reversible particle manipulation are further demonstrated by leveraging this peculiar effect. Furthermore, we found the existence of anisotropic edge state on lithium niobate, which provides new degrees of freedom for topological material design on realistic on-chip substrate. The work demonstrates the feasibility of topological states sustained by a multi-physics system and more importantly, opens the door for topological phenomena across different physical interfaces. The work provides a new technology for visualization and a deep understanding of topological spin textures, analogous to that in quantum fluids. The work also bridges topological insulators to life sciences for synchronous particle rotation, one-way particle transport, localized particle manipulation, and biosensing.

6. Conclusion

This dissertation presents an investigation into micro-vortex streaming in acoustofluidic devices, from the perspectives of enhancement, suppression, and chirality. Each opens the door for new possibilities in particle and biological sample manipulation. However, certain challenges remain as well as numerous opportunities. In this section, I will first summarize our contributions to the development of acoustic micro-vortex streaming. I will then provide my perspective on the next generation of micro-vortex streaming based acoustofluidic devices and discuss future research directions for the emerging topological acoustofluidic field.

6.1. Summary

The investigation of acoustic micro-vortex streaming in this dissertation is divided into aspects for (1) enhancing streaming; (2) suppressing streaming; and (3) generating chiral streaming.

Enhancement of micro-vortex streaming was studied in chapters 2 and 3. Through rational design and a systematic investigation of device parameters, we have demonstrated that device operation frequency, glass thickness, and PDMS thickness play key roles in enhancing micro-vortex streaming to improve mixing performance. With optimal design parameters, the sharp-edge based micromixer was able to reduce mixing time from 180 ms to 3 ms, allowing for improved throughput from 5 $\mu\text{L min}^{-1}$ to 150 $\mu\text{L min}^{-1}$. This rapid and strong micro-vortex streaming enabled on-chip liquefaction of

viscous human stool samples while maintaining the bacteria viability. Moreover, we also demonstrated that micro-vortex streaming in microfluidic channels could also be used to facilitate nanoparticle synthesis. We fabricated nanoparticles that are difficult to generate in hydrodynamic methods including (1) uniform PLGA-PEG nanoparticles; (2) chitosan nanoparticles via multiple reagents reaction; (3) PLGA-lipid core shell nanoparticles via sequential reagent mixing.

Suppression of micro-vortex streaming in SAW devices was studied in chapter 4. Although acoustic radiation force and acoustic streaming compete to manipulate particles, acoustic radiation force is more predictable and is more preferred. To this end, we developed disposable SAW devices for particle manipulation by generating SSAW to reduce acoustic streaming and designing unidirectional transducers to enhance acoustic radiation force. The results showed that the S21 transmission is tremendously increased from -11.2 dBm in bidirectional transducers to -5 dBm in unidirectional transducers. By minimizing acoustic streaming and enhancing acoustic radiation force, we showed comparable performance for particle manipulation compared to directly bonded SAW devices. Our disposable SAW devices were able to not only concentrate 400 nm PS particles at pressure nodes, but also separate bacteria from human blood cells in the absence of acoustic streaming. This work demonstrates an effective method to suppress acoustic streaming by enhancing acoustic radiation force. Furthermore, the low-cost of the

device could significantly expedite the transition of disposable SAW devices into point-of-care systems.

The generation of chiral micro-vortex streaming in SAW based topological acoustofluidic devices was studied in chapter 5. We introduced the physics of valley hall topological insulators into microfluidics and demonstrated the two fields can contribute to each other. Based on the numerical simulation of chiral vortex streaming in fluids, we experimentally realized clockwise and counterclockwise micro-vortex streaming of 200 nm PS particles along the interface between two topologically inequivalent hexagonal phononic crystals. We also demonstrated reversible particle manipulation in unit cell structures along a topological zigzag interface. Using this reversible particle manipulation, we further showed that the anisotropic property of lithium niobate has a significant effect on the bandwidth of edge states. For the acoustofluidic field, topological physics provide new possibilities for particle manipulation, such as clockwise/counterclockwise particle rotation, back-movement immune particle transport, and highly localized particle concentration. For topological insulator field, microfluidics provides a visualization technology by which to characterize topological spin textures. This work also extends topological physics from one single physical domain to two physical domains (solid and liquid). Overall, our work at the interface of acoustofluidics and topological physics can serve to expand both fields.

6.2. Potential Future Work

The potential future work for acoustic micro-vortex streaming in this dissertation is discussed in aspects for (1) numerical model for bulk acoustic wave devices, (2) studies in topological spin textures and (3) applications of topological acoustofluidic devices.

For sharp edge based flexural acoustic wave devices, the current simulation model uses pressure acoustics and fluid mechanics to simulate fluid mixing and micro-vortex streaming. However, the vibration displacement of sharp edge is directly measured from experiments, which cannot predict the influence of the significant parameters such as substrate and PDMS microchamber thickness. Therefore, introducing solid mechanics with band structure theory to directly predict the device performance would be extremely meaningful both in theory and experiments.

Acoustic waves have been considered as a scalar field for the long time until the recent demonstration of topological spin textures such as chiral vortex and skyrmion. Limited to solid or air domain, these spin textures are difficult to observe. The emergence of our topological acoustofluidic technology provides possibilities for visualization and deep understanding of these spin textures by tracking the trajectories of fluorescent particles.

The surge in physics of topological insulators have tremendously overturn the traditional view of wave propagation. However, the real-world applications of these concepts are limited. The convergence of these new physics concept into microfluidics for

life sciences would provide new possibilities that cannot be achieved by traditional microfluidic devices, such as synchronous cell rotation and one-way cell transport.

References

- (1) Reynolds, O. XXIX. An experimental investigation of the circumstances which determine whether the motion of water shall be direct or sinuous, and of the law of resistance in parallel channels. *Philosophical Transactions of the Royal society of London* **1883**, (174), 935-982.
- (2) Shamloo, A.; Boodaghi, M. Design and simulation of a microfluidic device for acoustic cell separation. *Ultrasonics* **2018**, *84*, 234-243.
- (3) Lu, M.; Ozcelik, A.; Grigsby, C. L.; Zhao, Y.; Guo, F.; Leong, K. W.; Huang, T. J. Microfluidic hydrodynamic focusing for synthesis of nanomaterials. *Nano Today* **2016**, *11* (6), 778-792.
- (4) Lee, C.-Y.; Chang, C.-L.; Wang, Y.-N.; Fu, L.-M. Microfluidic mixing: a review. *International journal of molecular sciences* **2011**, *12* (5), 3263-3287.
- (5) Karnik, R.; Gu, F.; Basto, P.; Cannizzaro, C.; Dean, L.; Kyei-Manu, W.; Langer, R.; Farokhzad, O. C. Microfluidic platform for controlled synthesis of polymeric nanoparticles. *Nano letters* **2008**, *8* (9), 2906-2912.
- (6) Valencia, P. M.; Basto, P. A.; Zhang, L.; Rhee, M.; Langer, R.; Farokhzad, O. C.; Karnik, R. Single-step assembly of homogenous lipid- polymeric and lipid- quantum dot nanoparticles enabled by microfluidic rapid mixing. *ACS nano* **2010**, *4* (3), 1671-1679.
- (7) Rhee, M.; Valencia, P. M.; Rodriguez, M. I.; Langer, R.; Farokhzad, O. C.; Karnik, R. Synthesis of size-tunable polymeric nanoparticles enabled by 3D hydrodynamic flow focusing in single-layer microchannels. *Advanced Materials* **2011**, *23* (12), H79-H83.
- (8) Sajeesh, P.; Sen, A. K. Particle separation and sorting in microfluidic devices: a review. *Microfluidics and nanofluidics* **2014**, *17* (1), 1-52.
- (9) Shields IV, C. W.; Reyes, C. D.; López, G. P. Microfluidic cell sorting: a review of the advances in the separation of cells from debulking to rare cell isolation. *Lab on a Chip* **2015**, *15* (5), 1230-1249.
- (10) Sanjay, S. T.; Fu, G.; Dou, M.; Xu, F.; Liu, R.; Qi, H.; Li, X. Biomarker detection for disease diagnosis using cost-effective microfluidic platforms. *Analyst* **2015**, *140* (21), 7062-7081.
- (11) Collins, D. J.; Ma, Z.; Han, J.; Ai, Y. Continuous micro-vortex-based nanoparticle manipulation via focused surface acoustic waves. *Lab on a Chip* **2017**, *17* (1), 91-103.

- (12) Ding, X.; Li, P.; Lin, S.-C. S.; Stratton, Z. S.; Nama, N.; Guo, F.; Slotcavage, D.; Mao, X.; Shi, J.; Costanzo, F. Surface acoustic wave microfluidics. *Lab on a Chip* **2013**, *13* (18), 3626-3649.
- (13) Wang, Z.; Wang, H.; Becker, R.; Rufo, J.; Yang, S.; Mace, B. E.; Wu, M.; Zou, J.; Laskowitz, D. T.; Huang, T. J. Acoustofluidic separation enables early diagnosis of traumatic brain injury based on circulating exosomes. *Microsystems & nanoengineering* **2021**, *7* (1), 1-11.
- (14) Wu, M.; Ozcelik, A.; Rufo, J.; Wang, Z.; Fang, R.; Jun Huang, T. Acoustofluidic separation of cells and particles. *Microsystems & nanoengineering* **2019**, *5* (1), 1-18.
- (15) Settnes, M.; Bruus, H. Forces acting on a small particle in an acoustical field in a viscous fluid. *Physical Review E* **2012**, *85* (1), 016327.
- (16) Nilsson, A.; Petersson, F.; Jönsson, H.; Laurell, T. Acoustic control of suspended particles in micro fluidic chips. *Lab on a Chip* **2004**, *4* (2), 131-135.
- (17) Nama, N.; Huang, P.-H.; Huang, T. J.; Costanzo, F. Investigation of micromixing by acoustically oscillated sharp-edges. *Biomicrofluidics* **2016**, *10* (2), 024124.
- (18) Wiklund, M.; Green, R.; Ohlin, M. Acoustofluidics 14: Applications of acoustic streaming in microfluidic devices. *Lab on a Chip* **2012**, *12* (14), 2438-2451.
- (19) Lu, J.; Qiu, C.; Ke, M.; Liu, Z. Valley vortex states in sonic crystals. *Physical review letters* **2016**, *116* (9), 093901.
- (20) Huang, P.-H.; Xie, Y.; Ahmed, D.; Rufo, J.; Nama, N.; Chen, Y.; Chan, C. Y.; Huang, T. J. An acoustofluidic micromixer based on oscillating sidewall sharp-edges. *Lab on a Chip* **2013**, *13* (19), 3847-3852.
- (21) Zhao, S.; Huang, P.-H.; Zhang, H.; Rich, J.; Bachman, H.; Ye, J.; Zhang, W.; Chen, C.; Xie, Z.; Tian, Z. Fabrication of tunable, high-molecular-weight polymeric nanoparticles via ultrafast acoustofluidic micromixing. *Lab on a Chip* **2021**, *21* (12), 2453-2463.
- (22) Mao, Z.; Li, P.; Wu, M.; Bachman, H.; Mesyngier, N.; Guo, X.; Liu, S.; Costanzo, F.; Huang, T. J. Enriching nanoparticles via acoustofluidics. *Acs Nano* **2017**, *11* (1), 603-612.
- (23) Collins, D. J.; Ma, Z.; Ai, Y. Highly localized acoustic streaming and size-selective submicrometer particle concentration using high frequency microscale focused acoustic fields. *Analytical chemistry* **2016**, *88* (10), 5513-5522.

- (24) Yan, M.; Lu, J.; Li, F.; Deng, W.; Huang, X.; Ma, J.; Liu, Z. On-chip valley topological materials for elastic wave manipulation. *Nature Materials* **2018**, *17* (11), 993-998.
- (25) Tian, Z.; Shen, C.; Li, J.; Reit, E.; Bachman, H.; Socolar, J. E.; Cummer, S. A.; Jun Huang, T. Dispersion tuning and route reconfiguration of acoustic waves in valley topological phononic crystals. *Nature communications* **2020**, *11* (1), 1-10.
- (26) Davis, R.; Zhou, Y.; Bandaru, P.; Sievenpiper, D. Photonic Topological Insulators: A Beginner's Introduction [Electromagnetic Perspectives]. *IEEE Antennas and Propagation Magazine* **2021**, *63* (3), 112-124.
- (27) Shalaev, M. I.; Walasik, W.; Tsukernik, A.; Xu, Y.; Litchinitser, N. M. Robust topologically protected transport in photonic crystals at telecommunication wavelengths. *Nature nanotechnology* **2019**, *14* (1), 31-34.
- (28) Gao, F.; Xue, H.; Yang, Z.; Lai, K.; Yu, Y.; Lin, X.; Chong, Y.; Shvets, G.; Zhang, B. Topologically protected refraction of robust kink states in valley photonic crystals. *Nature Physics* **2018**, *14* (2), 140-144.
- (29) Huang, P. H.; Zhao, S.; Bachman, H.; Nama, N.; Li, Z.; Chen, C.; Yang, S.; Wu, M.; Zhang, S. P.; Huang, T. J. Acoustofluidic synthesis of particulate nanomaterials. *Advanced Science* **2019**, *6* (19), 1900913.
- (30) Bachman, H.; Huang, P.-H.; Zhao, S.; Yang, S.; Zhang, P.; Fu, H.; Huang, T. J. Acoustofluidic devices controlled by cell phones. *Lab on a Chip* **2018**, *18* (3), 433-441.
- (31) Huang, P.-H.; Nama, N.; Mao, Z.; Li, P.; Rufo, J.; Chen, Y.; Xie, Y.; Wei, C.-H.; Wang, L.; Huang, T. J. A reliable, programmable acoustofluidic pump powered by oscillating sharp-edge structures. *Lab on a Chip* **2014**, *14* (22), 4319.
- (32) Collins, D. J.; Khoo, B. L.; Ma, Z.; Winkler, A.; Weser, R.; Schmidt, H.; Han, J.; Ai, Y. Selective particle and cell capture in a continuous flow using micro-vortex acoustic streaming. *Lab on a Chip* **2017**, *17* (10), 1769-1777.
- (33) Wu, M.; Ouyang, Y.; Wang, Z.; Zhang, R.; Huang, P.-H.; Chen, C.; Li, H.; Li, P.; Quinn, D.; Dao, M. Isolation of exosomes from whole blood by integrating acoustics and microfluidics. *Proceedings of the National Academy of Sciences* **2017**, *114* (40), 10584-10589.
- (34) Wu, M.; Huang, P. H.; Zhang, R.; Mao, Z.; Chen, C.; Kemeny, G.; Li, P.; Lee, A. V.; Gyanchandani, R.; Armstrong, A. J. Circulating Tumor Cell Phenotyping via High-Throughput Acoustic Separation. *Small* **2018**, *14* (32), 1801131.

- (35) Jiang, R.; Agrawal, S.; Aghaamoo, M.; Parajuli, R.; Agrawal, A.; Lee, A. P. Rapid isolation of circulating cancer associated fibroblasts by acoustic microstreaming for assessing metastatic propensity of breast cancer patients. *Lab on a Chip* **2021**, *21* (5), 875-887.
- (36) Li, P.; Mao, Z.; Peng, Z.; Zhou, L.; Chen, Y.; Huang, P.-H.; Truica, C. I.; Drabick, J. J.; El-Deiry, W. S.; Dao, M. Acoustic separation of circulating tumor cells. *Proceedings of the National Academy of Sciences* **2015**, *112* (16), 4970-4975.
- (37) Wu, G. D.; Chen, J.; Hoffmann, C.; Bittinger, K.; Chen, Y.-Y.; Keilbaugh, S. A.; Bewtra, M.; Knights, D.; Walters, W. A.; Knight, R.; et al. Linking long-term dietary patterns with gut microbial enterotypes. *Science (New York, N.Y.)* **2011**, *334* (6052), 105-108.
- (38) Koga, Y.; Yasunaga, M.; Takahashi, A.; Kuroda, J.; Moriya, Y.; Akasu, T.; Fujita, S.; Yamamoto, S.; Baba, H.; Matsumura, Y. MicroRNA expression profiling of exfoliated colonocytes isolated from feces for colorectal cancer screening. *Cancer Prev. Res.* **2010**, *3* (11), 1435-1442.
- (39) Takahashi, M. K.; Tan, X.; Dy, A. J.; Braff, D.; Akana, R. T.; Furuta, Y.; Donghia, N.; Ananthakrishnan, A.; Collins, J. J. A low-cost paper-based synthetic biology platform for analyzing gut microbiota and host biomarkers. *Nat. Commun.* **2018**, *9* (1), 3347.
- (40) Ye, S.; Whiley, D. M.; Ware, R. S.; Sloots, T. P.; Kirkwood, C. D.; Grimwood, K.; Lambert, S. B. Detection of viruses in weekly stool specimens collected during the first 2 years of life: a pilot study of five healthy Australian infants in the rotavirus vaccine era. *J. Med. Virol.* **2017**, *89* (5), 917-921.
- (41) Rossignol, J.-F. A.; Ayoub, A.; Ayers, M. S. Treatment of diarrhea caused by *Cryptosporidium parvum*: a prospective randomized, double-blind, placebo-controlled study of nitazoxanide. *J. Infect. Dis.* **2001**, *184* (1), 103-106.
- (42) Gordon, N. P.; Green, B. B. Factors associated with use and non-use of the Fecal Immunochemical Test (FIT) kit for Colorectal Cancer Screening in Response to a 2012 outreach screening program: a survey study. *BMC Public Health* **2015**, *15* (1), 546.
- (43) Davies, R. J.; Miller, R.; Coleman, N. Colorectal cancer screening: prospects for molecular stool analysis. *Nat. Rev. Cancer* **2005**, *5* (3), 199-209.
- (44) Schaeysbroeck, S. V.; Allen, W. L.; Turkington, R. C.; Johnston, P. G. Implementing prognostic and predictive biomarkers in CRC clinical trials. *Nat. Rev. Clin. Oncol.* **2011**, *8* (4), 222-232.

- (45) Shoemark, D. K.; Allen, S. J. The microbiome and disease: reviewing the links between the oral microbiome, aging, and Alzheimer's disease. *J. Alzheimer's Dis.* **2015**, *43* (3), 725-738.
- (46) Sampson, T. R.; Debelius, J. W.; Thron, T.; Janssen, S.; Shastri, G. G.; Ilhan, Z. E.; Challis, C.; Schretter, C. E.; Rocha, S.; Gradinaru, V. Gut microbiota regulate motor deficits and neuroinflammation in a model of Parkinson's disease. *Cell* **2016**, *167* (6), 1469-1480. e1412.
- (47) Gumus, A.; Ahsan, S.; Dogan, B.; Jiang, L.; Snodgrass, R.; Gardner, A.; Lu, Z.; Simpson, K.; Erickson, D. Solar-thermal complex sample processing for nucleic acid based diagnostics in limited resource settings. *Biomedical Optics Express* **2016**, *7* (5), 1974-1984.
- (48) Chan, C. Y.; Huang, P.-H.; Guo, F.; Ding, X.; Kapur, V.; Mai, J. D.; Yuen, P. K.; Huang, T. J. Accelerating drug discovery via organs-on-chips. *Lab Chip* **2013**, *13* (24), 4697-4710.
- (49) Su, W.; Gao, X.; Jiang, L.; Qin, J. Microfluidic platform towards point-of-care diagnostics in infectious diseases. *J. Chromatogr. A* **2015**, *1377*, 13-26.
- (50) Huang, P.-H.; Chan, C. Y.; Li, P.; Wang, Y.; Nama, N.; Bachman, H.; Huang, T. J. A sharp-edge-based acoustofluidic chemical signal generator. *Lab Chip* **2018**, *18* (10), 1411-1421.
- (51) Wu, M.; Chen, K.; Yang, S.; Wang, Z.; Huang, P.-H.; Mai, J.; Li, Z.-Y.; Huang, T. J. High-throughput cell focusing and separation via acoustofluidic tweezers. *Lab Chip* **2018**, *18* (19), 3003-3010.
- (52) Song, J.; Mauk, M. G.; Hackett, B. A.; Cherry, S.; Bau, H. H.; Liu, C. Instrument-free point-of-care molecular detection of Zika virus. *Anal. Chem.* **2016**, *88* (14), 7289-7294.
- (53) Huang, P.-H.; Ren, L.; Nama, N.; Li, S.; Li, P.; Yao, X.; Cuento, R. A.; Wei, C.-H.; Chen, Y.; Xie, Y.; et al. An acoustofluidic sputum liquefier. *Lab Chip* **2015**, *15* (15), 3125-3131.
- (54) Aroonual, A.; Janvilisri, T.; Ounjai, P.; Chankhamhaengdecha, S. Microfluidics: innovative approaches for rapid diagnosis of antibiotic-resistant bacteria. *Essays Biochem* **2017**, *61* (1), 91-101.
- (55) Ma, L.; Kim, J.; Hatzenpichler, R.; Karymov, M. A.; Hubert, N.; Hanan, I. M.; Chang, E. B.; Ismagilov, R. F. Gene-targeted microfluidic cultivation validated by isolation of a gut bacterium listed in Human Microbiome Project's Most Wanted taxa. *Proc. Natl. Acad. Sci. U. S. A.* **2014**, *111*, 9768-9773.

- (56) Mauk, M.; Song, J.; Bau, H. H.; Gross, R.; Bushman, F. D.; Collman, R. G.; Liu, C. Miniaturized devices for point of care molecular detection of HIV. *Lab Chip* **2017**, *17* (3), 382-394.
- (57) Ahmed, H.; Destgeer, G.; Park, J.; Afzal, M.; Sung, H. J. Sheathless focusing and separation of microparticles using tilted angle travelling surface acoustic waves. *Anal. Chem.* **2018**.
- (58) Connacher, W.; Zhang, N.; Huang, A.; Mei, J.; Zhang, S.; Gopesh, T.; Friend, J. Micro/nano acoustofluidics: materials, phenomena, design, devices, and applications. *Lab Chip* **2018**, *18*, 1952-1996.
- (59) Lillehoj, P. B.; Huang, M.-C.; Truong, N.; Ho, C.-M. Rapid electrochemical detection on a mobile phone. *Lab Chip* **2013**, *13* (15), 2950-2955.
- (60) Chen, Y.; Fang, Z.; Merritt, B.; Strack, D.; Xu, J.; Lee, S. Onset of particle trapping and release via acoustic bubbles. *Lab Chip* **2016**, *16* (16), 3024-3032.
- (61) Collins, D. J.; O'Rourke, R.; Devendran, C.; Ma, Z.; Han, J.; Neild, A.; Ai, Y. Self-aligned acoustofluidic particle focusing and patterning in microfluidic channels from channel-based acoustic waveguides. *Phys. Rev. Lett.* **2018**, *120* (7), 074502.
- (62) Castro, C.; Rosillo, C.; Tsutsui, H. Characterizing effects of humidity and channel size on imbibition in paper-based microfluidic channels. *Microfluid. Nanofluid.* **2017**, *21* (2), 21.
- (63) Gracioso Martins, A. M.; Glass, N. R.; Harrison, S.; Rezk, A. R.; Porter, N. A.; Carpenter, P. D.; Du Plessis, J.; Friend, J. R.; Yeo, L. Y. Toward complete miniaturisation of flow injection analysis systems: microfluidic enhancement of chemiluminescent detection. *Anal. Chem.* **2014**, *86* (21), 10812-10819.
- (64) Ozcelik, A.; Rufo, J.; Guo, F.; Gu, Y.; Li, P.; Lata, J.; Huang, T. J. Acoustic tweezers for the life sciences. *Nat. Methods* **2018**, *15* (12), 1021-1028. DOI: 10.1038/s41592-018-0222-9.
- (65) Li, P.; Huang, T. J. Applications of Acoustofluidics in Bioanalytical Chemistry. *Anal. Chem.* **2018**.
- (66) Zhang, S. P.; Lata, J.; Chen, C.; Mai, J.; Guo, F.; Tian, Z.; Ren, L.; Mao, Z.; Huang, P.-H.; Li, P. Digital acoustofluidics enables contactless and programmable liquid handling. *Nat. Commun.* **2018**, *9* (1), 2928.

- (67) Wu, M.; Ouyang, Y.; Wang, Z.; Zhang, R.; Huang, P.-H.; Chen, C.; Li, H.; Li, P.; Quinn, D.; Dao, M. Isolation of exosomes from whole blood by integrating acoustics and microfluidics. *Proc. Natl. Acad. Sci. U. S. A.* **2017**, 201709210.
- (68) Yang, H. R.; Seo, J. K. Helicobacter pylori stool antigen (HpSA) tests in children before and after eradication therapy: comparison of rapid immunochromatographic assay and HpSA ELISA. *Dig. Dis. Sci.* **2008**, 53 (8), 2053-2058.
- (69) Bunyakul, N.; Promptmas, C.; Baeumner, A. J. Microfluidic biosensor for cholera toxin detection in fecal samples. *Anal. Bioanal. Chem.* **2015**, 407 (3), 727-736.
- (70) Phaneuf, C. R.; Mangadu, B.; Piccini, M. E.; Singh, A. K.; Koh, C.-Y. Rapid, portable, multiplexed detection of bacterial pathogens directly from clinical sample matrices. *Biosensors* **2016**, 6 (4), 49.
- (71) Kim, G.; Moon, J.-H.; Moh, C.-Y.; Lim, J.-g. A microfluidic nano-biosensor for the detection of pathogenic Salmonella. *Biosens. Bioelectron.* **2015**, 67, 243-247.
- (72) Li, Y.; Zhang, C.; Xing, D. Integrated microfluidic reverse transcription-polymerase chain reaction for rapid detection of food-or waterborne pathogenic rotavirus. *Anal. Biochem.* **2011**, 415 (2), 87-96.
- (73) Mosley, O.; Melling, L.; Tarn, M. D.; Kemp, C.; Esfahani, M. M.; Pamme, N.; Shaw, K. J. Sample introduction interface for on-chip nucleic acid-based analysis of Helicobacter pylori from stool samples. *Lab Chip* **2016**, 16 (11), 2108-2115.
- (74) Zhang, H.; Wang, X.; Ma, Q.; Zhou, Z.; Fang, J. Rapid detection of low-abundance K-ras mutation in stools of colorectal cancer patients using chip-based temperature gradient capillary electrophoresis. *Lab. Invest.* **2011**, 91 (5), 788-798.
- (75) Lee, C.-Y.; Wang, W.-T.; Liu, C.-C.; Fu, L.-M. Passive mixers in microfluidic systems: A review. *Chem. Eng. J.* **2016**, 288, 146-160.
- (76) Bhagat, A. A. S.; Peterson, E. T.; Papautsky, I. A passive planar micromixer with obstructions for mixing at low Reynolds numbers. *J. Micromech. Microeng.* **2007**, 17 (5), 1017-1024.
- (77) Cui, X.; Ren, L.; Shan, Y.; Wang, X.; Yang, Z.; Li, C.; Xu, J.; Ma, B. Smartphone-based rapid quantification of viable bacteria by single-cell microdroplet turbidity imaging. *Analyst* **2018**, 143, 3309-3316.

- (78) Ren, L.; Yang, S.; Zhang, P.; Qu, Z.; Mao, Z.; Huang, P. H.; Chen, Y.; Wu, M.; Wang, L.; Li, P.; et al. Standing Surface Acoustic Wave (SSAW)-Based Fluorescence-Activated Cell Sorter. *Small* **2018**, *14* (40), 1801996.
- (79) Utharala, R.; Tseng, Q.; Furlong, E. E.; Merten, C. A. A Versatile, Low-Cost, Multiway Microfluidic Sorter for Droplets, Cells, and Embryos. *Anal. Chem.* **2018**, *90* (10), 5982-5988.
- (80) Jang, S.; Lee, B.; Jeong, H.-H.; Jin, S. H.; Jang, S.; Kim, S. G.; Jung, G. Y.; Lee, C.-S. On-chip analysis, indexing and screening for chemical producing bacteria in a microfluidic static droplet array. *Lab Chip* **2016**, *16* (10), 1909-1916.
- (81) Lillehoj, P. B.; Kaplan, C. W.; He, J.; Shi, W.; Ho, C.-M. Rapid, electrical impedance detection of bacterial pathogens using immobilized antimicrobial peptides. *J. Lab. Autom.* **2014**, *19* (1), 42-49.
- (82) Gratton, J.; Phetcharaburanin, J.; Mullish, B. H.; Williams, H. R.; Thursz, M.; Nicholson, J. K.; Holmes, E.; Marchesi, J. R.; Li, J. V. Optimized sample handling strategy for metabolic profiling of human feces. *Anal. Chem.* **2016**, *88* (9), 4661-4668.
- (83) Gillers, S.; Atkinson, C. D.; Bartoo, A. C.; Mahalanabis, M.; Boylan, M. O.; Schwartz, J. H.; Klapperich, C.; Singh, S. K. Microscale sample preparation for PCR of *C. difficile* infected stool. *J. Microbiol. Methods* **2009**, *78* (2), 203-207.
- (84) Periago, M. V.; Diniz, R. C.; Pinto, S. A.; Yakovleva, A.; Correa-Oliveira, R.; Diemert, D. J.; Bethony, J. M. The right tool for the job: detection of soil-transmitted helminths in areas co-endemic for other helminths. *PLoS Negl. Trop. Dis.* **2015**, *9* (8), e0003967.
- (85) Riglar, D. T.; Giessen, T. W.; Baym, M.; Kerns, S. J.; Niederhuber, M. J.; Bronson, R. T.; Kotula, J. W.; Gerber, G. K.; Way, J. C.; Silver, P. A. Engineered bacteria can function in the mammalian gut long-term as live diagnostics of inflammation. *Nat. Biotechnol.* **2017**, *35* (7), 653-658.
- (86) Skinner, S. O.; Sepúlveda, L. A.; Xu, H.; Golding, I. Measuring mRNA copy number in individual *Escherichia coli* cells using single-molecule fluorescent in situ hybridization. *Nat. Protoc.* **2013**, *8* (6), 1100-1113.
- (87) Fu, H.; Liu, X.; Li, S. Mixing indexes considering the combination of mean and dispersion information from intensity images for the performance estimation of micromixing. *RSC advances* **2017**, *7* (18), 10906-10914.

- (88) Walker, G. M.; Sai, J.; Richmond, A.; Stremmer, M.; Chung, C. Y.; Wikswo, J. P. Effects of flow and diffusion on chemotaxis studies in a microfabricated gradient generator. *Lab Chip* **2005**, *5* (6), 611-618.
- (89) Kinsler, L. E.; Frey, A. R.; Coppens, A. B.; Sanders, J. V. *Fundamentals of acoustics*; 1999.
- (90) Nama, N.; Huang, P.-H.; Huang, T. J.; Costanzo, F. Investigation of acoustic streaming patterns around oscillating sharp edges. *Lab Chip* **2014**, *14* (15), 2824-2836.
- (91) Ozcelik, A.; Ahmed, D.; Xie, Y.; Nama, N.; Qu, Z.; Nawaz, A. A.; Huang, T. J. An acoustofluidic micromixer via bubble inception and cavitation from microchannel sidewalls. *Anal. Chem.* **2014**, *86* (10), 5083-5088.
- (92) Labbaf, S.; Ghanbar, H.; Stride, E.; Edirisinghe, M. Preparation of multilayered polymeric structures using a novel four-needle coaxial electrohydrodynamic device. *Macromol. Rapid Commun.* **2014**, *35* (6), 618-623.
- (93) Nama, N.; Barnkob, R.; Mao, Z.; Kähler, C. J.; Costanzo, F.; Huang, T. J. Numerical study of acoustophoretic motion of particles in a PDMS microchannel driven by surface acoustic waves. *Lab Chip* **2015**, *15* (12), 2700-2709.
- (94) Ophir, J.; Jaeger, P. A ternary solution for independent acoustic impedance and speed of sound matching to biological tissues. *Ultrasonic imaging* **1982**, *4* (2), 163-170.
- (95) Leininger, D. J.; Roberson, J. R.; Elvinger, F. Use of eosin methylene blue agar to differentiate *Escherichia coli* from other gram-negative mastitis pathogens. *J. Vet. Diagn. Invest.* **2001**, *13* (3), 273-275.
- (96) Antony, A. C.; Paul, M. K.; Silvester, R.; Aneesa, P.; Suresh, K.; Divya, P.; Paul, S.; Fathima, P.; Abdulla, M. H. Comparative evaluation of EMB agar and Hicrome *E. coli* agar for differentiation of green metallic sheen producing non *E. coli* and typical *E. coli* colonies from food and environmental samples. *J. Pure. Appl. Microbiol.* **2016**, *10* (4), 2863-2871.
- (97) Rollenske, T.; Szijarto, V.; Lukasiewicz, J.; Guachalla, L. M.; Stojkovic, K.; Hartl, K.; Stulik, L.; Kocher, S.; Lasitschka, F.; Al-Saeedi, M.; et al. Cross-specificity of protective human antibodies against *Klebsiella pneumoniae* LPS O-antigen. *Nat. Immunol.* **2018**, *19*, 617-624.
- (98) Berney, M.; Hammes, F.; Bosshard, F.; Weilenmann, H.-U.; Egli, T. Assessment and interpretation of bacterial viability by using the LIVE/DEAD BacLight Kit in combination with flow cytometry. *Appl. Environ. Microbiol.* **2007**, *73* (10), 3283-3290.

- (99) Valencia, P. M.; Pridgen, E. M.; Rhee, M.; Langer, R.; Farokhzad, O. C.; Karnik, R. Microfluidic platform for combinatorial synthesis and optimization of targeted nanoparticles for cancer therapy. *ACS nano* **2013**, *7* (12), 10671-10680.
- (100) Zhao, X.; Bian, F.; Sun, L.; Cai, L.; Li, L.; Zhao, Y. Microfluidic Generation of Nanomaterials for Biomedical Applications. *Small* **2020**, *16* (9), 1901943.
- (101) Zhang, H.; Zhu, Y.; Shen, Y. Microfluidics for cancer nanomedicine: from fabrication to evaluation. *Small* **2018**, *14* (28), 1800360.
- (102) Reboud, J.; Bourquin, Y.; Wilson, R.; Pall, G. S.; Jiwaji, M.; Pitt, A. R.; Graham, A.; Waters, A. P.; Cooper, J. M. Shaping acoustic fields as a toolset for microfluidic manipulations in diagnostic technologies. *Proc. Natl. Acad. Sci. U. S. A.* **2012**, *109* (38), 15162-15167.
- (103) Friend, J.; Yeo, L. Y. Microscale acoustofluidics: Microfluidics driven via acoustics and ultrasonics. *Reviews of Modern Physics* **2011**, *83* (2), 647.
- (104) Ahmed, H.; Destgeer, G.; Park, J.; Jung, J. H.; Sung, H. J. Vertical hydrodynamic focusing and continuous acoustofluidic separation of particles via upward migration. *Advanced science* **2018**, *5* (2), 1700285.
- (105) Li, P.; Huang, T. J. Applications of acoustofluidics in bioanalytical chemistry. *Anal. Chem.* **2018**, *91* (1), 757-767.
- (106) Xie, Y.; Bachman, H.; Huang, T. J. Acoustofluidic methods in cell analysis. *TrAC, Trends Anal. Chem.* **2019**, *117*, 280-290.
- (107) Connacher, W.; Zhang, N.; Huang, A.; Mei, J.; Zhang, S.; Gopesh, T.; Friend, J. Micro/nano acoustofluidics: materials, phenomena, design, devices, and applications. *Lab Chip* **2018**, *18* (14), 1952-1996.
- (108) Zhou, Y.; Wang, H.; Ma, Z.; Yang, J. K.; Ai, Y. Acoustic Vibration-Induced Actuation of Multiple Microrotors in Microfluidics. *Advanced Materials Technologies* **2020**, *5* (9), 2000323.
- (109) Chen, B.; Wu, Y.; Ao, Z.; Cai, H.; Nunez, A.; Liu, Y.; Foley, J.; Nephew, K.; Lu, X.; Guo, F. High-throughput acoustofluidic fabrication of tumor spheroids. *Lab Chip* **2019**, *19* (10), 1755-1763.
- (110) Schmid, L.; Weitz, D. A.; Franke, T. Sorting drops and cells with acoustics: acoustic microfluidic fluorescence-activated cell sorter. *Lab Chip* **2014**, *14* (19), 3710-3718.

- (111) Zhao, S.; Wu, M.; Yang, S.; Wu, Y.; Gu, Y.; Chen, C.; Ye, J.; Xie, Z.; Tian, Z.; Bachman, H. A disposable acoustofluidic chip for nano/microparticle separation using unidirectional acoustic transducers. *Lab Chip* **2020**, *20* (7), 1298-1308.
- (112) Pessoa, A. C.; Sipoli, C. C.; Lucimara, G. Effects of diffusion and mixing pattern on microfluidic-assisted synthesis of chitosan/ATP nanoparticles. *Lab on a Chip* **2017**, *17* (13), 2281-2293.
- (113) Hasani-Sadrabadi, M. M.; Taranejoo, S.; Dashtimoghadam, E.; Bahlakeh, G.; Majedi, F. S.; VanDersarl, J. J.; Janmaleki, M.; Sharifi, F.; Bertsch, A.; Hourigan, K. Microfluidic manipulation of core/shell nanoparticles for oral delivery of chemotherapeutics: a new treatment approach for colorectal cancer. *Adv. Mater.* **2016**, *28* (21), 4134-4141.
- (114) Augustsson, P.; Karlsen, J. T.; Su, H.-W.; Bruus, H.; Voldman, J. Iso-acoustic focusing of cells for size-insensitive acousto-mechanical phenotyping. *Nat. Commun.* **2016**, *7* (1), 1-9.
- (115) Olofsson, K.; Carannante, V.; Ohlin, M.; Frisk, T.; Kushiro, K.; Takai, M.; Lundqvist, A.; Önfelt, B.; Wiklund, M. Acoustic formation of multicellular tumor spheroids enabling on-chip functional and structural imaging. *Lab Chip* **2018**, *18* (16), 2466-2476.
- (116) Tian, L.; Martin, N.; Bassindale, P. G.; Patil, A. J.; Li, M.; Barnes, A.; Drinkwater, B. W.; Mann, S. Spontaneous assembly of chemically encoded two-dimensional coacervate droplet arrays by acoustic wave patterning. *Nat. Commun.* **2016**, *7* (1), 1-10.
- (117) Cushing, K.; Undvall, E.; Ceder, Y.; Lilja, H.; Laurell, T. Reducing WBC background in cancer cell separation products by negative acoustic contrast particle immuno-acoustophoresis. *Anal. Chim. Acta* **2018**, *1000*, 256-264.
- (118) Collins, D. J.; Morahan, B.; Garcia-Bustos, J.; Doerig, C.; Plebanski, M.; Neild, A. Two-dimensional single-cell patterning with one cell per well driven by surface acoustic waves. *Nat. Commun.* **2015**, *6* (1), 1-11.
- (119) Biroun, M. H.; Li, J.; Tao, R.; Rahmati, M.; McHale, G.; Dong, L.; Jangi, M.; Torun, H.; Fu, Y. Acoustic Waves for Active Reduction of Contact Time in Droplet Impact. *Physical Review Applied* **2020**, *14* (2), 024029.
- (120) Hsu, M. N.; Wei, S. C.; Guo, S.; Phan, D. T.; Zhang, Y.; Chen, C. H. Smart Hydrogel Microfluidics for Single-Cell Multiplexed Secretomic Analysis with High Sensitivity. *Small* **2018**, *14* (49), 1802918.

- (121) Tao, R.; McHale, G.; Reboud, J.; Cooper, J. M.; Torun, H.; Luo, J.; Luo, J.; Yang, X.; Zhou, J.; Canyelles-Pericas, P. Hierarchical nanotexturing enables acoustofluidics on slippery yet sticky, flexible surfaces. *Nano Lett.* **2020**, *20* (5), 3263-3270.
- (122) Melde, K.; Choi, E.; Wu, Z.; Palagi, S.; Qiu, T.; Fischer, P. Acoustic fabrication via the assembly and fusion of particles. *Adv. Mater.* **2018**, *30* (3), 1704507.
- (123) Vladisavljević, G. T.; Shahmohamadi, H.; Das, D. B.; Ekanem, E. E.; Tauanov, Z.; Sharma, L. Glass capillary microfluidics for production of monodispersed poly (DL-lactic acid) and polycaprolactone microparticles: Experiments and numerical simulations. *J. Colloid Interface Sci.* **2014**, *418*, 163-170.
- (124) Brzeziński, M.; Socka, M.; Kost, B. Microfluidics for producing polylactide nanoparticles and microparticles and their drug delivery application. *Polym. Int.* **2019**, *68* (6), 997-1014.
- (125) Liu, D.; Zhang, H.; Cito, S.; Fan, J.; Mäkilä, E.; Salonen, J.; Hirvonen, J.; Sikanen, T. M.; Weitz, D. A.; Santos, H. I. A. Core/shell nanocomposites produced by superfast sequential microfluidic nanoprecipitation. *Nano Lett.* **2017**, *17* (2), 606-614.
- (126) Zhao, S.; He, W.; Ma, Z.; Liu, P.; Huang, P.-H.; Bachman, H.; Wang, L.; Yang, S.; Tian, Z.; Wang, Z. On-chip stool liquefaction via acoustofluidics. *Lab on a Chip* **2019**, *19* (6), 941-947.
- (127) JunáHuang, T. Acoustofluidic devices controlled by cell phones. *Lab Chip* **2018**, *18* (3), 433-441.
- (128) Lei, J.; Hill, M.; Glynne-Jones, P. Numerical simulation of 3D boundary-driven acoustic streaming in microfluidic devices. *Lab Chip* **2014**, *14* (3), 532-541.
- (129) Wang, Z.; Huang, P.-H.; Chen, C.; Bachman, H.; Zhao, S.; Yang, S.; Huang, T. J. Cell lysis via acoustically oscillating sharp edges. *Lab Chip* **2019**, *19* (24), 4021-4032.
- (130) Avgoustakis, K. Pegylated poly (lactide) and poly (lactide-co-glycolide) nanoparticles: preparation, properties and possible applications in drug delivery. *Curr. Drug Del.* **2004**, *1* (4), 321-333.
- (131) Jokerst, J. V.; Lobovkina, T.; Zare, R. N.; Gambhir, S. S. Nanoparticle PEGylation for imaging and therapy. *Nanomedicine* **2011**, *6* (4), 715-728.

- (132) Locatelli, E.; Franchini, M. C. Biodegradable PLGA-b-PEG polymeric nanoparticles: synthesis, properties, and nanomedical applications as drug delivery system. *J. Nanopart. Res.* **2012**, *14* (12), 1316.
- (133) Van Phan, H.; Coşkun, M. B.; Şeşen, M.; Pandraud, G.; Neild, A.; Alan, T. Vibrating membrane with discontinuities for rapid and efficient microfluidic mixing. *Lab Chip* **2015**, *15* (21), 4206-4216.
- (134) Cui, X.; Mao, S.; Liu, M.; Yuan, H.; Du, Y. Mechanism of surfactant micelle formation. *Langmuir* **2008**, *24* (19), 10771-10775.
- (135) Shields IV, C. W.; Sun, D.; Johnson, K. A.; Duval, K. A.; Rodriguez, A. V.; Gao, L.; Dayton, P. A.; López, G. P. Nucleation and growth synthesis of siloxane gels to form functional, monodisperse, and acoustically programmable particles. *Angew. Chem. Int. Ed.* **2014**, *53* (31), 8070-8073.
- (136) Liu, D.; Cito, S.; Zhang, Y.; Wang, C. F.; Sikanen, T. M.; Santos, H. A. A versatile and robust microfluidic platform toward high throughput synthesis of homogeneous nanoparticles with tunable properties. *Advanced Materials* **2015**, *27* (14), 2298-2304.
- (137) Majedi, F. S.; Hasani-Sadrabadi, M. M.; VanDersarl, J. J.; Mokarram, N.; Hojjati-Emami, S.; Dashtimoghadam, E.; Bonakdar, S.; Shokrgozar, M. A.; Bertsch, A.; Renaud, P. On-chip fabrication of paclitaxel-loaded chitosan nanoparticles for cancer therapeutics. *Advanced Functional Materials* **2014**, *24* (4), 432-441.
- (138) Thevenot, J.; Troutier, A.-L.; Putaux, J.-L.; Delair, T.; Ladaviere, C. Effect of the polymer nature on the structural organization of lipid/polymer particle assemblies. *The Journal of Physical Chemistry B* **2008**, *112* (44), 13812-13822.
- (139) Griffiths, P. C.; Cattoz, B.; Ibrahim, M. S.; Anuonye, J. C. Probing the interaction of nanoparticles with mucin for drug delivery applications using dynamic light scattering. *European Journal of Pharmaceutics and Biopharmaceutics* **2015**, *97*, 218-222.
- (140) Wunsch, B. H.; Smith, J. T.; Gifford, S. M.; Wang, C.; Brink, M.; Bruce, R. L.; Austin, R. H.; Stolovitzky, G.; Astier, Y. Nanoscale lateral displacement arrays for the separation of exosomes and colloids down to 20 nm. *Nat. Nanotechnol.* **2016**, *11* (11), 936.
- (141) Ai, Y.; Sanders, C. K.; Marrone, B. L. Separation of Escherichia coli bacteria from peripheral blood mononuclear cells using standing surface acoustic waves. *Anal. Chem.* **2013**, *85* (19), 9126-9134.

- (142) Lee, J.-J.; Jeong, K. J.; Hashimoto, M.; Kwon, A. H.; Rwei, A.; Shankarappa, S. A.; Tsui, J. H.; Kohane, D. S. Synthetic ligand-coated magnetic nanoparticles for microfluidic bacterial separation from blood. *Nano Lett.* **2013**, *14* (1), 1-5.
- (143) Dow, P.; Kotz, K.; Gruszka, S.; Holder, J.; Fiering, J. Acoustic separation in plastic microfluidics for rapid detection of bacteria in blood using engineered bacteriophage. *Lab Chip* **2018**, *18* (6), 923-932.
- (144) Ding, X.; Peng, Z.; Lin, S.-C. S.; Geri, M.; Li, S.; Li, P.; Chen, Y.; Dao, M.; Suresh, S.; Huang, T. J. Cell separation using tilted-angle standing surface acoustic waves. *Proc. Natl. Acad. Sci. U. S. A.* **2014**, *111* (36), 12992-12997.
- (145) Zhao, W.; Zhu, T.; Cheng, R.; Liu, Y.; He, J.; Qiu, H.; Wang, L.; Nagy, T.; Querec, T. D.; Unger, E. R. Label-free and continuous-flow ferrohydrodynamic separation of HeLa cells and blood cells in biocompatible ferrofluids. *Adv. Funct. Mater.* **2016**, *26* (22), 3990-3998.
- (146) Wu, M.; Mao, Z.; Chen, K.; Bachman, H.; Chen, Y.; Rufo, J.; Ren, L.; Li, P.; Wang, L.; Huang, T. J. Acoustic separation of nanoparticles in continuous flow. *Adv. Funct. Mater.* **2017**, *27* (14), 1606039.
- (147) Aghaamoo, M.; Aghilinejad, A.; Chen, X.; Xu, J. On the design of deterministic dielectrophoresis for continuous separation of circulating tumor cells from peripheral blood cells. *Electrophoresis* **2019**, *40* (10), 1486-1493.
- (148) Ozcelik, A.; Rufo, J.; Guo, F.; Gu, Y.; Li, P.; Lata, J.; Huang, T. J. Acoustic tweezers for the life sciences. *Nat. Methods* **2018**, *15* (12), 1. DOI: 10.1038/s41592-018-0222-9.
- (149) Friedrich, S. M.; Bang, R.; Li, A.; Wang, T.-H. Versatile Analysis of DNA-Biomolecule Interactions in Solution by Hydrodynamic Separation and Single Molecule Detection. *Anal. Chem.* **2019**, *91* (4), 2822-2830.
- (150) MacDonald, M. P.; Spalding, G. C.; Dholakia, K. Microfluidic sorting in an optical lattice. *Nature* **2003**, *426* (6965), 421.
- (151) Kang, B.; Shin, J.; Park, H.-J.; Rhyou, C.; Kang, D.; Lee, S.-J.; Yoon, Y.-s.; Cho, S.-W.; Lee, H. High-resolution acoustophoretic 3D cell patterning to construct functional collateral cylindroids for ischemia therapy. *Nat. Commun.* **2018**, *9* (1), 5402.
- (152) Shilton, R. J.; Travaglini, M.; Beltram, F.; Cecchini, M. Nanoliter-droplet acoustic streaming via ultra high frequency surface acoustic waves. *Adv. Mater.* **2014**, *26* (29), 4941-4946.

- (153) Miansari, M.; Friend, J. R. Acoustic Nanofluidics via Room-Temperature Lithium Niobate Bonding: A Platform for Actuation and Manipulation of Nanoconfined Fluids and Particles. *Adv. Funct. Mater.* **2016**, *26* (43), 7861-7872.
- (154) Bourquin, Y.; Wilson, R.; Zhang, Y.; Reboud, J.; Cooper, J. M. Phononic crystals for shaping fluids. *Adv. Mater.* **2011**, *23* (12), 1458-1462.
- (155) Collins, D. J.; Morahan, B.; Garcia-Bustos, J.; Doerig, C.; Plebanski, M.; Neild, A. Two-dimensional single-cell patterning with one cell per well driven by surface acoustic waves. *Nat. Commun.* **2015**, *6*, 8686.
- (156) Ahmed, H.; Rezk, A. R.; Carey, B. J.; Wang, Y.; Mohiuddin, M.; Berean, K. J.; Russo, S. P.; Kalantar-zadeh, K.; Yeo, L. Y. Ultrafast Acoustofluidic Exfoliation of Stratified Crystals. *Adv. Mater.* **2018**, *30* (20), 1704756.
- (157) Guo, F.; Mao, Z.; Chen, Y.; Xie, Z.; Lata, J. P.; Li, P.; Ren, L.; Liu, J.; Yang, J.; Dao, M. Three-dimensional manipulation of single cells using surface acoustic waves. *Proc. Natl. Acad. Sci. U. S. A.* **2016**, *113* (6), 1522-1527.
- (158) Cao, W.-K.; Wu, L.-T.; Zhang, C.; Ke, J.-C.; Cheng, Q.; Cui, T.-J.; Jing, Y. Asymmetric transmission of acoustic waves in a waveguide via gradient index metamaterials. *Science Bulletin* **2019**.
- (159) Collins, D. J.; Devendran, C.; Ma, Z.; Ng, J. W.; Neild, A.; Ai, Y. Acoustic tweezers via sub-time-of-flight regime surface acoustic waves. *Science advances* **2016**, *2* (7), e1600089.
- (160) Mutafooulos, K.; Spink, P.; Lofstrom, C.; Lu, P.; Lu, H.; Sharpe, J.; Franke, T.; Weitz, D. Traveling surface acoustic wave (TSAW) microfluidic fluorescence activated cell sorter (μ FACS). *Lab Chip* **2019**.
- (161) Skowronek, V.; Rambach, R. W.; Schmid, L.; Haase, K.; Franke, T. Particle deflection in a poly (dimethylsiloxane) microchannel using a propagating surface acoustic wave: size and frequency dependence. *Anal. Chem.* **2013**, *85* (20), 9955-9959.
- (162) Lee, K.; Shao, H.; Weissleder, R.; Lee, H. Acoustic purification of extracellular microvesicles. *ACS nano* **2015**, *9* (3), 2321-2327.
- (163) Ahmed, H.; Destgeer, G.; Park, J.; Afzal, M.; Sung, H. J. Sheathless focusing and separation of microparticles using tilted-angle traveling surface acoustic waves. *Anal. Chem.* **2018**, *90* (14), 8546-8552.

- (164) Tian, Z.; Yang, S.; Huang, P.-H.; Wang, Z.; Zhang, P.; Gu, Y.; Bachman, H.; Chen, C.; Wu, M.; Xie, Y. Wave number–spiral acoustic tweezers for dynamic and reconfigurable manipulation of particles and cells. *Science advances* **2019**, *5* (5), eaau6062.
- (165) Park, J.; Jung, J. H.; Park, K.; Destgeer, G.; Ahmed, H.; Ahmad, R.; Sung, H. J. On-demand acoustic droplet splitting and steering in a disposable microfluidic chip. *Lab Chip* **2018**, *18* (3), 422-432.
- (166) li, P.; Ma, Z.; Zhou, Y.; Collins, D. J.; Wang, Z.; Ai, Y. Detachable Acoustophoretic System for Fluorescence Activated Sorting at Single Droplet Level. *Anal. Chem.* **2019**.
- (167) Park, J.; Jung, J. H.; Destgeer, G.; Ahmed, H.; Park, K.; Sung, H. J. Acoustothermal tweezer for droplet sorting in a disposable microfluidic chip. *Lab Chip* **2017**, *17* (6), 1031-1040.
- (168) Guo, F.; Xie, Y.; Li, S.; Lata, J.; Ren, L.; Mao, Z.; Ren, B.; Wu, M.; Ozcelik, A.; Huang, T. J. Reusable acoustic tweezers for disposable devices. *Lab Chip* **2015**, *15* (24), 4517-4523.
- (169) Witte, C.; Reboud, J.; Wilson, R.; Cooper, J.; Neale, S. Microfluidic resonant cavities enable acoustophoresis on a disposable superstrate. *Lab Chip* **2014**, *14* (21), 4277-4283.
- (170) Ma, Z.; Collins, D. J.; Ai, Y. Detachable acoustofluidic system for particle separation via a traveling surface acoustic wave. *Anal. Chem.* **2016**, *88* (10), 5316-5323.
- (171) Wu, M.; Chen, C.; Wang, Z.; Bachman, H.; Ouyang, Y.; Huang, P.-H.; Sadovsky, Y.; Huang, T. J. Separating extracellular vesicles and lipoproteins via acoustofluidics. *Lab Chip* **2019**, *19* (7), 1174-1182.
- (172) Tian, L.; Martin, N.; Bassindale, P. G.; Patil, A. J.; Li, M.; Barnes, A.; Drinkwater, B. W.; Mann, S. Spontaneous assembly of chemically encoded two-dimensional coacervate droplet arrays by acoustic wave patterning. *Nat. Commun.* **2016**, *7*, 13068.
- (173) Caleap, M.; Drinkwater, B. W. Acoustically trapped colloidal crystals that are reconfigurable in real time. *Proc. Natl. Acad. Sci. U. S. A.* **2014**, *111* (17), 6226-6230.
- (174) Xu, K.; Clark, C. P.; Poe, B. L.; Lounsbury, J. A.; Nilsson, J.; Laurell, T.; Landers, J. P. Isolation of a Low Number of Sperm Cells from Female DNA in a Glass–PDMS–Glass Microchip via Bead-Assisted Acoustic Differential Extraction. *Anal. Chem.* **2019**, *91* (3), 2186-2191.

- (175) Ahmed, H.; Lee, L.; Darmanin, C.; Yeo, L. Y. A novel acoustofluidic nebulization technique yielding new crystallization morphologies. *Adv. Mater.* **2018**, *30* (3), 1602040.
- (176) Lin, T.-Y.; Do, T.; Kwon, P.; Lillehoj, P. B. 3D printed metal molds for hot embossing plastic microfluidic devices. *Lab Chip* **2017**, *17* (2), 241-247.
- (177) Lin, Y.; Gao, Y.; Wu, M.; Zhou, R.; Chung, D.; Caraveo, G.; Xu, J. Acoustofluidic stick-and-play micropump built on foil for single-cell trapping. *Lab Chip* **2019**.
- (178) Lillehoj, P. B.; Wei, F.; Ho, C.-M. A self-pumping lab-on-a-chip for rapid detection of botulinum toxin. *Lab Chip* **2010**, *10* (17), 2265-2270.
- (179) Liu, C.; Thompson, J. A.; Bau, H. H. A membrane-based, high-efficiency, microfluidic debubbler. *Lab Chip* **2011**, *11* (9), 1688-1693.
- (180) Jonnalagadda, U. S.; Hill, M.; Messaoudi, W.; Cook, R. B.; Oreffo, R. O.; Glynn-Jones, P.; Tare, R. S. Acoustically modulated biomechanical stimulation for human cartilage tissue engineering. *Lab Chip* **2018**, *18* (3), 473-485.
- (181) Huang, P. H.; Zhao, S.; Bachman, H.; Nama, N.; Li, Z.; Chen, C.; Yang, S.; Wu, M.; Zhang, S. P.; Huang, T. J. Acoustofluidic Synthesis of Particulate Nanomaterials. *Advanced Science* **2019**, 1900913.
- (182) Wu, M.; Ozcelik, A.; Rufo, J.; Wang, Z.; Fang, R.; Huang, T. J. Acoustofluidic separation of cells and particles. *Microsystems & nanoengineering* **2019**, *5* (1), 32.
- (183) Xie, Y.; Bachman, H.; Huang, T. J. Acoustofluidic methods in cell analysis. *TrAC, Trends Anal. Chem.* **2019**.
- (184) Schmid, H.; Michel, B. Siloxane polymers for high-resolution, high-accuracy soft lithography. *Macromolecules* **2000**, *33* (8), 3042-3049.
- (185) He, W.; Huang, L.; Feng, Y.; Liang, F.; Ding, W.; Wang, W. Highly integrated microfluidic device for cell pairing, fusion and culture. *Biomicrofluidics* **2019**, *13* (5), 054109.
- (186) Tsou, J. K.; Liu, J.; Barakat, A. I.; Insana, M. F. Role of ultrasonic shear rate estimation errors in assessing inflammatory response and vascular risk. *Ultrasound Med. Biol.* **2008**, *34* (6), 963-972.
- (187) Thouvenot, A.; Poepping, T.; Peters, T. M.; Chen, E. C. Characterization of various tissue mimicking materials for medical ultrasound imaging. In *Medical Imaging 2016*:

Physics of Medical Imaging, 2016; International Society for Optics and Photonics: Vol. 9783, p 97835E.

(188) Anwar, K.; Han, T.; Kim, S. M. Reversible sealing techniques for microdevice applications. *Sensors Actuators B: Chem.* **2011**, *153* (2), 301-311.

(189) Devendran, C.; Collins, D. J.; Ai, Y.; Neild, A. Huygens-Fresnel acoustic interference and the development of robust time-averaged patterns from traveling surface acoustic waves. *Phys. Rev. Lett.* **2017**, *118* (15), 154501.

(190) Li, S.; Ma, F.; Bachman, H.; Cameron, C. E.; Zeng, X.; Huang, T. J. Acoustofluidic bacteria separation. *J. Micromech. Microeng.* **2016**, *27* (1), 015031.

(191) Karlsen, J. T.; Bruus, H. Forces acting on a small particle in an acoustical field in a thermoviscous fluid. *Physical Review E* **2015**, *92* (4), 043010.

(192) Zhao, S.; He, W.; Ma, Z.; Liu, P.; Huang, P.-H.; Bachman, H.; Wang, L.; Yang, S.; Tian, Z.; Wang, Z. On-chip stool liquefaction via acoustofluidics. *Lab Chip* **2019**.

(193) He, C.; Ni, X.; Ge, H.; Sun, X.-C.; Chen, Y.-B.; Lu, M.-H.; Liu, X.-P.; Chen, Y.-F. Acoustic topological insulator and robust one-way sound transport. *Nature physics* **2016**, *12* (12), 1124-1129.

(194) Hu, B.; Zhang, Z.; Zhang, H.; Zheng, L.; Xiong, W.; Yue, Z.; Wang, X.; Xu, J.; Cheng, Y.; Liu, X. Non-Hermitian topological whispering gallery. *Nature* **2021**, *597* (7878), 655-659.

(195) Yang, Y.; Yamagami, Y.; Yu, X.; Pitchappa, P.; Webber, J.; Zhang, B.; Fujita, M.; Nagatsuma, T.; Singh, R. Terahertz topological photonics for on-chip communication. *Nature Photonics* **2020**, *14* (7), 446-451.

(196) Zeng, Y.; Chattopadhyay, U.; Zhu, B.; Qiang, B.; Li, J.; Jin, Y.; Li, L.; Davies, A. G.; Linfield, E. H.; Zhang, B. Electrically pumped topological laser with valley edge modes. *Nature* **2020**, *578* (7794), 246-250.

(197) Zhang, X.; Wang, H.-X.; Lin, Z.-K.; Tian, Y.; Xie, B.; Lu, M.-H.; Chen, Y.-F.; Jiang, J.-H. Second-order topology and multidimensional topological transitions in sonic crystals. *Nature Physics* **2019**, *15* (6), 582-588.

(198) Cha, J.; Kim, K. W.; Daraio, C. Experimental realization of on-chip topological nanoelectromechanical metamaterials. *Nature* **2018**, *564* (7735), 229-233.

- (199) Souslov, A.; Van Zuiden, B. C.; Bartolo, D.; Vitelli, V. Topological sound in active-liquid metamaterials. *Nature Physics* **2017**, *13* (11), 1091-1094.
- (200) Nayak, A. K.; Steinbok, A.; Roet, Y.; Koo, J.; Margalit, G.; Feldman, I.; Almoalem, A.; Kanigel, A.; Fiete, G. A.; Yan, B. Evidence of topological boundary modes with topological nodal-point superconductivity. *Nature physics* **2021**, *17* (12), 1413-1419.
- (201) Hamill, A.; Heischmidt, B.; Sohn, E.; Shaffer, D.; Tsai, K.-T.; Zhang, X.; Xi, X.; Suslov, A.; Berger, H.; Forró, L. Two-fold symmetric superconductivity in few-layer NbSe₂. *Nature Physics* **2021**, *17* (8), 949-954.
- (202) Zhang, F.; MacDonald, A. H.; Mele, E. J. Valley Chern numbers and boundary modes in gapped bilayer graphene. *Proceedings of the National Academy of Sciences* **2013**, *110* (26), 10546-10551.

Biography

Shuaiguo Zhao earned his bachelor's degree in the department of Materials Science and Engineering in 2013 from Zhengzhou University, Henan, China. In 2016, he obtained his master's degree in the department of Materials Science and Engineering from Zhengzhou University, Henan, China. In 2016, he joined the Acoustofluidic lab at Duke in Thomas Lord Department of Mechanical Engineering and Materials Science.